DISSERTATION

Simulations of Soft Matter Systems

Ausgeführt zum Zwecke der Erlangung des akademischen Grades eines Doktors der Naturwissenschaften unter der Leitung von

Ao. Univ. Prof. Dr. Gerhard Kahl
Institut für Theoretische Physik (E136)
Technische Universität Wien

und

Univ. Prof. Dr. Primož Ziherl
Faculty of Mathematics and Physics
University of Ljubljana & Jožef Stefan Institute

Ljubljana, Slovenia

eingereicht an der Technischen Universität Wien
Fakultät für Physik

von

Ioannis Georgiou, M.Sc.
Matrikelnummer 1028698

Wien, im März 2014 _____

(Ioannis Georgiou)

Kurzfassung

Dendrimere, verformbare Einheiten, die über weiche, effektive Potentiale wechselwirken, gehören zu jenen Kolloidteilchen, die sich selbst zu supramolekularen Strukturen organisieren. Sie sind über eine baumartige innere Struktur aus Monomereinheiten aufgebaut und für ihre Fähigkeit bekannt, in einer Vielzahl von kristallinen, quasikristallinen und flüssigkristallinen Phasen zu kondensieren. Dieses reichhaltige Phasenverhalten kann auf die stark verzweigte, räumliche Struktur der Dendrimere zurückgeführt werden, die es ihnen ermöglicht, sich wie weiche Teilchen zu verformen und sich relativ zueinander in charakteristischen Orientierungen anzuordnen. Ausgehend von einer monomerischen Beschreibung der Dendrimere kann man effektive Wechselwirkungen zwischen diesen Makromolekülen berechnen, die für die Entstehung der verschiedenen Phasen verantwortlich sind. In dieser Arbeit betrachten wir in einem ersten Schritt isolierte, amphiphile Dendrimere (mit einem solvophoben Kern und einer solvophilen Schale) und untersuchen mithilfe von Monte Carlo Simulationen ihre geometrische Form. Dabei werden unterschiedliche Dendrimergrößen sowie verschiedene Wechselwirkungsparameter zwischen den Monomeren betrachtet. In einem weiteren Schritt werden zwei wechselwirkende Dendrimere im Grenzwert kleiner Dichten betrachtet und ihre gegenseitige Deformation und ihre relative Orientierung untersucht. Die dabei berechnete effektive Wechselwirkung wird dann mit den Wechselwirkungseigenschaften auf monomerischer Ebene in Verbindung gebracht. Schließlich wird die geometrische Form und die räumliche Orientierung der Dendrimere bei endlicher Dichte untersucht. Unsere Ergebnisse liefern eindeutige Hinweise, dass sich die nächsten Nachbarn eines Teilchen in speziellen wechselseitigen Orientierungen anordnen, die eher auf eine antinematische (als auf eine nematische) Ordnung hindeuten. Es ist möglich, dass diese antinematische Struktur bei höheren Dichten zu offenen kristallinen Strukturen, wie etwa die A15 Struktur führt.

Abstract

Among the various systems which self-organize into supramolecular structures, dendrimers – seen as deformable units interacting via ultra soft potentials – have long been recognized for their ability to condense into a wide range of crystalline, quasi-crystalline, and liquid-crystalline phases, some of which are not commonly observed for non-deformable particles. Such a rich phase behavior may be related to the highly branched, tree-like structure of dendrimers, which not only allows them to deform like soft-spheres but also to assume specific reciprocal orientation like rod-like particles. The internal structure at the monomeric level and the effective interactions between the dendrimers determine the emergence of the various bulk phases.

   In this thesis we first consider isolated amphiphilic dendrimers and investigate the dependence of their shape on the interaction parameters between their monomeric units and on their internal structure by means of monomer-resolved Monte Carlo simulations. We then study a pair of dendrimers in the zero-density limit focusing on their mutual deformation and their relative orientation; in parallel we proceed to a coarse-grained description by eliminating the internal degrees of freedom in order to obtain the dendrimer-dendrimer interaction. We then associate this so-called effective interaction to the specific features of the monomer-resolved picture. Finally, we investigate the characteristic features of the shape of our model dendrimers as well as the spatial and orientational structure of a dense dendrimer liquid. Our results in the bulk provide unambiguous evidence that the nearest-neighbor shell of a tagged particle consists of a mixture of crossed, side-by-side, side-to-end, and end-to-end pair configurations, imposing antinematic rather than nematic order observed in rod-like particles. We expect that this antinematic arrangement may give rise to non-closed-packed crystalline structures such as the A15 crystal lattice reported in several dendrimer compounds.

Contents

Chapter 1

Introduction

The term *Soft Matter* became widely known in 1991 when Pierre-Gilles de Gennes, who is considered today one of the founding fathers of soft matter physics, was awarded with the Nobel prize in physics *"for discovering that methods developed for studying order phenomena in simple systems can be generalized to more complex forms of matter, in particular to liquid crystals and polymers"* [1]. Although many examples of soft matter systems can be found in our everyday life, e.g. protein solutions, blood, mayonnaise, foam, ink, paint and cement, a simple answer to the question "What is soft matter?" is still missing.

Richard Jones describes soft matter as *"a convenient term for materials in states of matter that are neither simple liquids nor crystalline solids of the type studied in other branches of solid state physics"* [2]. It may seem that this sentence defines what soft matter is not, but nonetheless it gives rise to two important questions:

(i) How can one distinguish between soft and hard materials?

(ii) What special features exclude this type of systems from being characterized as simple liquids or solids that form crystals which are studied in sold state physics?

In order to provide an answer to question (i) we introduce a very common quantity for characterizing the hardness of a materials, i.e. the cohesive energy density $\mathcal{E}$ given by [3]

$$\mathcal{E} \approx \frac{e}{a^3}, \tag{1.1}$$

where e is the interaction energy between two particles separated by a distance a. The interaction energy e in hard matter systems is actually the covalent bond energy between the atoms, which is typically of the order of 10^{-18} J, while the bond lengths are of the order of 0.1 nanometers, i.e. $a \sim 10^{-10}$ m. Thus, the cohesive energy density of hard matter is estimated to be of the order of 10^{12} N/m². Typical sizes of particles in soft matter systems range from nanometers to micrometers, i.e. $a = 10^{-8} - 10^{-6}$ m, while the e between such mesoscopic particles (van der Waals interaction [4], hydrogen bonds, etc.) is of the order of 10^{-20} J. The resulting cohesive energy density $\mathcal{E} = 10^{-2} - 10^4$ N/m² [2] between these colloidal particles is comparable to the thermal energy $k_\mathrm{B}T$ at room temperature, meaning that even thermal fluctuations or weak mechanical disturbances [5] can be responsible for enormous structural changes in soft matter systems.

The answer to question (ii) is that soft matter systems are not simple but *complex* fluids [6]. On one hand, the term *complex* describes the inner complexity of the mesoscopic

particles that are usually composed of a large number of smaller atoms or molecules. On the other hand, the term *fluids* does not necessarily imply that these materials are in a fluid phase but it points out one key feature: *flexibility*. In his Nobel prize lecture [6], de Gennes explained this flexibility by showing how a material made of a set of independent polymer chains, such as latex, turns into a network structure (known today as rubber) when exposed to air. In this case, the mild chemical reaction of latex with the air molecules is enough to change the mechanical properties of the material enormously.

In this work we focus our interest on dendrimers, i.e. highly-branched synthetic molecules with a tree-like structure which can be synthesized by a stepwise repetitive reaction procedure. Dendrimer chemistry began in 1978 introduced by Vögtle et al. who were the first to synthesize molecules with large internal cavities [7]. Inspired by this pioneering work, Tomalia et al. [8] in the late 1980s synthesized the first dendrimers and indicated a large number of possible applications, such as synthetic membranes, encapsulating devices and many others [9]. Over the last three decades dendrimers have been studied very thoroughly using experiments, computer simulations and theory. From the experimental side the internal structure of dendrimers can be investigated by means of small-angle X-ray scattering (SAXS) [10] and small-angle neutron scattering (SANS) [11]. The most commonly studied dendrimers are the polyamidoamine (PAMAM) dendrimers because of their biocompatibility, which makes them good candidates for application in nanotechnology [12, 13] and in drug development [14] as carriers for drug delivery [15], but also for the ease and low cost of synthesis [16]. Many numerical studies focused on the characterization of such molecules [17–20]. On the numerical side, the most fundamental aspects have been investigated for neutral and charged dendrimers using fine [21–23] as well as coarse-grained [24–28] approaches. A detailed review of a large number of theoretical studies has been given by Ballauf and Likos in Ref. [29].

With a compact convex shape determined by their architecture, dendrimers are in many ways more similar to colloidal particles than to spread-out, random-coil linear polymers – yet they are penetrable like random coils, such that two dendrimers can overlap to a high degree. Much like colloidal particles, dendrimers readily crystallize, but many lattices observed (e.g. A15 and σ phases [30, 31]) are untypical for classical colloids. Some aspects of this unique behavior may be related to the dendrimer shape: The early-generation dendrimers found to have the shape of compact ellipsoids-spheroids with a considerable amount of back-folding, whereas higher generations ($G9$–$G11$) become more spherical in shape [17].

It is thus natural to expect that the optimal packing mode of dendrimers will depend on their shape and deformability. Indeed, atomistic simulations revealed that at large densities considerable interpenetration does take place [32] leading to the A15 cubic lattice as seen experimentally [31]. Complementary to this prediction are theoretical studies of penetrable ellipsoids. If forced into alignment, they form elongated lattices (obtained, e.g., by stretching the body-centered cubic crystal along [001], [110], or [111] direction) rather than cubic lattices [33, 34].

In this work we focus on the characterization of the positional and orientational order of dendrimers. We develop a coarse-grained description of dendrimers where they are regarded as soft anisotropic particles. For this, we use a model based on the amphiphilic model [see Fig. 1.1] which was the subject of research by Mladek et al. [24, 25, 35, 36] where the amphiphilicity is induced by introducing different interaction parameters between the
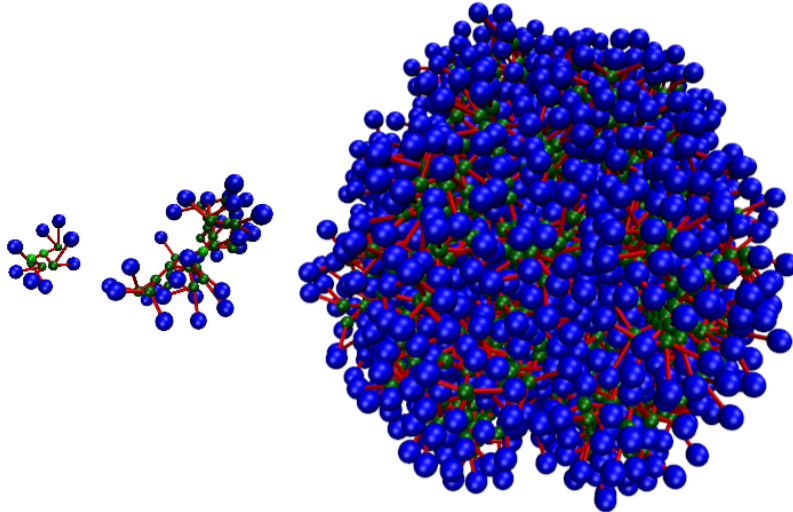
Figure 1.1: Simulation snapshots of the amphiphilic dendrimer model used in this work and for generation two ($G2$), four ($G4$) and ten ($G10$). The inner generation (core) monomers are drawn in green whereas the outer generation (shell) monomers in blue. Monomer diameters and dendrimer sizes are drawn to scale.

inner and the outer monomers. This model is known to exhibit a rich phase behavior where interpenetration (clustering) of dendrimers occurs both in the dense liquid phase as well as in the ordered solid phases [24, 35, 36]. Furthermore, low generation amphiphilic dendrimers have a more open structure and show stronger segregation between inner and outer monomers [24, 37]. Hence, using this model we can on one hand have a core-shell structure similar to the model in the work of Li et al. [32] but on the other hand we can study and tune the shape deformations in terms of potential interaction parameters.

We use monomer-resolved Monte Carlo simulations and we provide a full shape and orientational analysis of amphiphilic dendrimers based on the elements–eigenvalues and eigenvectors– of the radius of gyration tensor [38]. First, we describe the shape of a single dendrimer in terms of asphericity b and acylindricity c and for generation number $G = 2$ to 10. Our most important finding in this case is that the shape of the low generation ($G = 2$–4) dendrimers are not spherical but elongated. Afterwards, we use different coarse-grained approaches for the calculation of the effective potential and we study the effect of the dendrimers' shape and relative orientation to the form of the potential and vice versa. Afterwards, we focus on the fourth generation dendrimers and we simulate a pair of dendrimers in the zero-density limit with aim of quantifying their mutual influence on the shape and their relative orientation. Finally, we focus on the short-range-order of dendrimers in the liquid phase where we study the many-body-effects on the dendrimers' shape and relative orientation. The perpendicular relative orientations of dendrimers in the bulk system provide confirmatory evidence for the existence of an antinematic [39] rather than a nematic [40] liquid phase. We show preliminary evidence that this antinematic pattern exhibits many features of the A15 packing pattern already observed for dendritic polymers in the work of Zeng et al. [31].

The thesis is organized as follows:

- Chapter 2 gives first a brief overview of the key ideas of statistical mechanics (cf. Sec. 2.1) as well as of the Monte Carlo simulation technique. We discuss

some the useful optimization tricks that reduce significantly the computational time (cf. Sec. 2.2). Then we present different approaches for calculating the effective interactions, which takes us from a monomer-resolved to a coarse-grained description of a macromolecular system.

- Chapter 3 presents an overview of the historical key work in dendrimers and as well as of the different models used in the literature for simulating these macromolecules. Then we focus on the amphiphilic simulation model used throughout this work in terms of interaction potentials.

- Chapter 4 provides a review on the basic theories in liquid crystals as a theoretical framework for the description of the orientational order in dendrimer systems. After describing the different possible liquid crystal phases, we focus on the Onsager theory for the nematic-isotropic transition of hard rods. We quantify the orientation of molecules using the nematic order parameter by diagonalizing the nematic tensor. We use the nematic order parameter as a measure for the orientation of our model dendrimers.

- Chapter 5 summarizes the quantities that we used to analyze our simulation data with respect to shape, size and relative orientation of dendrimers. We also discuss the trustworthiness of our sampling technique.

- Chapter 6 is the bulk of this thesis as it contains the results concerning the shape and orientational properties of amphiphilic dendrimers. We present the dependence of the shape and size of isolated dendrimers on their internal structure. Then we proceed to a coarse-grained description of the interdendrimer interaction and combine it with a monomer-resolved picture of the dendrimers' deformation. We also test different approaches for quantifying the relative orientation of dendrimers on the pair level at zero density as well as in a bulk liquid.

- Chapter 7 summarizes our findings and gives an outlook on future work.

Chapter 2

Methods

In this chapter we give a brief overview of the key ideas of **statistical mechanics** and we describe the **Monte Carlo** simulation methods.

2.1 Statistical Mechanics

2.1.1 Concept of statistical mechanics

Statistical mechanics is the branch of physics that deals with the study of equilibrium and non-equilibrium properties of matter systems based on the concepts of probability theory. The difficulty associated with these systems is that they are composed of a very large number N of small microscopic parts (typically atoms or molecules), which is usually of the order of 10^{23}. While these parts obey simple equations of motion, which can be straightforwardly expressed mathematically, the large number of degrees of freedom makes it impossible to solve the mathematics exactly. The role of statistical mechanics is not to solve these equations, but rather to provide a conceptual understanding of the macroscopic variables of the system (e.g. temperature, volume, pressure, internal energy etc.) in terms of the variables that are relevant for the description of motion of the constituents of matter.

2.1.2 Phase space

In classical statistical mechanics we can fully describe a N-particle system[1] by the sets of positions and the momenta vectors $\left(\mathbf{r}^N, \mathbf{p}^N\right)$ of the particles, i.e.:

$$\mathbf{r}^N = \{\mathbf{r}_1, \mathbf{r}_2, \ldots, \mathbf{r}_N\},$$
$$\mathbf{p}^N = \{\mathbf{p}_1, \mathbf{p}_2, \ldots, \mathbf{p}_N\}. \tag{2.1}$$

Each possible configuration of the system is called a *microstate*. For a system with d physical dimensions, one microstate is characterized by a set of dN position and dN momentum vectors and can be represented as a point in the $2dN$-dimensional space, called the *phase space*. We denote as $\left(\mathbf{r}_\tau^N, \mathbf{p}_\tau^N\right)$ the set of position and momentum vectors

---

[1]System (σύστημα) comes from the greek verb συνίστημι which means to set together, combine, band together.

of a system in a specific microstate τ. In contrast, a macrostate of a system can be described by one of the systems macroscopic variables, i.e. temperature, volume, internal energy etc. Thus a microstate is one of the different arrangements that molecules can have in a particular macrostate.

The Hamiltonian $\mathcal{H}$ of the system is defined as:

$$\mathcal{H}\left(\mathbf{r}^N, \mathbf{p}^N\right) = K\left(\mathbf{p}^N\right) + \mathcal{V}\left(\mathbf{r}^N\right) + \mathcal{V}^{\mathrm{ext}}\left(\mathbf{r}^N\right), \tag{2.2}$$

where

$$K = \sum_{i=1}^{N} \frac{|\mathbf{p}_i|^2}{2m} \tag{2.3}$$

is the kinetic energy, $\mathcal{V}$ is the interatomic potential energy and $\mathcal{V}^{\mathrm{ext}}$ is the potential energy due to the interaction of particles with an external field. If all interactions are pairwise additive and radially symmetric, then the total potential energy is given by a sum of pair terms, i.e.:

$$\mathcal{V}\left(\mathbf{r}^N\right) = \sum_{i=1}^{N} \sum_{j>i}^{N} v(r_{ij}) \tag{2.4}$$

with $v(r_{ij})$ being the interatomic potential energy between particles i and j that depends only on the inter-particle separation r_{ij}.

Given an initial state, the time evolution of the system can be obtained by solving the canonical Hamilton equations of motion [41] given by:

$$\dot{\mathbf{r}}_i = \frac{\partial \mathcal{H}\left(\mathbf{r}^N, \mathbf{p}^N\right)}{\partial \mathbf{p}_i},$$

$$\dot{\mathbf{p}}_i = -\frac{\partial \mathcal{H}\left(\mathbf{r}^N, \mathbf{p}^N\right)}{\partial \mathbf{r}_i}. \tag{2.5}$$

2.1.3   Gibbsian ensemble

In order to describe a system we assume that its macroscopic physical quantities are long time averages of the corresponding instantaneous quantities. Fot the purpose of obtaining the time evolution of a microscopic state, the solution of the Hamiltonian equations of motion [see Eq. (2.5)] is required. Due to the very large number of particles on the system, namely $\sim 10^{23}$, this is not possible in practice. Thus, instead of calculating these macroscopic quantities from first principles we can use a statistical approach. For each system there is a huge number of microscopic states corresponding to the same macroscopic state. A *Gibbsian ensemble* is a collection of systems in *microstates* that correspond to the same *macrostate*, which are called macroscopically identical systems. Thus, instead of calculating time averages we can determine the macroscopical properties of the system by performing *ensemble averages*, i.e. averages of any physical quantity over an ensemble of systems.

The distribution of the phase space points of an ensemble is described by a *microstate probability distribution function* $\mathcal{P}\left(\mathbf{r}^N, \mathbf{p}^N; t\right)$ which describes the probability of finding the system in a microstate τ and at a time t. In particular, the quantity:

$$\mathcal{P}\left(\mathbf{r}_\tau^N, \mathbf{p}_\tau^N; t\right) \mathrm{d}\mathbf{r}^N \mathrm{d}\mathbf{p}^N$$

gives the probability of microstate τ, i.e. $\mathcal{P}\left(\mathbf{r}_\tau^N, \mathbf{p}_\tau^N; t\right) d\mathbf{r}_1 \ldots d\mathbf{r}_N d\mathbf{p}_1 \ldots d\mathbf{p}_N$ is proportional to the probability of finding the system at a time t in the volume element $d\mathbf{r}_1 \ldots d\mathbf{r}_N d\mathbf{p}_1 \ldots d\mathbf{p}_N$ [42]. From this definition it follows that

$$\int \int d\mathbf{r}^N d\mathbf{p}^N \mathcal{P}\left(\mathbf{r}_\tau^N, \mathbf{p}_\tau^N; t\right) = 1 \tag{2.6}$$

for all t.

The system is said to be in *statistical equilibrium* [43, 44] when

$$\frac{\partial \mathcal{P}\left(\mathbf{r}_\tau^N, \mathbf{p}_\tau^N; t\right)}{\partial t} = 0, \tag{2.7}$$

where $\int \int \ldots d\mathbf{r}^N d\mathbf{p}^N$ implies that the integral is over the whole phase space. From now on, we will use the notation $\mathcal{P}\left(\mathbf{r}^N, \mathbf{p}^N\right)$ for the microscopical statistical distribution function of a system in equilibrium. By imposing different macroscopic constraints in order to control the system under study, we get a different statistical ensemble and thus a different form for the distribution function $\mathcal{P}\left(\mathbf{r}^N, \mathbf{p}^N\right)$. The most common statistical ensembles are:

- The microcanonical (or NVE) ensemble which is used to describe isolated systems where a fixed number of particles N is confined in an also fixed volume V and where the energy E is constant.

- The canonical (or NVT) ensemble where N and V are fixed and the system is in equilibrium with a heat bath so that its temperature T remains also fixed.

- The grand canonical (or μVT) ensemble which is used to study open systems. In this case T and V are fixed but the system may exchange particles with a particle reservoir.

Let us now consider the so-called *ergodic hypothesis*. During an experiment, the observed value of the quantity A can be considered as the average of several sample values over a long period of time T. This can be expressed mathematically by

$$\langle A \rangle_{\text{time}} = \lim_{T \to \infty} \frac{1}{T} \int_0^T dt\, A(t). \tag{2.8}$$

The ergodic hypothesis assumes that the same observed values can be obtained as an ensemble average over all the allowed phase space points $\left(\mathbf{r}^N, \mathbf{p}^N\right)$. Thus,

$$\langle A \rangle_{\text{ens}} = \int \int d\mathbf{r}^N d\mathbf{p}^N A\left(\mathbf{r}^N, \mathbf{p}^N\right) \mathcal{P}\left(\mathbf{r}^N, \mathbf{p}^N\right). \tag{2.9}$$

Hence, a system is ergodic if and only if

$$\langle A \rangle_{\text{ens}} = \langle A \rangle_{\text{time}}. \tag{2.10}$$

The ergodic hypothesis is implicitly used as a justification for substituting time averages by averages over the statistical ensemble. Although this hypothesis was originally introduced

by Boltzmann in 1871 [45], there are still many on going discussion about its validity. The reason is that the ergodic hypothesis can be only verified for some very simple cases such as the classical one-dimensional harmonic oscillator. There exist some other weak forms of ergodic systems where the hypothesis is valid for almost all phase space points and which are discussed in Ref. [46].

2.1.4   Canonical ensemble

The parameters that characterize a system $\mathcal{S}$ in the canonical ensemble are: its number of particles N, its volume V and its temperature T. The system $\mathcal{S}$ is considered to interact with an infinitely large system $\mathcal{S}'$ which is called *heat reservoir* and which ensures that our system's temperature T remains constant. This way the energy of the system $\mathcal{S}$ is no longer constant like in an isolated system, but it fluctuates around a mean value.

In 1902, Gibbs showed that the microscopical distribution function of a system in thermal equilibrium with a heat reservoir is proportional to the *Boltzmann factor* [47]

$$\mathcal{P}\left(\mathbf{r}^N, \mathbf{p}^N\right) \propto \exp\left(-\beta \mathcal{H}\left(\mathbf{r}^N, \mathbf{p}^N\right)\right) \tag{2.11}$$

where $\mathcal{H}\left(\mathbf{r}^N, \mathbf{p}^N\right)$ is the Hamiltonian of the system while $\beta = 1/k_{\mathrm{B}}T$ with k_{B} being the Boltzmann constant. The normalizing factor for the probabilities [see Eq. (2.6)] in this case is called the *canonical partition function* $\mathcal{Z}\left(N, V, T\right)$ and is defined by the formula

$$\mathcal{Z}\left(N, V, T\right) = \frac{h^{-3N}}{N!} \int \int d\mathbf{r}^N d\mathbf{p}^N \exp\left(-\beta \mathcal{H}\left(\mathbf{r}^N, \mathbf{p}^N\right)\right) \tag{2.12}$$

where h is the Planck constant and $N!$ is needed to properly normalize the phase integral of indistinguishable particles.

Using Eq. (2.2) and by setting the external field to zero we can rewrite Eq. (2.12) as:

$$\mathcal{Z}\left(N, V, T\right) = \frac{h^{-3N}}{N!} \int \int d\mathbf{r}^N d\mathbf{p}^N \exp\left(-\beta \left(\sum_{i=1}^{N} \frac{|\mathbf{p}_i|^2}{2m}\right)\right) \exp\left(-\beta \mathcal{V}\left(\mathbf{r}^N\right)\right). \tag{2.13}$$

This way, we can perform the integration over the momenta and over the position vectors separately. The integration over each component of the momenta in Eq. (2.13) can be done using the known integral of the Gaussian form[2] and yields a factor $(2\pi m/\beta)^{1/2}$. Thus, the partition function reads now as

$$\mathcal{Z}\left(N, V, T\right) \equiv \frac{z_N}{\Lambda^{3N} N!} \tag{2.14}$$

where

$$\Lambda \equiv \sqrt{\frac{\beta h^2}{2\pi m}} \tag{2.15}$$

is the thermal de Broglie wavelength and

$$z_N = \int d\mathbf{r}^N \exp\left(-\beta \mathcal{V}\left(\mathbf{r}^N\right)\right) \tag{2.16}$$

---

[2] Gaussian integral: $\int_{-\infty}^{\infty} \exp\left(-ax^2\right) \mathrm{d}x = (\pi/a)^{1/2}$.

is the configuration integral.

The importance of the partition function stems from the fact that it links statistical mechanics with thermodynamics. In particular, the Helmholtz free energy $\mathcal{F}$, the thermodynamic potential which measures the portion of energy that is available to perform thermodynamic work of a system under constant volume and temperature, is connected to the partition function through the relation:

$$\mathcal{F}(N, V, T) = -k_\mathrm{B} T \log \mathcal{Z}(N, V, T).$$
(2.17)

Physical quantities can be expressed as first- or second-order derivatives of the Helmholtz free energy $\mathcal{F}$ [48–50]. Thus, the knowledge of how $\mathcal{F}$ (or equivalently $\mathcal{Z}$) varies with the temperature, or any other constraint that affects the system under study, can give us all of the information that we need to know about the macroscopic behavior of the system [49]. For example, the internal energy U, i.e. the expectation value of the Hamiltonian $\langle \mathcal{H} \rangle$, can be expressed in terms of the first derivative of the free energy in respect to the volume V and the number of particles N

$$U = \left(\frac{\partial \beta \mathcal{F}}{\partial \beta} \right)_{V,N} = -\frac{1}{\mathcal{Z}} \left(\frac{\partial \mathcal{Z}}{\partial \beta} \right)_{V,N}.$$
(2.18)

In a similar way we can calculate the pressure P

$$P = -\left(\frac{\partial \mathcal{F}}{\partial V} \right)_{T,N} = \frac{1}{\beta} \left(\frac{\partial \log \mathcal{Z}}{\partial V} \right)_{T,N}.$$
(2.19)

as well as the chemical potential μ, which is a measure of the change in the Helmholtz free energy upon the addition of one particle in the system,

$$\mu = \left(\frac{\partial \mathcal{F}}{\partial N} \right)_{T,V} = -\frac{1}{\beta} \left(\frac{\partial \log \mathcal{Z}}{\partial N} \right)_{T,V}.$$
(2.20)

2.2 Monte Carlo simulations

> *"Science is what we understand well enough to explain to a computer. Art is everything else we do."*
>
> Donald Knuth

This section is dedicated to the Monte Carlo (MC) method [48, 49, 51], which is a broad class of numerical methods that rely on random number generation in order to solve certain problems. This method is used to obtain numerical results for problems which cannot be solved analytically. In physics, MC methods are useful when dealing with systems of many degrees of freedom where in order to obtain properties of the system, the solution of a large number of equations [such as the Hamilton equations Eq. (2.5)] is required.

2.2.1 Purpose of Monte Carlo simulations

Once we know the microstate distribution function $\mathcal{P}\left(\mathbf{r}^N, \mathbf{p}^N\right)$ of the ensemble, the average of any physical property A can be calculated through Eq. (2.9) which for the canonical

ensemble takes the form

$$\langle A \rangle = \frac{\int \int d\mathbf{r}^N d\mathbf{p}^N A\left(\mathbf{r}^N, \mathbf{p}^N\right) \exp\left(-\beta \mathcal{H}\left(\mathbf{r}^N, \mathbf{p}^N\right)\right)}{\int \int d\mathbf{r}^N d\mathbf{p}^N \exp\left(-\beta \mathcal{H}\left(\mathbf{r}^N, \mathbf{p}^N\right)\right)}. \tag{2.21}$$

Properties that depend only on the momenta are in most of the cases easy to evaluate [52]. Thus, in a similar way to the calculation of the partition function in Sec. 2.1.4, we can also separate the exponential of Eq. (2.11) into a configurational and a kinetic part and carry out the integration over the momenta separately. Then our problem reduces:

$$\langle A \rangle = \frac{\int d\mathbf{r}^N A\left(\mathbf{r}^N\right) \exp\left(-\beta \mathcal{V}\left(\mathbf{r}^N\right)\right)}{\int d\mathbf{r}^N \exp\left(-\beta \mathcal{V}\left(\mathbf{r}^N\right)\right)} \tag{2.22}$$

$$= \int d\mathbf{r}^N A\left(\mathbf{r}^N\right) \mathcal{P}\left(\mathbf{r}^N\right) \tag{2.23}$$

where

$$\mathcal{P}\left(\mathbf{r}^N\right) = \frac{\exp\left(-\beta \mathcal{V}\left(\mathbf{r}^N\right)\right)}{z_N} \tag{2.24}$$

is the probability density of finding the system in a configuration around $\mathbf{r}^N$ which is also known as the *Boltzmann distribution*. The first approach to calculate the average in Eq. (2.23) would be to evaluate the average $\langle A \rangle$ by numerical integration. The difficulty is that this would require discretizing a very large space, namely the dN-dimensional configurational space, which would result in a magnitude of computation that exceeds the limits of what can be realistically calculated with present-time computers [50].

2.2.2   Monte Carlo importance sampling

Another, more realistic, way for calculating such high dimensional integrals is by using *Monte Carlo integration*. In this case, instead of of iterating through all different configurations of the descretized configurational space (see Sec. 2.2.1), we first choose a random subset of M configurations, i.e. $\left\{\mathbf{r}_1^N, \mathbf{r}_2^N, \ldots, \mathbf{r}_M^N\right\}$ from a certain probability distribution $p\left(\mathbf{r}_i^N\right)$ and then we estimate the average value of the physical quantity in Eq. (2.23) by calculating its estimator A_M given by:

$$A_M = \frac{\sum\limits_{i=1}^{M} A\left(\mathbf{r}_i^N\right) p\left(\mathbf{r}_i^N\right)^{-1} \exp\left(-\beta \mathcal{V}\left(\mathbf{r}_i^N\right)\right)}{\sum\limits_{i=1}^{M} p\left(\mathbf{r}_i^N\right)^{-1} \exp\left(-\beta \mathcal{V}\left(\mathbf{r}_i^N\right)\right)}. \tag{2.25}$$

This quantity has the property that the larger the M the more accurate the estimation for the average $\langle A \rangle$, since:

$$\lim_{M \to \infty} A_M = \langle A \rangle. \tag{2.26}$$

A rather naive approach would be to choose these states from a uniform probability, i.e. to make all the probabilities $p\left(\mathbf{r}_i^N\right)$ equal. Thus, by substituting

$p\left(\mathbf{r}_1^N\right) = p\left(\mathbf{r}_2^N\right) = \ldots = p\left(\mathbf{r}_M^N\right)$ into Eq. (2.25), we get:

$$A_M = \frac{\sum\limits_{i=1}^{M} A\left(\mathbf{r}_i^N\right)\exp\left(-\beta\mathcal{V}\left(\mathbf{r}_i^N\right)\right)}{\sum\limits_{i=1}^{M}\exp\left(-\beta\mathcal{V}\left(\mathbf{r}_i^N\right)\right)}. \tag{2.27}$$

The problem with this choice is that we are not sampling enough the interesting configurations. The reason is that a real physical system does not sample the states uniformly but according to the microstate probability distribution function, which in the canonical ensemble is the Boltzmann distribution [see Eq. (2.24)].

Metropolis et al. [53] proposed an algorithm that samples states from a probability distribution $\mathcal{P}\left(\mathbf{r}^N\right)$. In this case the M random states are directly generated according to the Boltzmann distribution and thus, the expression for the estimator [see Eq. (2.25)] becomes a simple arithmetic average

$$A_M = \frac{1}{M}\sum_{i=1}^{M} A\left(\mathbf{r}_i^N\right), \tag{2.28}$$

where $\mathbf{r}_i^N$ is generated according to the desired distribution. This technique is known as *importance sampling* or *Metropolis MC*.

2.2.3   Markov chains

But how do we generate random states states with the correct canonical probability $\mathcal{P}\left(\mathbf{r}^N\right)$ in Eq. (2.24)?

We can achieve that by using a mathematical tool called *Markov chain* [54]. In a Markov chain, the system at each timestep can undergo a transition from one state into another. It does that randomly so that the system has no memory. This means that the next state of the system depends *only* on the current state and not on the previous states that the system has passed through.

In a MC simulation a Markov chain is created in the following way: suppose that at a timestep t the system is in a state τ. We then randomly generate a new trial state ν, i.e. a new trial configuration $\mathbf{r}^N$. A way to do this is by choosing a random particle on the system and then adding a small random displacement $\Delta\boldsymbol{\xi}_i$ to its position, i.e. perform a *single-particle displacement*. Next, we accept or reject the trial state in such a way that the configuration is generated according to $\mathcal{P}\left(\mathbf{r}^N\right)$. If the trial configuration is accepted, then at timestep $t+1$ the system is in the new state ν, otherwise it remains in the old state τ, which is now counted as the new state of the system. By repeating this procedure over and over again we will eventually generate a trajectory of states where each state appears with the correct probability. This trajectory can be then used to calculate quantity averages according to Eq. (2.28). In the following section we describe the conditions that have to be fulfilled in order for the states in the trajectory to appear with the correct probability.

2.2.4 Master equation and detailed balance

At this point we need to determine a criterion for the acceptance of states such that all the states in the long time trajectory are generated according to the canonical probabilities given by Eq. (2.24). We repeat here for convenience that:

$$\mathcal{P}\left(\mathbf{r}^N\right) = \frac{\exp\left(-\beta \mathcal{V}\left(\mathbf{r}^N\right)\right)}{z_N}. \tag{2.29}$$

For the discussion that follows, we denote by $\mathcal{P}_\tau(t)$ the probability that at timestep t the system will be in a state/configuration τ and by $R(\tau \to \nu)$ the *transition probability*, i.e. the probability that a system that is currently in a state τ will undergo a transition into a state ν at any time t. We note here that since both quantities express probabilities they should also obey the sum rule at any timestep t, i.e.:

$$\sum_\tau \mathcal{P}_\tau(t) = 1,$$

$$\sum_\nu R(\tau \to \nu) = 1.$$

The time evolution of $\mathcal{P}_\tau(t)$ is governed by the so-called **master equation** [55], which is given by the formula:

$$\frac{d\mathcal{P}_\tau(t)}{dt} = \sum_\nu \left[\mathcal{P}_\nu(t) R(\nu \to \tau) - \mathcal{P}_\tau(t) R(\tau \to \nu)\right]. \tag{2.30}$$

The first term inside the sum of the right-hand side of this equation represents the rate of transitions into a state τ whereas the second one the rate at which the system undergoes transitions out of τ into other states. In order to better explain the meaning of the equation above, we consider just one timestep forward on our Markov chain. For this case Eq. (2.30) reads as

$$\mathcal{P}_\tau(t+1) = \mathcal{P}_\tau(t) + \sum_\nu \mathcal{P}_\nu(t) R(\nu \to \tau) - \sum_\nu \mathcal{P}_\tau(t) R(\tau \to \nu). \tag{2.31}$$

This means that for a given state τ the master equation takes into account:

  (i) the increase in the probability associated with undergoing a transition from other states ν into τ and

  (ii) the decrease in the probability due to transition going from τ into other states ν.

What we want to achieve is for those probabilities to converge to a *stationary*, independent of time, *distribution* that is equal to the canonical microstate probability distribution function. In other words, we want:

$$\lim_{t \to \infty} \mathcal{P}_\tau(t) = \frac{\exp\left(-\beta \mathcal{V}\left(\mathbf{r}_\tau^N\right)\right)}{z_N}. \tag{2.32}$$

In order for this to be possible, the Markov transitions have to fulfill two important

conditions:

(i) the condition of *ergodicity* and

(ii) the condition of *detailed balance.*

The first condition –ergodicity– says there there should exist *at least* one path of non-zero transition probabilities between any two states ν and τ on our Markov chain. This is necessary since we want the states in our chain to appear with the correct Boltzmann probability. More specific, suppose that we have a state ν, which is inaccessible from another state τ although it appears with some non-zero probability $\mathcal{P}\left(\mathbf{r}_\tau^N\right)$ in the Boltzmann distribution. Then, the probability of finding state ν in our chain will be zero and not $\mathcal{P}\left(\mathbf{r}_\tau^N\right)$ as it is required to be.

On the other hand, the condition of detailed balance is the one that ensures that in equilibrium all states in the chain appear with the correct Boltzmann distribution. We say that the system has reached an *equilibrium* state when the two terms in the sum of the right-hand side of the master equation (Eq. (2.30)) cancel each other and thus $d\mathcal{P}_\tau\left(t\right)/dt = 0$. This can be expressed mathematically by

$$\sum_\nu \mathcal{P}_\tau R\left(\tau \to \nu\right) = \sum_\nu \mathcal{P}_\nu R\left(\nu \to \tau\right) \tag{2.33}$$

This so-called *balance equation* indicates that at equilibrium, the probabilities should not change, i.e. the rate at which the system undergo a transition from a state τ has to be equal to the number of transitions into that state. We denote with the symbol $\mathcal{P}_\tau$ the probabilities $\mathcal{P}_\tau(t)$ at equilibrium.

If the transition probabilities satisfy Eq. (2.33) then, the Markov chain has reached an equilibrium probability $\mathcal{P}_\tau$. This, however, does not guarantee that the states generated will have the desired probability distribution since there is the possibility that the system has reached a *dynamic equilibrium* (see [49]). To overcome this we impose an even stronger condition called the *detailed balance*:

$$\mathcal{P}_\tau R\left(\tau \to \nu\right) = \mathcal{P}_\nu R\left(\nu \to \tau\right), \quad \text{for each } \tau \text{ and } \nu. \tag{2.34}$$

By summing both sides over ν, we see that this choice also satisfies Eq. (2.33)[3].

Further, the transition probabilities are split into two factors [49, 50]:

$$R\left(\tau \to \nu\right) = g\left(\tau \to \nu\right) A\left(\tau \to \nu\right) \tag{2.35}$$

where

- $g\left(\tau \to \nu\right)$ is the selection probability, which expresses the probability that the algorithm will generate from an initial state τ a new state ν and

- $A\left(\tau \to \nu\right)$ is the acceptance ratio, which is the probability to accept the newly generated state ν.

---

[3]If the detailed balance condition is obeyed then the general balance condition is also obeyed. The opposite is not true.

From Eq. (2.35) we can calculate the ratio of the transition rates as:

$$\frac{R\left(\tau \to \nu\right)}{R\left(\nu \to \tau\right)} = \frac{g\left(\tau \to \nu\right) A\left(\tau \to \nu\right)}{g\left(\nu \to \tau\right) A\left(\nu \to \tau\right)}. \tag{2.36}$$

By imposing also the detailed balance condition [Eq. (2.34)] we get for the acceptance ratios:

$$\frac{A\left(\tau \to \nu\right)}{A\left(\nu \to \tau\right)} = \frac{g\left(\nu \to \tau\right) \mathcal{P}_\nu}{g\left(\tau \to \nu\right) \mathcal{P}_\tau}. \tag{2.37}$$

This equation is the one we need to create our MC simulation. By imposing it at any timestep in our Markov chain we guarantee that:

(i) the detailed balance [Eq. (2.34)] is satisfied

(ii) we converge in an equilibrium probability distribution $\mathcal{P}_\tau$.

2.2.5 Metropolis Monte Carlo

"The spirit of this method was consistent with Stan's interest in random processes from the simple to the sublime. He relaxed playing solitaire; he was stimulated by playing poker; he would cite the times he drove into a filled parking lot at the same moment someone was accommodatingly leaving. "

N. Metropolis [56]

The first importance sampling MC method algorithm was proposed in 1953 by Metropolis et al. [53]. Prior to the Metropolis algorithm, the usual method for studying systems that follow the Boltzmann distribution was to create a huge number of random configurations, calculate then the properties of interest and then produce their average by weighting each one of them with the relevant Boltzmann factor. The *Los Alamos* team proposed *"a modified Monte Carlo scheme where, instead of choosing configurations randomly, then weighting them with* $\exp\left[-\beta\mathcal{V}\left(\mathbf{r}^N\right)\right]$*, they choose configurations with a probability* $\exp\left[-\beta\mathcal{V}\left(\mathbf{r}^N\right)\right]$ *and weight them evenly "* [56]. The configuration of the algorithm is based on the principles mentioned in Sec. 2.2.4 and is described below.

Let as assume that we have a system of N particles confined in a volume V. Suppose that the system is initially in a state $\tau = 1$ and that we want to accept or reject a trial state $\nu = 2$. These states, 1 and 2, correspond to some particle configurations $\mathbf{r}_1^N$ and $\mathbf{r}_2^N$ respectively. Then, according to Eq. (2.36), we have

$$\frac{A\left(1 \to 2\right)}{A\left(2 \to 1\right)} = \frac{g\left(2 \to 1\right) \mathcal{P}_2}{g\left(1 \to 2\right) \mathcal{P}_1}. \tag{2.38}$$

The fact that Eq. (2.38) fixes only the ratio $A\left(1 \to 2\right)/A\left(2 \to 1\right)$ of the acceptance probabilities, gives us the freedom about on how we choose the selection probabilities $g\left(1 \to 2\right)$ and $g\left(2 \to 1\right)$. In the original Metropolis scheme the MC moves are symmetric, which means that the selection probabilities are equal for the forward and the reverse transition [53], i.e.:

$$g(1 \to 2) = g(2 \to 1). \tag{2.39}$$

In this case, from Eq. (2.38) follows that:

$$\frac{A(1 \to 2)}{A(2 \to 1)} = \frac{\mathcal{P}_2}{\mathcal{P}_1}. \tag{2.40}$$

An example of symmetric moves is a single-particle displacement, where the trial configuration is created from the old one by moving a single random particle positioned at $\mathbf{r}_i$ following the prescription:

$$\mathbf{r}_i \to \mathbf{r}_i + \Delta\boldsymbol{\xi}_i. \tag{2.41}$$

Here, we denote by Δ denotes the maximum displacement[4] and by $\boldsymbol{\xi}_i$ a random unitary vector[5]. The particle can be then located anywhere within a cube centered at $\mathbf{r}_i$ and of side length 2Δ.

Within the canonical ensemble we wish the equilibrium distribution is the canonical distribution [see Eq. (2.29)]. Therefore Eq. (2.38) takes the form:

$$
\begin{aligned}
\frac{A(1 \to 2)}{A(2 \to 1)} = \frac{\mathcal{P}_2}{\mathcal{P}_1} &= \frac{\exp\left(-\beta\mathcal{V}\left(\mathbf{r}_2^N\right)\right)}{\exp\left(-\beta\mathcal{V}\left(\mathbf{r}_1^N\right)\right)} \\
&= \exp\left(-\beta\left[\mathcal{V}\left(\mathbf{r}_2^N\right) - \mathcal{V}\left(\mathbf{r}_1^N\right)\right]\right) \\
&\equiv \exp\left(-\beta\left(\mathcal{V}_2 - \mathcal{V}_1\right)\right).
\end{aligned}
\tag{2.42}
$$

This equation leaves us with many possible choices for the acceptance acceptance probabilities, with the constraint that $A(1 \to 2)$ cannot exceed 1. The choice of Metropolis et al., also known as the *Metropolis criterion*, is:

$$A(1 \to 2) = \min\left(1, \exp\left(-\beta\left(\mathcal{V}_2 - \mathcal{V}_1\right)\right)\right) \tag{2.43}$$

Hence, in order to choose the acceptance ratios we first need to calculate the energy cost $\Delta\mathcal{V} \equiv \mathcal{V}_2 - \mathcal{V}_1$ for changing the particle position. If a move of the particle results in a decrease in the energy, then the new configuration is always accepted. Thus, $A(1 \to 2) = 1$. Otherwise, the move is accepted with a probability $\exp\left(-\beta\left(\mathcal{V}_2 - \mathcal{V}_1\right)\right)$. To determine this probability, we play a game of chance biased by a Boltzmann factor, i.e.:

(i) we choose a random number $\hat{\xi}$ between 0 and 1

(ii) if $\hat{\xi} < \exp\left(-\beta\left(\mathcal{V}_2 - \mathcal{V}_1\right)\right)$ then the new configuration is accepted

(iii) if $\hat{\xi} > \exp\left(-\beta\left(\mathcal{V}_2 - \mathcal{V}_1\right)\right)$ then the move is rejected and the system remains in the old configuration.

We should note here that for the purpose of taking averages according to Eq. (2.27), we consider that we are always in a new configuration whether a move is accepted or not.

---

[4]The factor Δ can be automatically tuned by the update algorithm such that the ratio of accepted configurations is 30 – 60% (for example) of the trial configurations. This tuning should not be done during measurements, or else detailed balance *might* be ruined.

[5]Randomly orientated vectors can be calculated using Marsaglia's algorithm [57].

We can verify that the Metropolis criterion satisfies the detailed balance by calculating the ratio $A(1 \to 2)/A(2 \to 1)$ using Eq. (2.43):

$$
\begin{aligned}
\frac{A(1 \to 2)}{A(2 \to 1)} &= \frac{\min\left(1, \exp\left(-\beta\left(\mathcal{V}_2 - \mathcal{V}_1\right)\right)\right)}{\min\left(1, \exp\left(-\beta\left(\mathcal{V}_1 - \mathcal{V}_2\right)\right)\right)} \\
&= \begin{cases} \frac{\exp\left(-\beta(\mathcal{V}_2 - \mathcal{V}_1)\right)}{1} & \text{if } \mathcal{V}_2 > \mathcal{V}_1 \\ \frac{1}{\exp[-\beta(\mathcal{V}_1 - \mathcal{V}_2)]} & \text{if } \mathcal{V}_1 > \mathcal{V}_2 \end{cases} \\
&= \exp\left(-\beta\left(\mathcal{V}_2 - \mathcal{V}_1\right)\right)
\end{aligned}
\tag{2.44}
$$

which agrees with Eq. (2.43).

The acceptance ratios for the Metropolis MC can be summarized in the following formula:

$$
A(\tau \to \nu) = \begin{cases} \exp\left(-\beta\left(\mathcal{V}_\nu - \mathcal{V}_\tau\right)\right) & \text{if } \mathcal{V}_\nu > \mathcal{V}_\tau \\ 1 & \text{otherwise} \end{cases}
\tag{2.45}
$$

or in a more compact form:

$$
A(\tau \to \nu) = \min\left(1, \exp\left(-\beta\left(\mathcal{V}_\nu - \mathcal{V}_\tau\right)\right)\right).
\tag{2.46}
$$

2.3   Finite size systems and optimization

2.3.1   Periodic boundary conditions and minimum image convention

MC simulations of systems serves the purpose of providing information about the properties of a macroscopic sample. In reality, only a small number of particles can be handled within a simulation using present-day computers. Let us, for example, assume a system of N particles confined in a cubic box of constant side L (in units of particle diameters). If we divide the box into $n \times n \times n$ smaller cubes of side length equal to one particle diameter, we can then see that we have a number of $(n-2)^3$ cubes that are *not* located on the surface of the box. Thus, on the surface we have

$$
N_{sur} = n^3 - (n-2)^3
\tag{2.47}
$$

such cubes. Suppose we have 1000 particles arranged in a $10 \times 10 \times 10$ cubic box. Then according to Eq. (2.47) 488 particles will be located on the box's surface. Thus there is a fraction of $\sim 50\%$ of the molecules that appear on the surface of the box.

Periodic boundary conditions (PBC) [58] are useful when simulating a finite system as a part of a large infinite system where no surface is present. By PBC, we mean that our model system is placed in a *central cell* and it is replicated throughout the space to form an infinite system (see Fig. 2.1). That is, if the position vectors of the particles in the central cubic cell are $\mathbf{r}_i$ then the PBC create *periodic* images of particles at positions

$$
\mathbf{r}'_i = \mathbf{r}_i + L\left(l\hat{\mathbf{x}} + m\hat{\mathbf{y}} + n\hat{\mathbf{z}}\right),
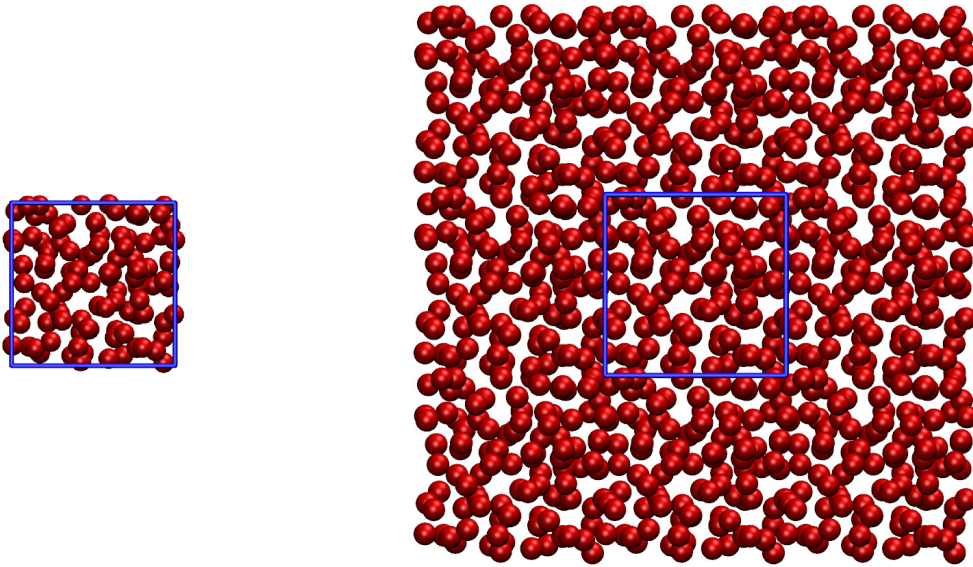\tag{2.48}
$$

Figure 2.1: Schematic representation of periodic boundary conditions. Left: Central unit cell. Right: The central unit is replicated an infinite amount of times. The position of the particles in the periodic images are given by Eq. (2.48). The blue square marks the central unit cell.

where $\hat{\mathbf{x}}, \hat{\mathbf{y}}$ and $\hat{\mathbf{z}}$ are the unit vectors of the cubic box edges and l, m, n are integers that range from $-\infty$ to ∞. Therefore there are no walls at the boundaries of the central cell and thus no surface particles. As a particle moves within the original (central) cell, also all of its periodic images in the repeated cells move exactly the same way. However, when a particle crosses the boundary of the cell, one of its images will enter at the opposite side of the central cell. Consequently, due to the surrounding cells, a particle in the central cell not only interacts with the particles within the same cell, but also with their periodic images (including its own periodic image) belonging to all other cells.
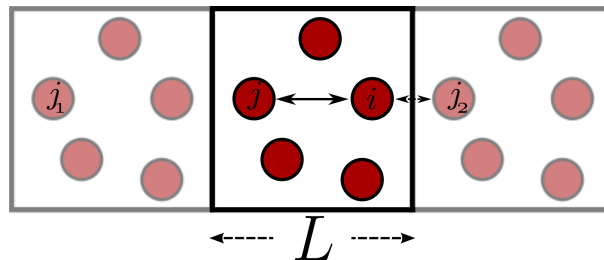

Figure 2.2: Schematic representation of the minimum image convention. The central square represents the central unit cell while the lower opacity ones the neighboring images in one direction. The minimum image convention states that a particle i can interact only with the closest image of any other particle j which may or may not lie on the same cell. Here we consider the interaction between particles i and j. We denote with j_1 and j_2 the two images of particle j in the neighboring images. In this case the closest image is j_2.

Applying PBC on a system does not imply that the effect of the small number of particles automatically vanishes. There are certain limitations induced by the use of PBC. Firstly, the characteristic size of any structural property of the system should be smaller than the size of the central cell. Secondly, the size of the central cell should be larger than $2r_c$, with r_c being the cutoff radius of the interatomic potential energy $\mathcal{V}(\mathbf{r}_N)$[6]. This way we ensure that none of the particles interacts with itself and also that any atom i interacts with only one periodic image of any other particle j. The latter is called *the minimum image convention* and is schematically represented in Fig. 2.2.
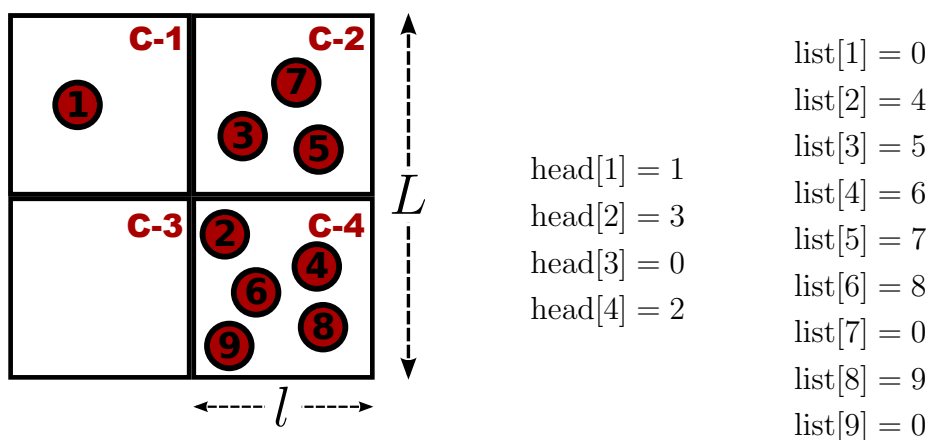
2.3.2   Cell lists

Figure 2.3: Left: A schematic representation of the cell list method. The simulation box of side L, which contains nine particles in total, is divided to four cells of side length l each and denoted as C-1, C-2, C-3 and C-4. Right: The particle index of the first element in each sub-cell is stored in the head-of-chain (head) array while the particle indexes the follow on the list are stored in the linked-list (list) array. For simplicity, we consider that the first element of each cell is the particle with the lower index.

Typically, most of the computational time during a MC simulation is consumed in calculating a double loop over all particle pairs, which is required for the evaluation of the interatomic potential energy $\mathcal{V}(\mathbf{r}^N)$. For pairwise-additive interactions [see Eq. (2.4)] this calculation is of the order of $N(N-1)/2$. Although there exist several techniques that can be used to reduce this dependence to $O(N)$ (for larger systems) still most of the simulation time will be taken by this loop [61, 62]. As explained before, for short-range interactions we typically use a cut-off radius, beyond which particle interactions are considered to be 0. In this case and for simulations involving a large number of particles ($N \geq 1000$) only pairs within this cut-off distance have to be considered. Therefore, we can decrease the simulation time significantly by keeping a list of neighbors that are located a distance smaller than r_c. Such a *cell list* was proposed by Quentrec and Brot [63] and is described in the following. Let us assume that we are performing simulations in a three-dimensional

---

[6]Short-range potential and treated differently than long-range potentials and are discussed in Refs. [59–62].
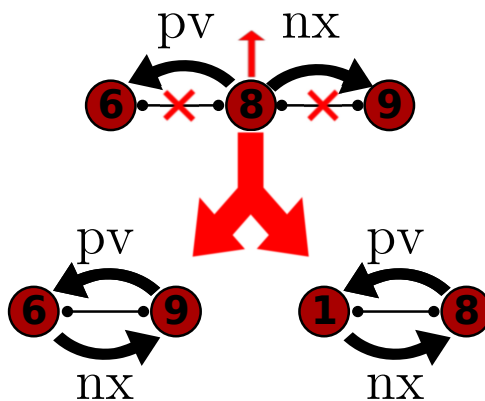
Figure 2.4: Update cell list after a single particle has left the cell. Suppose that particle 8 has been moved from its original cell C-4 into cell C-1. Initially, the *previous* index of particle 8 holds particle 6 while the *next* index holds particle 9. So, pv[8] = 6 and nx[8] = 9. After 8 has left C-4 we have to update the pv and nx for the remaining particles. This way, pv[9] = 6 and nx[6] = 9. After particles 8 has joined C-1 we have: nx[1] = 8, pv[8] = 1, nx[8] = 0.

simulation box of side length L. We divide the box into $M \times M \times M$ smaller boxes, called sub-cells, of equal side length $l = L/r_c$. Each of the sub-cells then contains on average $N_c = N/M^3$ particles. We also assume that each particle in a sub-cell interacts only with the particles in the same sub-cell and with the particles in the *first-neighboring* sub-cells. By applying this, we have to go through $3^3 N_c N$ instead of $N(N-1)/2$ pairs of particles for the calculation of the interatomic potential in Eq. (2.4).

The method can be implemented using the singly- or doubly-linked lists [64, 65]. We first describe the simple case of creating a cell list using singly-linked list with the help the example system of nine particles shown in Fig. 2.3. At the beginning of the simulation we assign to each cell the corresponding particles according to each particle's position. The particles are stored in cell with the use of two arrays. One array, called *head-of-chain*, stores the address of the first particle of each cell. In other words, in the element head [n] of the head-of-chain array we store the index of the first particle found inside the nth cell. This particle is then used as the *list*'s index to locate the next particle using the *linked-list* array (list) which contains the next element of the cell, i.e. the element list [i] holds the particle index that follows particle i on the list. This procedure is repeated until the 0th element is found on the list; this element signals the end of the list. An example of how cell lists are populated is shown in Fig. 2.3.

The disadvantage of this method is that whenever a particle moves to a neighboring cell, the whole list has to be updated. To avoid the construction of a new list each time a particle has left its original cell, we can just update the existing list at the cost of some extra book-keeping. This can be done by additionally introducing to each particle two more indices. Namely, we keep track of the *next* and *previous* indices of particles connected with a particle i. The elements nx[i] and pv[i] hold the indices of the next and the previous particles of particle i, respectively. Now, each time that a particle moves to a neighboring cell only these two indices need to be updated. This method decreases significantly the execution time of a MC simulation program, especially in the case where single monomer moves are considered. Figure 2.4 illustrates how the update is done for

the system shown in Fig. 2.3.

2.4   Special aspects of Monte Carlo simulations

2.4.1   Widom insertion method

The Widom or particle insertion method [66] is a technique that can be used to sample the chemical potential within a MC simulation. In the canonical ensemble, the chemical potential is defined as the change in the Helmholtz free energy upon the addition of one particle [cf. Eq. (2.20)]:

$$\mu = \left(\frac{\partial \mathcal{F}}{\partial N} \right)_{T,V}. \tag{2.49}$$

Starting from the configuration integral of Eq. (2.16), if $\mathcal{V}_N = 0$:

$$z_N = \int \int \cdots \mathrm{d}\mathbf{r}^N = V^N. \tag{2.50}$$

Thus the partition function [see Eq. (2.14)] of a uniform and ideal gas takes the form

$$\mathcal{Z}^{\mathrm{id}} = \frac{V^N}{\Lambda^{3N} N!}. \tag{2.51}$$

The corresponding ideal Helmholtz free energy is

$$\mathcal{F}^{\mathrm{id}} = -N k_{\mathrm{B}} T \ln \left(\frac{V^N}{\Lambda^{3N} N!} \right) \tag{2.52}$$

$$= -N k_{\mathrm{B}} T \left[\ln \left(\frac{\Lambda^3 N}{V} \right) - 1 \right] \tag{2.53}$$

where for the latter equation we use Stirling's approximation for $\ln N!$.

With the help of equation Eq. (2.20) the ideal chemical potential reads

$$\mu^{\mathrm{id}} = -k_{\mathrm{B}} T \ln \left(\frac{\Lambda^3 N}{V} \right). \tag{2.54}$$

The partition function of a system N interacting particles can now be written as

$$\mathcal{Z}_N = \mathcal{Z}_N^{\mathrm{id}} \frac{z_N}{V^N}. \tag{2.55}$$

By taking the logarithm on both sides we can naturally separate the Helmholtz free energy into an ideal and an excess part:

$$\mathcal{F} = \mathcal{F}^{\mathrm{id}} + \mathcal{F}^{\mathrm{ex}} \tag{2.56}$$

where the excess part is

$$\mathcal{F}^{\mathrm{ex}} = -k_{\mathrm{B}} T \ln \frac{z_N}{V^N} \tag{2.57}$$

For $N \gg 1$, Eq. (2.49) for the case of the excess chemical potential takes the form

$$\mu^{\mathrm{ex}} = \mathcal{F}^{\mathrm{ex}}\left(N+1, V, T\right) - \mathcal{F}^{\mathrm{ex}}\left(N, V, T\right)$$
$$= -k_{\mathrm{B}}T \ln\left(\frac{1}{V}\frac{z_{N+1}}{z_N}\right). \tag{2.58}$$

By substituting Eq. (2.14) to Eq. (2.58) we get:

$$\mu^{\mathrm{ex}} = -k_{\mathrm{B}}T \ln\left(\frac{\int \mathrm{d}\mathbf{r}^{N+1} \exp\left[-\beta\mathcal{V}\left(\mathbf{r}^{N+1}\right)\right]}{V \int \mathrm{d}\mathbf{r}^{N} \exp\left[-\beta\mathcal{V}\left(\mathbf{r}^{N}\right)\right]}\right). \tag{2.59}$$

The interatomic potential energy $\mathcal{V}\left(\mathbf{r}^{N+1}\right)$ of the $(N+1)$-particle system is the sum of the energy of the N-particle system and the interaction energy $\Delta\mathcal{V}$ of the extra, $(N+1)^{\mathrm{th}}$ particle with the rest of the system, i.e.:

$$\mathcal{V}\left(\mathbf{r}^{N+1}\right) = \mathcal{V}\left(\mathbf{r}^{N}\right) + \Delta\mathcal{V}. \tag{2.60}$$

Then μ_{ex} can be rewritten as:

$$\begin{aligned}
\mu_{\mathrm{ex}} &= -k_{\mathrm{B}}T\frac{\int \mathrm{d}\mathbf{r}^{N+1} \exp\left(-\beta\Delta\mathcal{V}\right)\exp\left(\mathcal{V}\left(\mathbf{r}^{N}\right)\right)}{V \int \mathrm{d}\mathbf{r}^{N} \exp\left(\mathcal{V}\left(\mathbf{r}^{N}\right)\right)}\\
&= -k_{\mathrm{B}}T\frac{V \int \mathrm{d}\mathbf{r}^{N} \exp\left(-\beta\Delta\mathcal{V}\right)\exp\left(\mathcal{V}\left(\mathbf{r}^{N}\right)\right)}{V \int \mathrm{d}\mathbf{r}^{N} \exp\left(\mathcal{V}\left(\mathbf{r}^{N}\right)\right)}\\
&= -k_{\mathrm{B}}T \ln\left\langle\exp\left(-\beta\Delta\mathcal{V}\right)\right\rangle_N
\end{aligned} \tag{2.61}$$

where $\left\langle\ldots\right\rangle_N$ denotes a canonical ensemble average over the configuration space of the N-particle system.

Therefore, we can compute the chemical potential within a standard MC simulation of the N-particle system the following way: while the simulation is running, we randomly generate coordinates for the $(N+1)^{\mathrm{th}}$ particle uniformly distributed inside the three dimensional simulation box. Using this random value for $\mathbf{r}_{N+1}$ we first compute $\Delta\mathcal{V}$ and then we sample $\exp\left(-\beta\Delta\mathcal{V}\right)$. We should note here that the random particle is never inserted in the N-particle system. This is why it is also referred to as the *ghost particle*.

As an example, we calculate the chemical potential of a hard sphere (HS) fluid [67, 68]. In this case, the interaction potential between the particles is given by:

$$\mathcal{V}\left(r\right) = \begin{cases} \infty & \text{if } r < \sigma \\ 0 & \text{if } r \geq \sigma \end{cases} \tag{2.62}$$

where σ is the diameter of the hard sphere. In Fig. 2.5 we compare the simulations results for μ_{ex} as a function of the numbered density ρ with the theoretical prediction for the μ_{ex} calculated according to the Carnahan and Starling equation of state [67], i.e.

$$\beta\mu_{\mathrm{ex}} = \frac{3\eta^3 - 9\eta^2 + 8\eta}{\left(1-\eta\right)^3} \tag{2.63}$$
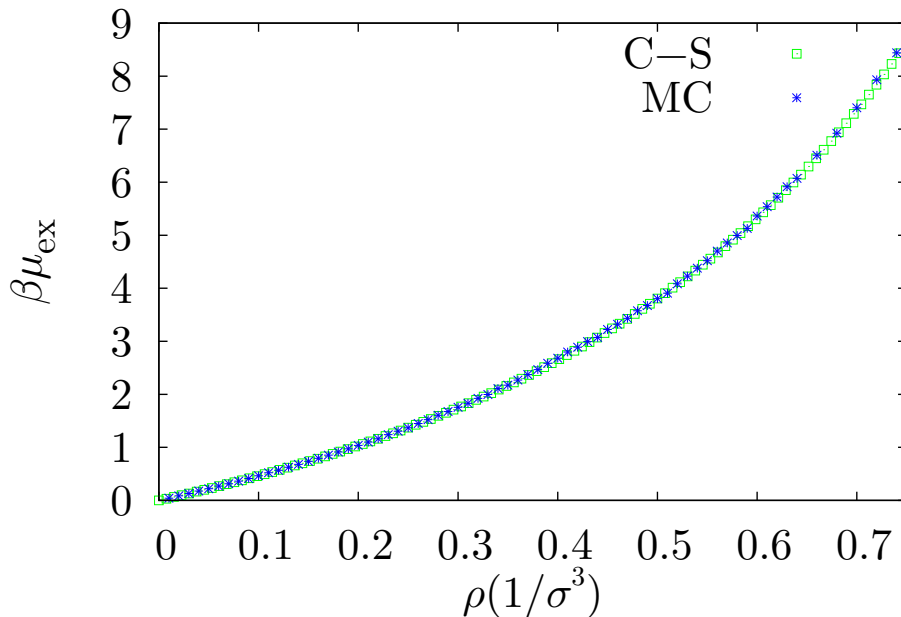
where $\eta = \pi\rho/6$.

Figure 2.5: Comparison of the μ_{ex} calculated from MC simulations using the Widom method, with the values derived from the Carnahan-Starling equation of states and for various density values ρ. Errors are within symbol size.

2.4.2   Non-Boltzmann sampling

As we have already explained (see Sec. 2.2.2), using the importance sampling method, we are able to sample through a sequence of trial configurations where each one is accepted or rejected according to the Boltzmann distribution. The macroscopic quantities are then calculated by a simple arithmetic average [cf. Eq. (2.28)]. Using this method, we only sample the important regions of the phase space, while regions where probability is negligible are rarely or never sampled. There are cases, though, where the important regions of the phase space are separated by high free-energy barriers to areas of non-negligible probabilities. Thus, the use of the simple Metropolis method would lead to biased results since the system would not be able to cross these barriers.

A method to overcome this broken ergodicity is the *umbrella sampling* and was proposed by Torrie and Valleau [69] and it is actually a variation of a more general scheme referred to today as *non-Boltzmann sampling* [70, 71]. In this method the phase space is sampled within a *biased ensemble*. By *biased* we mean that the probability distribution that we use is not related to a standard statistical ensemble (NVT, NPT, μVT, etc.). Yet, any results obtained in the biased ensemble have to somehow be related back to the results for the same system in one of the usual ensembles. The idea is as follows: for the probability distribution of our system within the canonical ensemble we have [cf. Eq. (2.24)]:

$$\mathcal{P}_\tau \propto \exp\left(-\beta \mathcal{V}_\tau\right)^{7}. \tag{2.64}$$

---

[7]Remark: for convenience we have dropped the $\mathbf{r^N}$ dependence from the symbols $\mathcal{P}_\tau$, $\mathcal{V}_\tau$.

In order to perform a *biased* simulation we introduce an additional factor to the exponent of the above equation, i.e.:

$$\mathcal{P}_{\tau}^{(b)} \propto \exp\left(-\beta\mathcal{V}_{\tau} + W_{\tau}\right). \tag{2.65}$$

We denote with $\mathcal{P}_{\tau}^{(b)}$ the probability distribution in the biased ensemble and $W_{\tau} \equiv W\left(\mathbf{r}_{\tau}^{N}\right)$ the so-called umbrella potential. The value of umbrella potential is such that some the states will appear with higher or lower probability than expected. In the biased ensemble Eq. (2.42) takes the form:

$$\frac{A\left(\tau \to \nu\right)}{A\left(\nu \to \tau\right)} = \frac{\mathcal{P}_{\tau}^{(b)}}{\mathcal{P}_{\nu}^{(b)}} = \exp\left(-\beta\left(\mathcal{V}_{\nu} - \mathcal{V}_{\tau}\right) + \left(W_{\nu} - W_{\tau}\right)\right)$$

$$= \exp\left(-\beta\Delta\mathcal{V} + \Delta W\right) \tag{2.66}$$

and thus the Metropolis criterion in Eq. (2.42) becomes:

$$A\left(\tau \to \nu\right) = \min\left(1, \exp\left(-\beta\Delta\mathcal{V} + \Delta W\right)\right). \tag{2.67}$$

In the biased ensemble, the average of a macroscopic variable A according to Eq. (2.28) is

$$\langle A \rangle^{(b)} = \frac{1}{M}\sum_{i=1}^{M} A_i \tag{2.68}$$

where i is the index over the M different configurations in the biased ensemble. If we now want to compute the above average in the *unbiased* (here canonical) ensemble, i.e. $\langle A \rangle^{(u)}$, we can still performed simulations in the biased ensemble and then weight accordingly by taking into account the differences between the two weighting factors, Eqs. (2.64) and (2.65). Namely, from Eq. (2.23) we get:

$$\langle A \rangle^{(u)} = \frac{\int \mathrm{d}\mathbf{r}^N A\left(\mathbf{r}^N\right)\exp\left(-\beta\mathcal{V}\left(\mathbf{r}^N\right)\right)}{\int \mathrm{d}\mathbf{r}^N \exp\left(-\beta\mathcal{V}\left(\mathbf{r}^N\right)\right)}$$

$$= \frac{\int \mathrm{d}\mathbf{r}^N A\left(\mathbf{r}^N\right)\exp\left(-W\left(\mathbf{r}^N\right)\right)\exp\left(-\beta\mathcal{V}\left(\mathbf{r}^N\right) + W\left(\mathbf{r}^N\right)\right)}{\int \mathrm{d}\mathbf{r}^N \exp\left(-W\left(\mathbf{r}^N\right)\right)\exp\left(-\beta\mathcal{V}\left(\mathbf{r}^N\right) + W\left(\mathbf{r}^N\right)\right)}$$

$$= \frac{\langle A\exp\left(-W\right)\rangle^{(b)}}{\langle \exp\left(-W\right)\rangle^{(b)}} \tag{2.69}$$

where we denote with $\langle \ldots \rangle^{(b)}$ an average in the biased ensemble. Thus the canonical ensemble average of the physical quantity A can be calculated as:

$$\langle A \rangle^{(u)} = \frac{\sum_{i=1}^{M} A_i\,\exp\left(-\beta W_i\right)}{\sum_{i=1}^{M}\exp\left(-\beta W_i\right)} \tag{2.70}$$

where each A_i is now the value of A in a microstate i in the biased ensemble.

2.4.3   Coarse-graining and effective interactions

Macromolecules (e.g. dendrimers and star polymers) are built from a large number of monomers. In polymer science we are mostly interested in the investigation of the properties of polymer solutions, i.e. a mixture of macromolecules and a large number of smaller particles, known as the *solvent*. Studying these already highly complex entities in a solution increases significantly the number of degrees of freedom significantly. In order to reduce this complexity and get an insight in the properties of such systems we need to map the *fine-grained* monomeric system to an equivalent *coarse-grained* system which consists of fewer but larger subcomponents; the procedure that one follows in order to do that is called *coarse-graining* [26, 27, 72, 73] and is presented in the following.

Within simulations, we are able on a first level to reduce the degrees of freedom by treating the solvent as a continuous medium and expressing the effect of the solvent through the potential used for the monomer-monomer interactions [74]. However, even after most of the microscopic details of the solvent have been removed we are still left with the large number of microscopic degrees of freedom of the macromolecules. Here is the point were the "effective" description of the macromolecules becomes important: instead of treating the full system we can treat all macromolecules as point particles which interact with each other by means of an effective interaction. This effective interaction has to be constructed in such a way that the effect of all the monomers is included and that the thermodynamics of the system is preserved.

Suppose that we have two macromolecules labeled by $\alpha = 1$ and 2 enclosed in a macroscopic volume V and each one consisting of N monomers. We denote with $\mathbf{r}_\alpha^N$ and $\mathbf{p}_\alpha^N$ the sets of position and momenta of macromolecule α, respectively, i.e.:

$$\mathbf{r}_\alpha^N = \{\mathbf{r}_{1\alpha}, \mathbf{r}_{2\alpha}, \ldots, \mathbf{r}_{N\alpha}\},$$
$$\mathbf{p}_\alpha^N = \{\mathbf{p}_{1\alpha}, \mathbf{p}_{2\alpha}, \ldots, \mathbf{p}_{N\alpha}\}. \tag{2.71}$$

The Hamiltonian $\mathcal{H}\left(\mathbf{r}_1^N, \mathbf{r}_2^N, \mathbf{p}_1^N, \mathbf{p}_2^N\right)$ of the system of the two macromolecules can be split in terms of $\mathcal{H}_{kl}$ that contain the interactions between macromolecules k and l **only**, i.e.:

$$\mathcal{H}\left(\mathbf{r}_1^N, \mathbf{r}_2^N, \mathbf{p}_1^N, \mathbf{p}_2^N\right) = \mathcal{H}_{11}\left(\mathbf{r}_1^N, \mathbf{p}_1^N\right) + \mathcal{H}_{12}\left(\mathbf{r}_1^N, \mathbf{p}_1^N, \mathbf{r}_2^N, \mathbf{p}_2^N\right) + \mathcal{H}_{22}\left(\mathbf{r}_2^N, \mathbf{p}_2^N\right) \tag{2.72}$$

The canonical partition function of the system is[8]:

$$\mathcal{Q} = \frac{1}{h^{6N}} \int \int \mathrm{d}\mathbf{r}_1^N \mathrm{d}\mathbf{p}_1^N \mathrm{d}\mathbf{r}_2^N \mathrm{d}\mathbf{p}_2^N \ \exp\left(-\beta\mathcal{H}\left(\mathbf{r}_1^N, \mathbf{r}_2^N, \mathbf{p}_1^N, \mathbf{p}_2^N\right)\right). \tag{2.73}$$

At this point it is helpful to introduce the center-of-mass density operators:

$$\hat{\rho}_{\mathrm{cm}}^{(\alpha)}\left(\mathbf{R}_\alpha\right) = \delta\left(\mathbf{R}_\alpha - \frac{1}{N}\sum_{i=1}^{N}\mathbf{r}_{i\alpha}\right), \ \ \alpha = 1, 2 \tag{2.74}$$

where $\mathbf{R}_\alpha$ is the position vector of the center-of-mass of macromolecule α and $\delta\left(\cdot\right)$ is the Dirac delta function. Then, according to Refs. [26, 27], by keeping the macromolecules'

---

[8]We have dropped the combinatorial factors $N!$ [cf. Eq. (2.12)] in the definition of the partition function since the monomers in this case are distinguishable due to their connectivity.

center-of-masses fixed at $\mathbf{R}_1$ and $\mathbf{R}_2$ the effective interaction $\Phi_{\text{eff}}(\mathbf{R}_1, \mathbf{R}_2)$ between the two identical macromolecules is defined as:

$$
\begin{aligned}
\beta \Phi_{\text{eff}}(\mathbf{R}_1, \mathbf{R}_2) = -\ln \Bigg(& \frac{V^2}{\mathcal{Q}_1^2} h^{-6N} \int \int d\mathbf{r}_1^N d\mathbf{p}_1^N d\mathbf{r}_2^N d\mathbf{p}_2^N \\
& \times \hat{\rho}_{\text{cm}}^{(1)}(\mathbf{R}_1) \hat{\rho}_{\text{cm}}^{(2)}(\mathbf{R}_2) \exp\left(-\beta \left(\mathcal{H}_{11} + \mathcal{H}_{12} + \mathcal{H}_{22}\right)\right) \Bigg)
\end{aligned}
\tag{2.75}
$$

where V is the volume of the system and $\mathcal{Q}_1$ is the partition function of the single macromolecule defined as:

$$
\mathcal{Q}_1 = \frac{1}{h^{3N}} \int \int \mathrm{d}\mathbf{r}_1^N \mathrm{d}\mathbf{p}_1^N \exp\left(-\beta \mathcal{H}_{11}\right). \tag{2.76}
$$

By combining Eqs. (2.73) and (2.75) and integrating over $\mathbf{R}_1$ and $\mathbf{R}_2$ we get for the partition function $\mathcal{Q}$ of the system:

$$
\mathcal{Q} = \frac{\mathcal{Q}_1^2}{V^2} \int \int \mathrm{d}\mathbf{R}_1 \mathrm{d}\mathbf{R}_2 \exp\left(-\beta \Phi_{\text{eff}}(\mathbf{R}_1, \mathbf{R}_2)\right). \tag{2.77}
$$

The effective interaction depends only on the intermacromolecule separation $R = |\mathbf{R}_1 - \mathbf{R}_2|$. Thus, we can write

$$
\Phi_{\text{eff}}(\mathbf{R}_1, \mathbf{R}_2) = \Phi_{\text{eff}}(R). \tag{2.78}
$$

The direct computation of $\Phi_{\text{eff}}(R)$ through Eq. (2.75) cannot be achieved using standard simulation techniques since the effective potential [Eq. (2.75)] has the form of a restricted partition function. However, from Eq. (2.75), it can be shown [26, 27] that the effective interaction can be related to the correlation function $g(R)$ between the positions of the centers-of-mass through the equation:

$$
g(R) \equiv \left\langle \hat{\rho}_{\text{cm}}^{(1)}(\mathbf{R}_1) \hat{\rho}_{\text{cm}}^{(2)}(\mathbf{R}_2) \right\rangle \propto \exp\left(-\beta \Phi_{\text{eff}}(R)\right) \tag{2.79}
$$

where $\langle x \rangle_R$ denotes an ensemble average over quantity x of a system of two particle which are separated by a distance R. Therefore, the problem of computing the effective interaction reduces to evaluating the expectation value in Eq. (2.79) which can be done using standard simulation techniques. In what follows we describe three different simulation techniques for calculating the effective interactions of macromolecules.

2.4.3.1   Umbrella sampling method

A common approach to compute the effective pair-interaction between two macromolecules is by using its relation with the radial distribution function $g(R)$ [RDF, cf. Sec. 5.1 and Eq. (2.79)]:

$$
\beta \Phi_{\text{eff}}(R) = -\ln\left(g(R)\right). \tag{2.80}
$$

However, the repulsion between macromolecules increases as they get closer to each other. Hence, while measuring the radial distribution function for two particles, the system would spend most of the time in configurations with either large particle separations or in ranges with overall attractive interactions. In order to obtain the effective interaction for the whole range of separations one can employ the technique of umbrella-sampling [24, 50] (cf. Sec. 2.4.2).

This method relies on introducing an additional term to the interactions of our model, a so-called biasing potential. The simplest choice is to take a series of windows of biasing potentials $W^i(R)$ on the centers-of-mass of the dendrimers that have the form

$$W^i(R) = \begin{cases} 0, & R^i_{\min} < R < R^i_{\max} \\ \infty, & \text{otherwise} \end{cases} \tag{2.81}$$

which limits the centers-of-mass distance to be within the range $[R^i_{\min}, R^i_{\max}]$. For each window i we obtain the effective interaction using the formula

$$\beta\Phi^i_{\text{eff}}(R) = -\ln\left(g^i(R)\right) + c_i \tag{2.82}$$

with $g^i(R)$ being the RDF measured in this particular range and c_i being an unknown constant.

By dividing the full interaction range into a number of overlapping windows, the complete RDF and hence the effective pair-interaction can be reconstructed. This is realized by matching the partial $\Phi^i_{\text{eff}}(R)$ with choosing appropriate constants c_i and imposing $\beta\Phi_{\text{eff}}(R_{\max}) = 0$.

2.4.3.2   Widom particle insertion method

This method for determining the effective interaction between two mesoscopic particles is based on Widom particle insertion method and was developed by Mladek and Frenkel [25]. It relies on simulating two isolated dendrimers, which are equilibrated independently using standard MC simulations. Thereafter, the dendrimers are placed on a centers-of-mass distance R generated uniformly in the interval $R \in [0, R_{\max}]$. If for each distance the intermolecular potential energy $\Delta U(R)$ is evaluated, the effective interaction $\Phi_{\text{eff}}(R)$ can be obtained from:

$$\beta\Phi_{\text{eff}}(R) = -\ln\left(\left\langle\exp\left(-\beta\Delta U(R)\right)\right\rangle_R\right) + c. \tag{2.83}$$

where $\langle a\rangle_R$ denotes a canonical ensemble over the quantity a in the system of two dendrimers at a center-of-mass distance R. Similar to the umbrella sampling method (Sec. 2.4.3.1) the parameter c is determined by requiring that the potential is 0 at $R = R_{\max}$, where the intermolecular potential energy has decayed to zero.

2.4.3.3   Force integration method

An alternative way of extract the effective interaction between two macromolecules is by calculating the force $\mathbf{F}_\alpha$ acting on the center-of-mass of each macromolecule α, due to the presence of the other macromolecule. This force is given by

$$\mathbf{F}_\alpha = -\nabla_{\mathbf{R}_\alpha}\Phi_{\text{eff}}\left(\mathbf{R}_1, \mathbf{R}_2\right). \tag{2.84}$$

It has been shown in Ref. [27] that this force can be calculated within a MC or a Molecular Dynamics simulation as the expectation value of the forces exerted on the individual

monomers of macromolecule α due to the monomers of the other macromolecule, i.e.:

$$\mathbf{F}_\alpha(R) = \left\langle \sum_{i=1}^{N} \mathbf{F}_{i\alpha} \right\rangle_R . \tag{2.85}$$

This method has been applied for in the calculation of the effective interaction between star polymers [75, 76] as well as between dendrimers [35, 36].

2.5 MC simulation of dendrimers

In order to study in detail the properties of dendrimers (cf. Sec. 3.1), we investigate our model system (cf. Sec. 3.2.3.2) at three different density regimes:

- the infinite dilution limit in which single isolated dendrimers are considered,

- the infinite dilution limit for a pair of dendrimers, and

- the bulk limit were the system is studied at finite densities.

For all theses regimes, we use a standard NVT MC simulation with the conventional Metropolis acceptance criterion. For the case of single dendrimer as well as for the bulk system we employ single translational monomer moves [see Eq. (2.41)]. For a pair of dendrimers center-of-mass moves were considered in order to keep the dendrimers at a fixed distance. One way to achieve this is to choose a random bead i and generate its new position using the rule $\mathbf{r}_i \to \mathbf{r}_i + \Delta\boldsymbol{\xi}_i$. Then, to keep the center-of-mass of the dendrimer at the same position, we move the rest of the beads $j \neq i$ according to the following formula:

$$\mathbf{r}_j \to \mathbf{r}_j - \frac{\Delta}{N_m - 1}\boldsymbol{\xi}_j \tag{2.86}$$

where N_m is the total number of monomers in the dendrimer. Initially, orientational moves [50] were also considered.

Chapter 3

Model

3.1 Polymers and dendrimers

Polymers are molecules that are synthesized through a process called **polymerization**, by which single components (*monomers*) are connected to each other through covalent bonds[1]. A widely studied example of polymers is the polypropelene $[(C_3H_6)_N]$. The subscript N denotes the number of times the monomer, here C_3H_6, is repeated; N is referred to as the *degree of polymerization* of the polymer. One of the most common methods for synthesizing polypropylene is by polymerizing propylene monomer by the Ziegler-Natta polymerization (see Fig. 3.1).
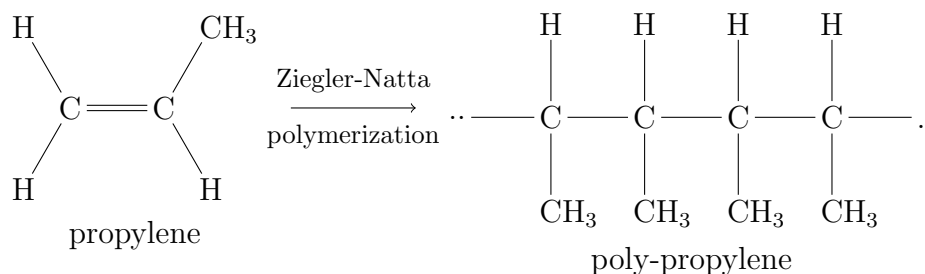
Figure 3.1: Polymerization of propylene monomers using the Ziegler-Natta polymerization method.

The properties of a polymer are determined by its degree of polymerization as well as by its architecture. Polymers consisting of only one monomer type are called *homopolymers*, whereas those consisting of several different types of monomers into a single chain are called *heteropolymers*.

Polymers can be classified according to their structure to:

- linear

- branched (or hyperbranched), and

- crosslinked.

---

[1](Poly)-(mer) means (many)-(parts) πολυ-μερές [77].

In linear polymers the monomeric units are linked together to form a linear chain of finite length. Examples are nylon, polyester or polyvinylchloride (PVC). In the case of branched polymers the monomers form long chains with side branches which can consist of different size monomers and can have various lengths. The most common branched polymers are low-density polyethylene, glycogen and starch. In crosslinked polymers different polymer chains form bridges, called crosslinks, which tie them all together. Vulcanized rubber is a widely polymer used in industry that falls into this category.

Hyperbranched polymers [78, 79] are polymers based on AB_{f-1} monomers, i.e. monomers that have a single functional group of type A and $(f - 1)$ terminal functional groups of type B, where A can only react with B. In Fig. 3.2, we show an example of an AB_2 hyperbranched polymer, i.e. $f = 3$. In this case, we can have three different types of monomers: dendritic (d), linear (l) or terminal (t) defined as monomers having 2, 1 or 0 B groups reacted. The degree of branching (DB), a quantity that measures the proportion ratio of perfectly reacted sites in a hyperbranched polymer, is defined as [80, 81]

$$DB = \frac{D + T}{D + T + L} \tag{3.1}$$

where D, L and T are the mole fractions of the dendritic, linear and terminal monomers.
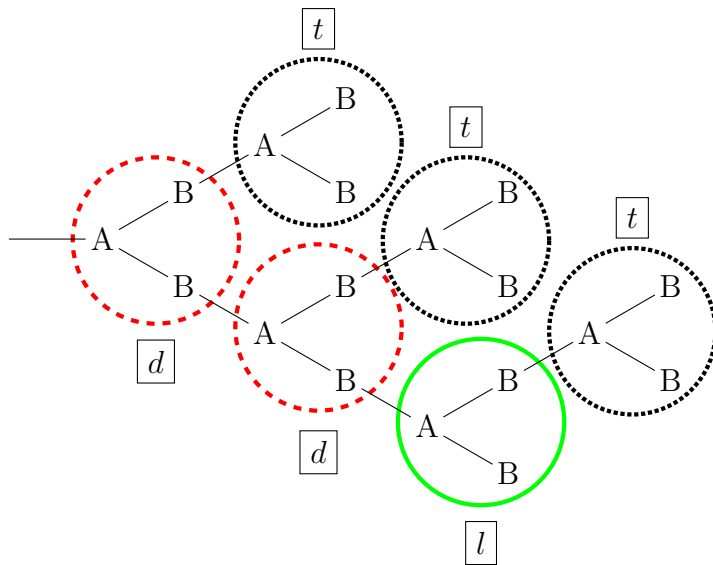
Figure 3.2: Example of a hyperbranched (AB_2) polymer. The dotted circles (black) mark the terminal (t), the dashed (red) the dendritic (d) and the continuous (green) circles the linear (l) monomers. In this case $D = 2/6$, $T = 3/6$ and $L = 1/6$ and so, according to Eq. (3.1), DB = 55/6.

3.2   Dendrimers

In this section we first describe the growth procedure of regular dendrimers, i.e. a special case of hyperbranched polymers (see Sec. 3.1), as well as some of the basic quantities that

are used for describing the shape and the microscopic structure of a dendrimer. Then we summarize the most important work done on dendrimers in the period 1978–2010 needed in order to describe the dendrimer model used throughout this thesis. Finally, we present two of the different models that are used in literature for simulating dendrimers.

3.2.1   Regular dendrimers

A very interesting and special subset of hyperbranched polymers are *dendrimers*. Their DB has the value of 1 which means that they branch at each monomeric unit and as a result they have a perfect architecture. They are typically synthesized through an iterative reactive procedure which leads to a tree-like structure. During this procedure, branched monomers are successively added in layers, starting from a monomer core with branching groups. Each layer is called a *generation*. We denoted with the letter G the total number of generations.

   We first describe the growth procedure for the simple case of a *regular dendrimer*. This procedure is similar to the one described in Sec. 3.1 for hyperbranched polymers with the difference that here the growth starts from an initial B_n core whose terminal groups can react only with n AB_{f-1} monomers. Initially, their B groups are protected from further reactions to ensure that the AB_{f-1} will only react with the initial core and not with each other. As soon as the first generation is completed the B groups are activated and the whole structure acts like a $B_{n(f-1)}$ core that can further react with $n(f-1)$ AB_{f-1} in order for the second generation to be created. This procedure can be repeated an infinite number of times, where on each step $n(f-1)^{G-1}$ monomers are added to the current structure. The special case of $f = n$ has a structure of a **Cayley tree** [77, 82] and is presented in Fig. 3.3.
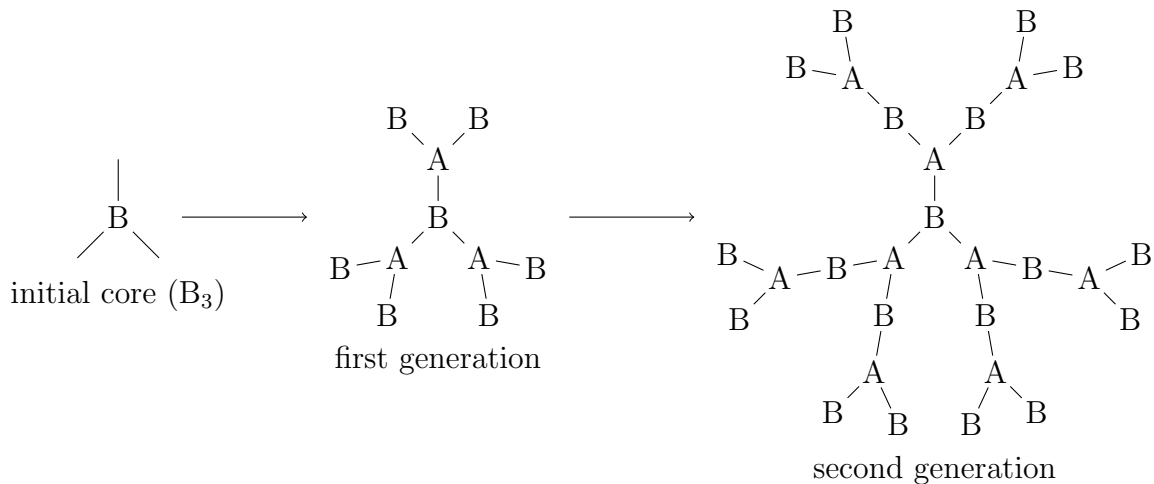

Figure 3.3: Example of a growth procedure of a regular dendrimer with $f = n = 3$ up to second generation.

   Now we define the characteristic quantities of a single dendrimer. First we consider a regular dendrimer as described in Sec. 3.2.1. The central particles constitute the zeroth generation (see Fig. 3.4a). Each monomer has functionality f (see Fig. 3.3) which means that from there, f linear chains of P bonds each can be attached. The quantity P is known

as the *spacer length* of the dendrimer. The total number of monomers of a dendrimer of generation G is given by the formula:

$$N = 1 + f \, P \frac{(f-1)^{G+1} - 1}{f-2}.$$

(3.2)

We denote a dendrimer of generation $G = m$ with the symbol Gm. The monomers of the last generation form the *shell* of the dendrimer, while the rest form the *core* of the dendrimer. The total number of monomers N_{shell} belonging to the shell is given by

$$N_{\text{shell}} = f(f-1)^{G}.$$

(3.3)

In Fig. 3.4 we present the most common case of regular dendrimers, i.e. $f = 3$ and $P = 1$.

$G0$
$N = 4$
$N_{\text{shell}} = 3$

$G1$
$N = 10$
$N_{\text{shell}} = 6$

$G2$
$N = 22$
$N_{\text{shell}} = 12$

(a)   (b)   (c)
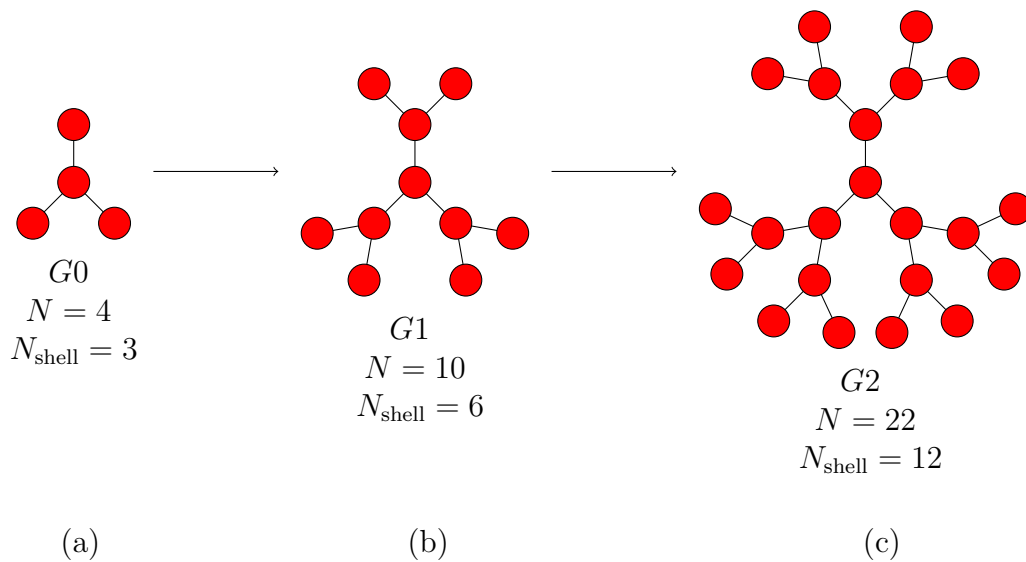
Figure 3.4: Schematic representation of regular dendrimers, with $f = 3$ and $P = 1$ for generations 0 (a), 1 (b) and 2 (c). For each case the total number of monomers as well as the number of shell monomers are displayed.

The radius of gyration R_{g}, measures the overall size of a dendrimer. Let $\mathbf{r}_i$ be the position vectors of the monomers $i = 1 \ldots N$ of a dendrimer and let $\mathbf{R}_{\text{CM}}$ be the position of the center-of-mass of the dendrimer. Then:

$$R_{\text{g}}^2 = \frac{1}{N} \left\langle \sum_{i=1}^{N} (\mathbf{r}_{\text{i}} - \mathbf{R}_{\text{CM}})^2 \right\rangle.$$

(3.4)

The radial monomer density profile $\rho(\mathbf{r})$ is a quantity that gives information on the conformation of a dendrimer and reads

$$\rho(\mathbf{r}) = \left\langle \sum_{i=1}^{N} \delta(\mathbf{r} - \mathbf{r}_{\text{i}}) \right\rangle,$$

(3.5)

where $\langle \cdots \rangle$ denotes an average over all different configurations. The quantity $\rho(\mathbf{r})$ implies that the average number of monomers lying in the range from r to $r + \mathrm{d}r$ from the center-of-mass of the dendrimer is $4\pi r^2 \rho(r)\mathrm{d}r$.

3.2.2   A brief history of dendrimers

(i) 1978: Cascade molecules

Dendrimers' chemistry was introduced in 1978 by Vögtle et al. [7] (University of Bonn, Germany) who synthesized the first dendrimers (termed *"cascade molecules"*) and described the advantages of frequent repetitions procedures in the construction of *large* molecular cavities.

(ii) 1982: Host-guest character

Maciejewski et al. discussed in Ref. [83] the concepts of synthesis of shell topo-logical compounds, which consist of guest molecules trapped by a host molecule with a spatial, egg shell like structure. This "shell-cast" characterization of dendrimers (termed as starburst molecules at that time) was based on the assumption that starburst polymers consist of a hollow-core and a dense-shell.

(iii) 1983: Starburst polymers

Tomalia presented for the first time the sequential construction of branched polymers as a novel technology in *The Winter Polymer Gordon Conference* (Santa Barbara, CA) [9].

(iv) 1984: Hollow-core, dense-shell model

Motivated by Tomalia's unpublished work, de Gennes and Hervet proposed in Ref. [84] a purely theoretical approach on the growth of starburst polymers. Using a modified version of the Edwards self-consistent field [85, 86], they predicted that the monomeric density increases from the core to the periphery up to a limiting radius R_l. Thus a limiting generation number G_l exists, above which the starburst process cannot continue. This limiting generation is given by the relation:

$$G_l = 2.88 \ln P + 4.4 \pm 0.2, \tag{3.6}$$

where P is the spacer length defined in Sec. 3.2.1. Well below this limit the polymer radius R scales with the molecular weight M as $R \sim M^{0.2}$, while above this limit compact structures are expected and thus $R \sim M^{0.33}$. This study created a theoretical background for further studies based on the hollow-core (dense-shell) assumption to come. Their result was not surprising, since the whole study was based on the assumption that each successive generation was at further radial distance from the core in such a way that the free (unreacted) groups always face outwards and thus they would always lie on the surface of the starburst polymer.

(v) 1985: The term "dendrimers" appears for the first time in the bibliography

In 1985, Tomalia et al. in the Dow Laboratories (Dow Chemical Co.) published [8] the work done during the period 1979-1985 and presented the first family of well-characterized dendrimers with a unique core-shell macromolecular architecture synthesized with the use of a divergent method developed [16, 87]. These polymers had a central hollow core and tendrils that branched outwards, one from another in a precise predictable manner. Inspired by their tree-like branching structure, Tomalia termed these macromolecules *dendrimers*, from the Greek word *dendron* for tree. Poly(amido amine) (PAMAM) dendrimers were produced in high yields and in different molecular weights. In this work the term dendrimers appeared for the first time. In Fig. 3.5, a second generation PAMAM dendrimer is presented.
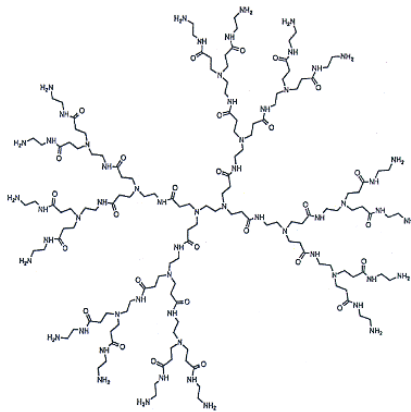
Figure 3.5: $G2$ PAMAM-dendrimer

(vi) Dense-core model

The de Gennes dense shell model (iv) was for a long time the accepted concept for the structure of dendrimers. Lescanec and Muthukumar [88] simulated the growth of starburst polymers using a self-avoiding walk algorithm [74] in three dimensions. They studied molecules with trifunctional branch points and flexible spacers P $(= 1, 3, 5, 7, 9$ and $11)$. Their results showed that the free ends do not necessarily lie on the surface of the molecule but they can fold back to the inner part. This was in contradiction with the theoretical predictions made by de Gennes given in Eq. (3.6). The physical properties studied in this work showed a strong dependence on the spacer length. In particular, the radius of gyration R_{g}, was proven to scale like

$$R_{\mathrm{g}} \sim M^{\nu} P^{q} \ \text{ with } \nu = 0.22 \text{ and } q = 0.5. \tag{3.7}$$

Although the simulation model used had by construction a non-equilibrium nature, their work gave rise to the dense-core model and was the starting point for many theoretical studies.

(vii) Dense-core vs. dense-shell model

It was the pioneering theoretical work of Boris and Rubinstein in Ref. [89] that supported the validity of the dense core model. These authors performed equilibrium self-consistent mean field (SCFM) [90] calculations and derived a simple analytical equation for the dependence of the radius of gyration upon generation. Their results showed that starburst dendrimers are characterized by a dense rather than a hollow core. The ends of the dendrimers were found to be distributed throughout the volume of the dendrimer whereas the monomeric density was proven to monotonically decay from the center of the molecule. This result was contradictory to the theoretical predictions of de Gennes and Hervet but in agreement with computer simulations results [20, 88].

(viii) Dendrimers and cluster formation

Likos et al. in Ref. [91] established a criterion for the formation of full particle overlaps – called *clusters* – for particles interacting via bounded, non-negative potentials. Until that time, cluster formation was explicitly seen in systems of penetrable spheres and it was attributed to the tendency of particles to create free space by forming full overlaps. They showed that clustering occurs in the absence of attraction when the Fourier transform of the potential has oscillatory behavior, i.e. it attains negative values for certain ranges of the wave number. Such potentials are called $Q^{\pm}$ potentials. In order for the criterion to be applicable, these interactions have to be spherically symmetric, to decay sufficiently fast to zero for large distances and to have an existing Fourier transform. Certain model dendrimers [24, 92] were proven to belong in the $Q^{\pm}$-class of bounded potentials [91].

(ix) Dendrimer liquid crystals
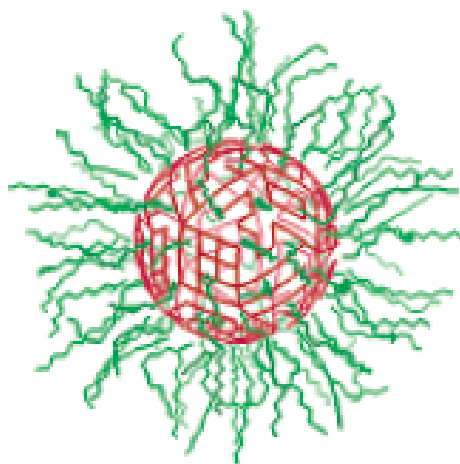
Figure 3.6: $G2$ dendrimer simulation ball model of Li et al. [32]

Li et al. in Ref. [32] presented a spherical model for soft dendrimer balls

(see Fig. 3.6). The core of the sphere consists of hard aromatic groups while the surface is covered with flexible C_{12} alkane chains. By carrying out Molecular Dynamics simulations [60] they found that anisotropic A15 lattice is favoured over FCC and BCC lattices with the soft balls to self-adjust their shape and interactions in different lattices.

(x) Internal structure of PAMAM dendrimers

Maiti et al. in Ref. [17] combined configuration biased Monte Carlo and Molecular Dynamics techniques to successfully characterize the structure of single ethylenediamine (EDA) cored PAMAM dendrimers for several generations. Low generation dendrimers (G2–G5) were found to have the shape of compact ellipsoids-spheroids with a considerable amount of back-folding, whereas higher generations (G9–G11) become more spherical in shape.

(xi) Effective interactions of cluster forming amphiphilic dendrimers

In Ref. [24], Mladek et al. presented a model of second generation amphiphilic dendrimers (see Sec. 3.2.3.2) consisting of a solvophobic core and a solvophilic shell. It was shown that their effective interactions belong to the aforementioned $Q^{\pm}$-potential class and thus they are suitable colloids for cluster formation.

(xii) Monomer resolved simulations of cluster forming amphiphilic dendrimers

Lenz et al. in Refs. [36, 93] verified the validity of the coarse-grained level description for the stability of cluster crystals, i.e. crystals composed of homogeneously sized clusters of overlapping dendrimers, by performing extensive monomer-resolved Monte Carlo simulation of $G2$ amphiphilic dendrimers, predicting also an upper limit for the density for which such crystals can exist.

3.2.3   Dendrimer simulation models

3.2.3.1   General bead spring model

Murat and Grest performed in Ref. [20] the first off-lattice equilibrium Molecular Dynamics (MD) [60, 61] simulations in order to explore the properties of dendrimers. The monomer-monomer pair interaction, $U(r)$, was modeled via a Lennard-Jones potential, ϕ_{LJ} [Eq. (3.9)], truncated and shifted at a cut-off distance r_c which was freely chosen:

$$U(r) = \begin{cases} \phi_{\mathrm{LJ}}(r) - \phi_{\mathrm{LJ}}(r_c), & \text{for } r \leq r_c, \\ 0, & \text{for } r > r_c \end{cases}, \tag{3.8}$$

$$\phi_{\mathrm{LJ}} = 4\varepsilon \left[\left(\frac{\sigma}{r}\right)^{12} - \left(\frac{\sigma}{r}\right)^{6} \right]. \tag{3.9}$$

A cut-off value of $r_c = 2^{1/6}\sigma$ makes the monomer-monomer interaction purely repulsive. The chemical bonds between monomers were modeled via the finite extensible nonlinear

elastic (FENE) [94] potential defined as:

$$U_{\text{FENE}}(r) = \begin{cases} -15\varepsilon \left(\frac{R_0}{\sigma}\right)^2 \ln\left(1 - \left(\frac{r}{R_0}\right)^2\right), & \text{for } r \leq R_0 \\ \infty, & \text{for } r > R_0 \end{cases} \tag{3.10}$$

where σ being is the monomer diameter, $R_0 = 1.5\sigma$ and $T = 1.2\varepsilon/k_{\text{B}}$. The resulting total potential between two adjacent (bonded) beads of the dendrimer separated at a distance r reads

$$U_{\text{tot}}(r) = U(r) + U_{\text{FENE}}(r) \tag{3.11}$$

and is visualized in Fig. 3.7. The bonded beads experience a very strong restoring force both for very short separations (steric repulsion) as well as for separations that approach the bond length scale R_0. The most probable separation is at $r_{min} = 0.97\sigma$, where the total potential U_{tot} has its minimum and thus the total force vanishes.
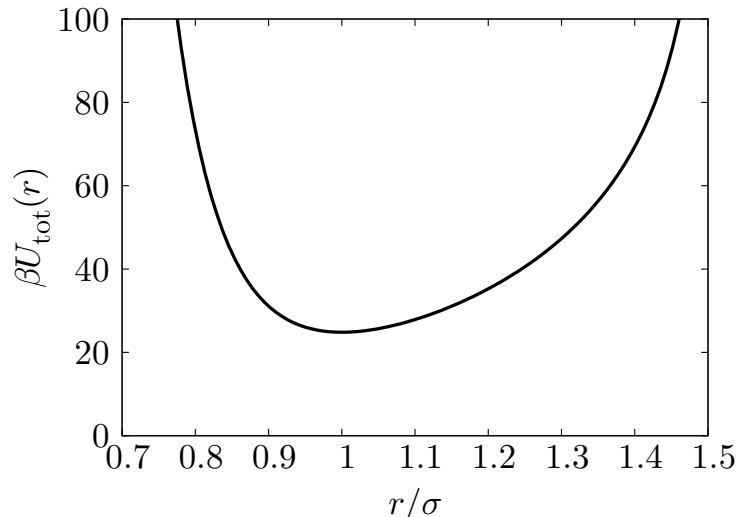
Figure 3.7: Total potential [see Eq. (3.11)] between two adjacent beads of the dendrimer.

3.2.3.2   Amphiphilic dendrimers

Throughout this work we have used the monomer resolved model for amphiphilic dendrimers introduced by Mladek et al. [37, 92], which is based on the model of Welch and Muthukumar [95]. The spacer length of these dendrimers is $P = 1$, while their functionality is $f = 3$. In contrast to the regular dendrimer model, the branching of amphiphilic dendrimers starts from a central bond rather from a central monomer. This results in a total number of monomers $n(G)$ given by the formula:

The total number of monomers in a dendrimer of generation number G is given by

$$n(G) = 2\left(2^{G+1} - 1\right). \tag{3.12}$$

and includes $2^{G+1} - 2$ core monomers and 2^{G+1} terminal shell monomers.

$$G0$$
$$N = 2$$

$$G1$$
$$N = 6$$
$$N_{\text{shell}} = 4$$

$$G2$$
$$N = 14$$
$$N_{\text{shell}} = 8$$

(a)   (b)   (c)
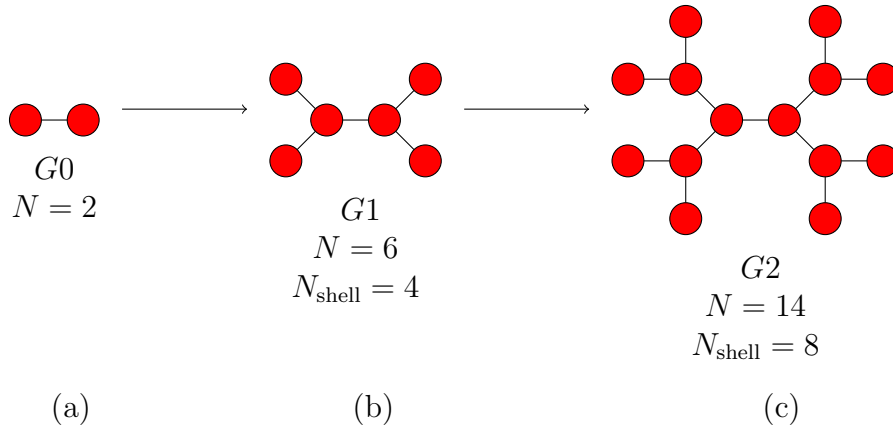
Figure 3.8: Schematic representation of amphiphilic dendrimers, with $f = 3$ and $P = 1$ for generations 0 (a), 1 (b) and 2 (c). We denote with N the total number of monomers while with N_{shell} number of terminal shell monomers.

The inner monomers represent the solvophobic core, labelled by 'C' while the outermost, labelled by 'S', represent the solvophilic shell. This results in a total number of three different interaction types between the beads namely 'CC', 'CS', 'SS'. The bonds are modeled via the finitely extensible nonlinear elastic (FENE) potential [Eq. (3.10)]. In this case we introduce the subscript $\mu\nu$ to denote the different types of interactions induced by the amphiphilic nature of the model; using a different formulation compared to Eq. (3.10) the FENE potential reads

$$\beta\Phi_{\mu\nu}^{\text{FENE}}(r) = -K_{\mu\nu}R_{\mu\nu}^2 \ln\left(1 - \left(\frac{r - l_{\mu\nu}^0}{R_{\mu\nu}}\right)^2\right) \tag{3.13}$$

The difference of the FENE potential to the simple harmonic, "spring" potential is that it restricts the bond length to be in the interval $\left[l_{\mu\nu}^{\min}, l_{\mu\nu}^{\max}\right]$. The $K_{\mu\nu}$ are the spring constants, $R_{\mu\nu} = \left(l_{\mu\nu}^{\max} - l_{\mu\nu}^{\min}\right)/2$ and measure the maximal extension and compression of the bond from the equilibrium length $l_{\mu\nu}^0$, defined as $l_{\mu\nu}^0 = \left(l_{\mu\nu}^{\min} + l_{\mu\nu}^{\max}\right)/2$. All of the dendrimer monomers separated by a distance r interact via a Morse potential:

$$\beta\Phi_{\mu\nu}^{\text{Morse}}(r) = \varepsilon_{\mu\nu}\left\{\left[\exp\left(-\alpha_{\mu\nu}\left(r - d_{\mu\nu}\right)\right) - 1\right]^2 - 1\right\}. \tag{3.14}$$

We focus on two families of model $G4$ dendrimers referred to as D7 [24] and D12. For all interaction parameters we use the diameter of the core monomers d_{CC} as the unit of length. Using this convention, we summarize the interaction potential parameters for the D7-type in Table 3.1. In the case of the D12-type dendrimers the core–core (CC) Morse potential has been truncated and shifted [50] at a distance d_{CC}, while for all other Morse interactions we have introduced a general cut-off distance $r_c = 2.8\,d_{\text{CC}}$ (see inset to Fig. 3.10).

In Fig. 3.9 we give a schematic representation the model dendrimer for a $G2$ dendrimer

FENE	$K_{\mu\nu}d_{CC}^2$	$l_{\mu\nu}^0/d_{CC}$	$R_{\mu\nu}/d_{CC}$
CC	40	1.8750	0.3750
CS	20	2.8125	0.5625
Morse	$\varepsilon_{\mu\nu}$	$\alpha_{\mu\nu}d_{CC}$	$d_{\mu\nu}/d_{CC}$
CC	0.714	6.4	1.00
CS	0.014	19.2	1.25
SS	0.014	19.2	1.50

Table 3.1: Interaction parameters specifying the potentials Eq. (3.13) and Eq. (3.14) for the D7-type and D12-type dendrimers.
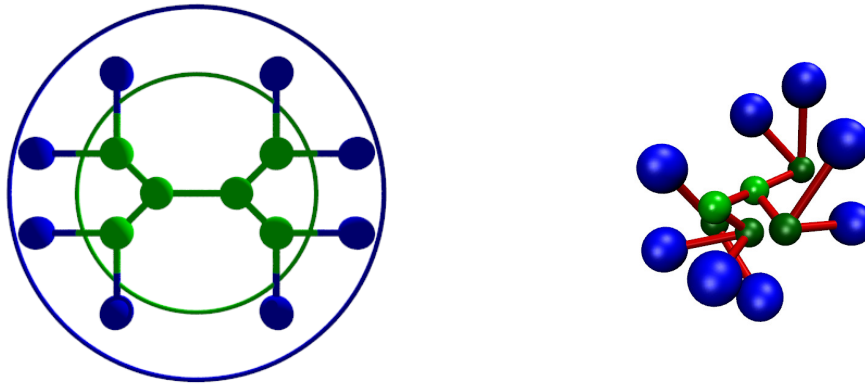
along with a simulation snapshot.

Figure 3.9: Left: Schematic representation of the dendrimer model for $G2$, the core (C) and the shell (S) monomers are colored in green and blue, respectively. Right: A simulation snapshot of a $G2$ D7-type amphiphilic dendrimer.

In Fig. 3.10 we plot the Morse potential for the different types that we have used, i.e. D7 and D12, as well as for the different monomer types (C or S). We use a color coding related the colors used for the different monomer types. The CC interaction is colored in green, the CS interaction in turquoise and the SS in blue color. Following the same color coding we also plot in Fig. 3.11 the FENE potential.
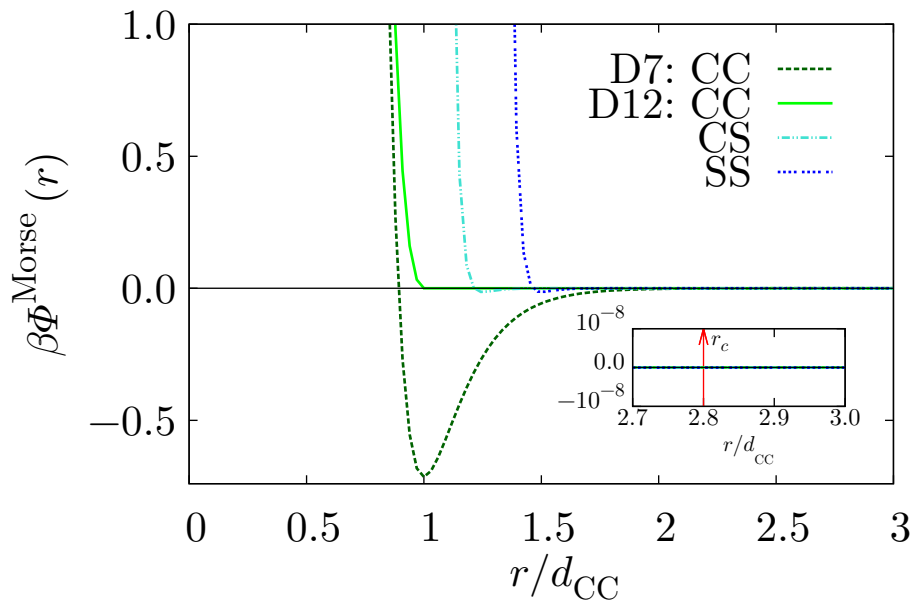
Figure 3.10: Illustration of the Morse interaction potentials between the different types of monomers. The dashed (dark green) and the continuous (light green) line illustrate the CC interaction for the D7- and the D12-type dendrimer. With a dotted-dashed line (turquoise) we represent the CS and with the dotted line (blue) the SS interactions. The inset shows a close-up of the x-axis of the plot at the cutoff radius $r_c = 2.8\, d_{\mathrm{CC}}$ that is used for all interactions except for the D12-type CC interaction where the potential is truncated and shifted at $r_c = d_{\mathrm{CC}}$.
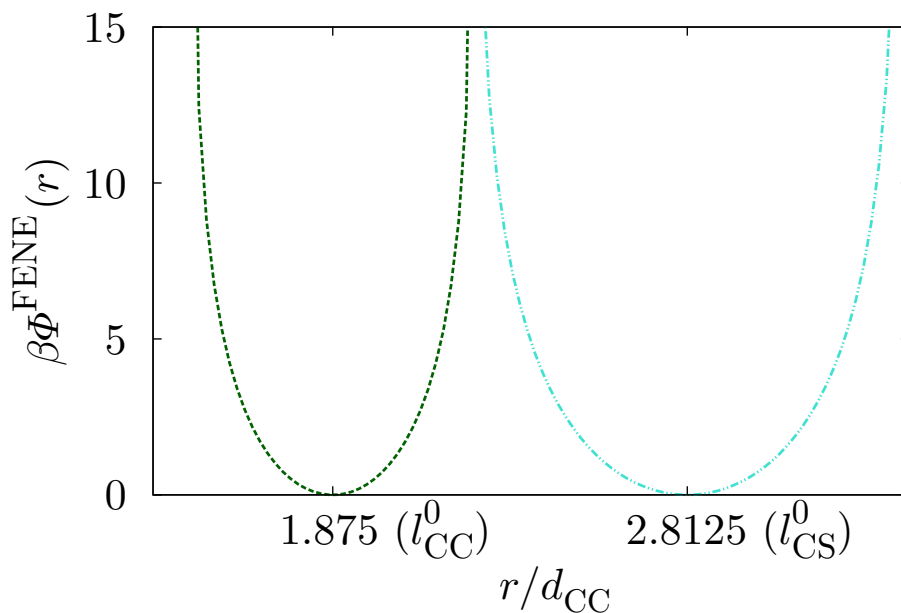
Figure 3.11: Illustration of the FENE interaction potentials between different types of monomers, both for D7- and D12-type dendrimers. We have marked on the x-axis the equilibrium lengths of the CC and CS interactions namely, $l^0_{\mathrm{CC}}/d_{\mathrm{CC}} = 1.875$ and $l^0_{\mathrm{CS}}/d_{\mathrm{CC}} = 2.8125$. We use the same color coding as in Fig. 3.10.

Chapter 4

Liquid crystals in a nutshell

On one hand, the simulation work done by Maiti et al. [cf. Sec. 3.2.2 (x)] suggests that dendrimers are elongated rather than spherical (see Fig. 5 in [17]). On the other hand, from the work of Li et al. [cf. Sec. 3.2.2 (ix)] we can expect that the dendrimers' shape deformation and re-orientation will play role in the way they pack. In this chapter we review the basic theories in liquid crystals as a theoretical framework for the description of the orientational order in dendrimer liquids. As the name suggests, LCs are matter in an intermediate state (*mesophase*), observed between the liquid and the crystal phase. Physically, LCs have the flow properties of liquids but they have also the optical properties of crystalline solids due to the orientational (and partial positional) order.
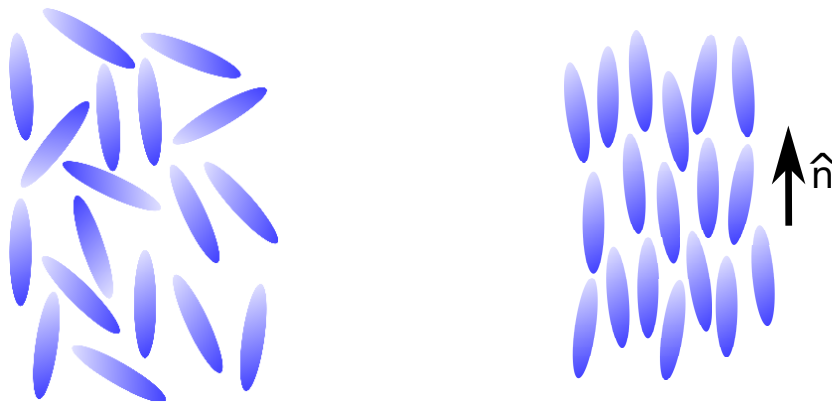
Figure 4.1: Structure of isotropic liquid (left) and of nematic liquid crystal (right). The director $\hat{\mathbf{n}}$ is a unit vector and gives the average direction of the molecules.

The classification of LCs is based on the degree of order in the system. According to their positional and orientational order, LC phases can be classified as follows:

- isotropic phase
- nematic phase
- smectic phase and
- columnar phase.

In Fig. 4.1 we show a schematic of the nematic phase. Here the molecules tend, in contrast to isotropic liquids, to align along the average orientation defined as the *director* $\hat{\mathbf{n}}$, which also specifies the average molecular orientation. Orientations of the director $+\hat{\mathbf{n}}$ and $-\hat{\mathbf{n}}$ are equivalent so that $\hat{\mathbf{n}}$ is a headless rather than a proper vector.

Several models [40, 96] have been developed in order to elucidate the stability of the phases and the transitions between these phases. The Onsager theory gives an insight into the nematic-isotropic (NI) transition [96].

4.1   The Onsager theory

Onsager in Ref. [96] proposed a *hard-rod model* for LCs, which predicts the nematic-isotropic transition. In his theory a 3-dimensional gas of N hard rods of length L and diameter D is considered (see Fig. 4.2) [40, 96]. In this model it is assumed that the energy of interaction between two rods is zero except when they overlap and that the aspect ratio of the rods is large, $(L/D \gg 1)$, the theory is valid for small packing fraction η,

$$\eta = \frac{N}{V}\frac{\pi L D^2}{4} \tag{4.1}$$

with ρ being the number density of the system.

An expression of the Helmholtz free energy $\mathcal{F}$ of a system of hard rods is based on our knowledge on the thermodynamics of ideal gases and systems of finite sized spheres. In a perfect gas the ideal Helmholtz free energy per atom reads

$$\frac{\mathcal{F}^{\text{id}}}{N} = -k_{\text{B}}T\ln\left(a\frac{V}{N}\right) \tag{4.2}$$

Figure 4.2:   Hard rod molecule of length L and diameter D.

where a is a constant. If the gas atoms have a finite volume b then the free volume available per particle particle is:

$$\frac{V_{\text{free}}}{N} = \frac{V - Nb}{N} \tag{4.3}$$

with V_{free} being the free volume available to the all particles. Then, the modified Helmholtz free energy per particle is modified to

$$\begin{aligned}
\frac{\mathcal{F}}{N} &= -k_{\text{B}}T\ln\left(a\frac{V-Nb}{N}\right) \\
&= -k_{\text{B}}T\ln\left(a\frac{V}{N}\left(1-\frac{N}{V}b\right)\right) \\
&\approx \underbrace{-k_{\text{B}}T\ln a}_{\frac{\mathcal{F}_0}{N}} + k_{\text{B}}T\ln\frac{N}{V} + k_{\text{B}}T\frac{N}{V}b
\end{aligned} \tag{4.4}$$

where we have expanded the logarithm $\ln\left(1 - \frac{N}{V}b\right)$ in the dilute limit. Hence the corre-

sponding free energy reads

$$\mathcal{F} = \mathcal{F}_0 + Nk_\mathrm{B}T \ln\left(\frac{N}{V}\right) + Nk_\mathrm{B}T\left(\frac{N}{V}\right)b \qquad (4.5)$$

In the case of hard rods the excluded volume depends also on the relative orientation of the particles. For parallel rods the excluded volume is a cylinder of of radius D and length L totaling to $\pi D^2 L$. For perpendicular rods the excluded volume is a cylinder of ellipsoidal base and length L. It can be shown [40, 97] that the excluded volume per rod is

$$b = DL^2|\sin\gamma| \qquad (4.6)$$

where γ is the angle between the long axes of the rods [see Fig. 4.7]. The orientation of the rods is described by an orientational distribution function $f(\theta)$ so that $f(\theta)\mathrm{d}\Omega$ is the fraction of molecules in a solid angle $\mathrm{d}\Omega$ whose axes' are oriented at an angle θ to the director $\hat{\mathbf{n}}$.
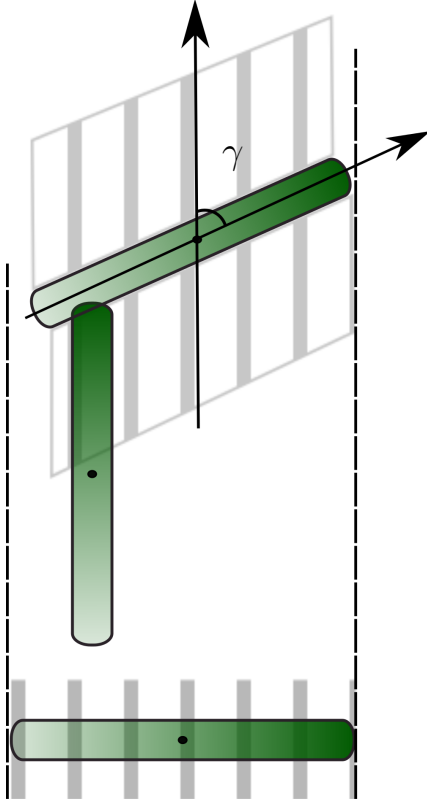
The average values $|\sin\gamma|$ is a functional of the orientational distribution function $f(\theta)$:

$$\langle|\sin\gamma|\rangle = \int \sin\gamma f(\theta)f(\theta')\,\mathrm{d}\Omega\mathrm{d}\Omega' \qquad (4.7)$$

where Ω and Ω' describe the orientations of the two particles in space. The anisotropic distribution of the rod orientations results in a loss of entropy or, equivalently, in an excess free energy difference $\Delta\mathcal{F}^\mathrm{or}$ which according to the Gibbs formula [98] is given by

$$\Delta\mathcal{F}^\mathrm{or} = Nk_\mathrm{B}T \int f(\theta)\ln\left(4\pi f(\theta)\right)\mathrm{d}\Omega. \qquad (4.8)$$

Hence, by substituting Eq. (4.6) into Eq. (4.5) and by including the excess free energy due to the orientation of the molecules [see Eq. (4.8)] we get:

$$\mathcal{F} = \mathcal{F}_0' + Nk_\mathrm{B}T\left\{\ln\left(\frac{N}{V}\right) + \frac{N}{V}DL^2\langle|\sin\gamma|\rangle + \right.$$
$$\left. \int f(\theta)\ln\left(4\pi f(\theta)\right)\mathrm{d}\Omega\right\} \qquad (4.9)$$

Figure 4.3: Relative orientation of rods [40].

where $\langle|\sin\gamma|\rangle$ is given by Eq. (4.7). In terms of packing fraction η the final form of the Onsager free energy reads

$$\mathcal{F} = Nk_\mathrm{B}T\left[\ln\frac{L\eta}{D} + \frac{4}{\pi}\frac{L\eta}{D}\langle|\sin\gamma|\rangle + \int f(\theta)\ln\left(4\pi f(\theta)\right)\mathrm{d}\Omega\right]. \qquad (4.10)$$
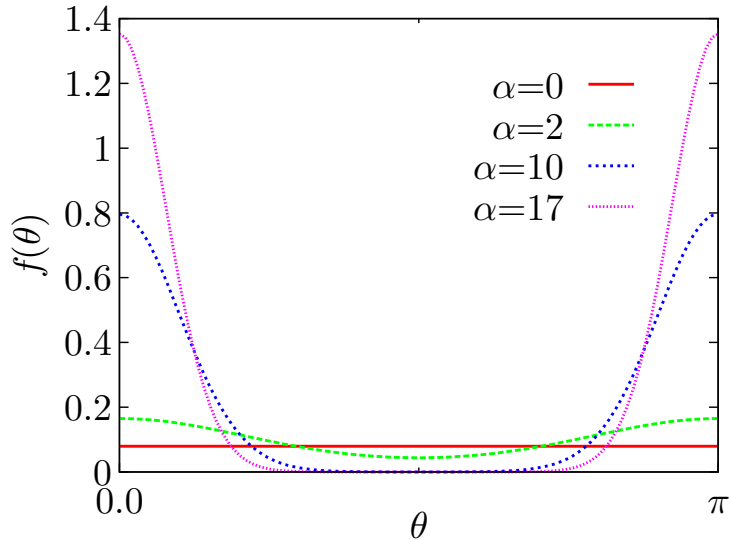
Figure 4.4: Onsager's trial function given in Eq. (4.11) for three representative values of the parameter α. With increasing α sharp peaks develop around $\theta = 0$ and $\theta = \pi$.

In order to determine the minimum of the free energy [Eq. (4.10)], Onsager used in his original publication [96] the following ansatz for $f(\theta)$:

$$f(\theta) = \frac{\alpha \cosh(\alpha \cos \theta)}{4\pi \sinh \alpha} \qquad (4.11)$$

where the parameter α controls the degree of orientational order: when $\alpha = 0$ the distribution is uniform while with increasing α, sharp peaks appear around $\theta = 0$ and $\theta = \pi$ (see Fig. 4.4). Then the free energy was minimized with respect to α. For this particular choice of $f(\theta)$ we can also calculate the degree of orientational order, which is the usual measure of ordering in the nematic phase, given by [2]

$$
\begin{aligned}
S &\equiv \langle P_2(\cos \theta) \rangle && (4.12) \\
&= \frac{1}{2} \int f(\theta)(3\cos^2 \theta - 1) 2\pi \sin \theta \, d\theta, && (4.13)
\end{aligned}
$$

$P_2(x) = (3x^2 - 1)/2$ is the Legendre polynomial of order 2. By substituting Eq. (4.11) into Eq. (4.13) we get

$$S(\alpha) = 1 - 3\frac{\coth \alpha}{\alpha} + \frac{3}{\alpha^2}. \qquad (4.14)$$

As depicted in Fig. 4.5, $S(\alpha)$ is a monotonically increasing function of α, starting from 0 at $\alpha = 0$ and saturating at 1 for $\alpha \to \infty$. For $\alpha \ll 1$, $S(\alpha) \approx \alpha^2/15$ whereas for $\alpha \gg 1$, $S(\alpha) \approx 1 - 3/\alpha$.

Using Onsager's ansatz [see Eq. (4.11)] we can calculate the average value $|\sin \gamma|$ from Eq. (4.7) and plot the Onsager free energy [Eq. (4.10)] as a function of $S(\alpha)$ for different values of $L\eta/D$. An increase of the degree of ordering, associated with the parameter $S(\alpha)$ leads to:
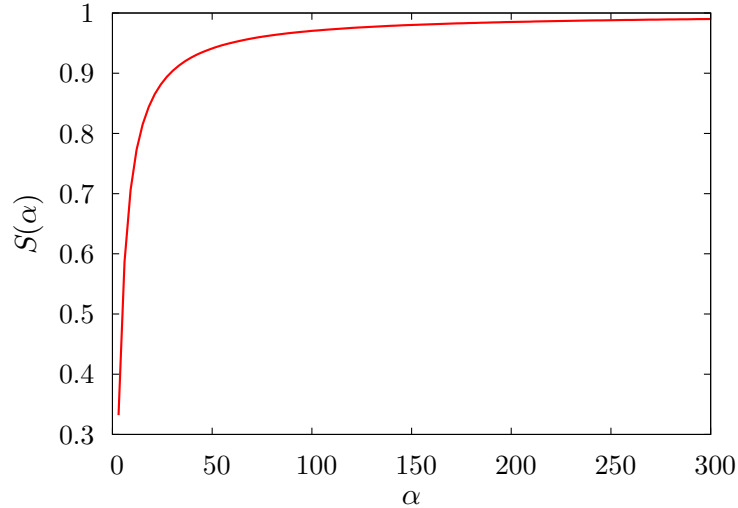
Figure 4.5: Illustration of the order parameter $S(\alpha)$ as function of α defined in Eq. (4.14).

(i) an *increase* in the orientational free energy $N k_\mathrm{B} T \int f(\theta) \ln\left(4\pi f(\theta)\right) \mathrm{d}\Omega$ (loss of orientational entropy) and

(ii) a *decrease* in the free energy $\frac{4}{\pi}\frac{L\eta}{D} \langle |\sin\gamma| \rangle$ emerging from excluded volume interactions: as $S(\alpha) \to 1$ all molecules tend to be parallel and therefore, the excluded volume becomes very small.

The final form of the free energy depends in the quantity $L\eta/D$, i.e. the product of the volume fraction η of the rods as well as on their aspect ratio L/D. In Fig. 4.6 we plot the Onsager free energy as a function of the order parameter $S(\alpha)$. We see that for $L\eta/D < 3.34$ the free energy is minimal at $S = 0$ whereas for values of $L\eta/D > 4.49$ the minimum is located at a finite value of the parameter S, i.e. $S > 0$. Between theses to limit there is a coexistence of the nematic and the isotropic phase.
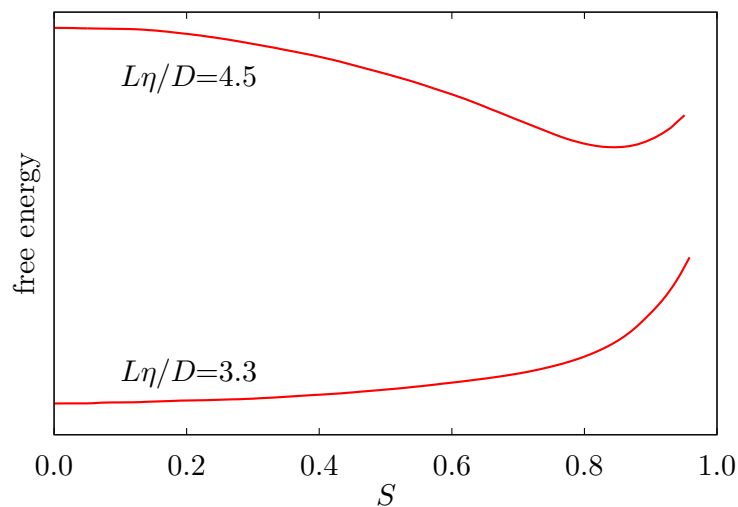
Figure 4.6: The Onsager free energy as a function of the order parameter S. For $L\eta/D = 3.3$ the minimum is at $S = 0$ which corresponds to the isotropic phase. For higher values $L\eta/D = 4.5$ the lowest energy state has nematic order.

Although Onsager theory for hard rods does not predict a correct solution at high densities [97] it provides a qualitative picture of the nematic-isotropic (NI) transition. The anisotropy of the shape of the molecules along with their excluded volume are sufficient for the stabilization of the orientational ordering. This can be also seen from the form of the Onsager free energy in Eq. (4.10) which is athermal, i.e. the temperature T enters only as a prefactor which signals the entropic origin of the orientational order [99]. This does not mean that the interactions between liquid-crystalline molecules or colloids are entirely hard-core; but the steric repulsion between them represents the reference interaction.

4.2   Nematic order parameter

As we have already mentioned, the nematic phase is characterized by a preferred direction specified by the director $\hat{\mathbf{n}}$ as well as by the degree of the nematic order S, see Eq. (4.13). Both quantities can be combined into a second rank tensor called the nematic tensor $\mathbf{Q}$ which captures all aspects of nematic order, i.e. the preferred molecular orientation as well as the magnitude of order. The elements Q_{ij} of the tensor are defined as [40]:

$$Q_{ij} = \frac{1}{N} \sum_{\alpha} \left(l_i^\alpha l_j^\alpha - \frac{1}{3}\delta_{ij} \right), \tag{4.15}$$

where $\mathbf{l}^\alpha$ is a unit vector pointing along the long axis of molecule α while l_i^α is the ith component of $\mathbf{l}^\alpha$. The tensor $\mathbf{Q}$ is symmetric and traceless. In the ordered state the elements of $\mathbf{Q}$ do not vanish. With the x axis along the direction of the molecular alignment, $\hat{\mathbf{n}}$, $\mathbf{Q}$ is diagonal and reads

$$\mathbf{Q} = \begin{bmatrix} 2S/3 & 0 & 0 \\ 0 & -S/3 + P & 0 \\ 0 & 0 & -S/3 - P \end{bmatrix} \tag{4.16}$$

where P is the degree of biaxiality. If P is nonzero, $\mathbf{Q}$ is biaxial [100], and there are two preferred directions.

Usually nematic crystals are uniaxial, i.e. $P = 0$ and there there is only one preferred direction. In this case:

$$Q_{ij} = S \left(n_i n_j - \frac{1}{3}\delta_{ij} \right). \tag{4.17}$$

From the definition of Eq. (4.15)

$$S = \frac{1}{2} \left\langle 3 \left(\mathbf{l}^\alpha \cdot \hat{\mathbf{n}} \right)^2 - 1 \right\rangle = \frac{1}{2} \left\langle 3 \cos^2 \theta^\alpha - 1 \right\rangle \tag{4.18}$$

where θ^α is the angle between the long axis of the molecule α and the director $\hat{\mathbf{n}}$, which specifies the direction of the principal axis of Q_{ij}.

We see that if all molecules point along the director such that $\theta^\alpha = 0$ for all molecules then $S = 1$ [Fig. 4.7(a)]. This state corresponds to perfect nematic order. If the molecules are oriented isotropically, $\langle \cos^2 \theta^\alpha \rangle = 1/3$ and $S = 0$ [Fig. 4.7(b)]; this is the isotropic
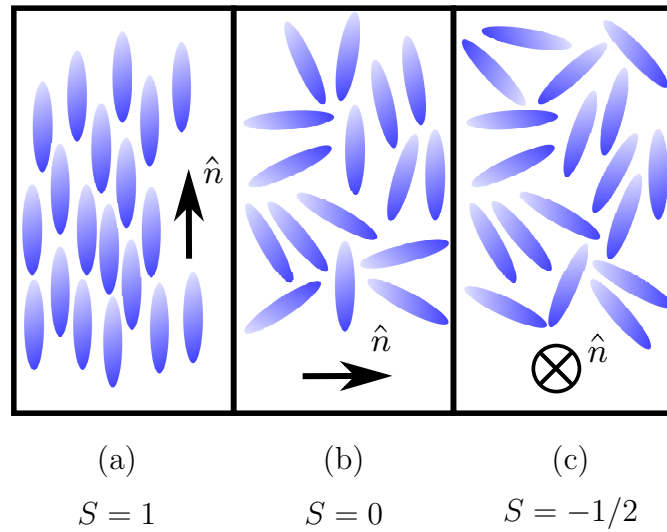
Figure 4.7: Values of the order parameter S [Eq. (4.18)] for perfectly ordered (a), isotropic (b) and perpendicular (c) orientation. The director $\hat{\mathbf{n}}$ is shown in each case.

phase. A special kind of nematic orientational order is that with all molecules perpendicular to the director such that $\theta^\alpha = \pi/2$. In this case $S = -1/2$ [Fig. 4.7(c)].

Chapter 5

Data analysis

In this chapter we summarize the quantities and methods that we used to analyze our simulation data. First we focus on the definition and implementation of the radial distribution function. Then we introduce sample autocorrelation functions as a measure of testing the statistical randomness of our simulation data. Finally, we present the main quantities for characterizing the shape, size and orientation of dendrimers, i.e. the radius of gyration R_{g}, the radius of gyration tensor $\mathcal{S}$, the orientational correlation functions, S and α.

5.1   Radial distribution function

The equilibrium *n-particle density* for a system of fixed N, V and T is defined as [67]:

$$
\begin{aligned}
\rho_N^{(n)}\left(\mathbf{r}^n\right) &= \frac{N!}{(N-n)!}\frac{1}{h^{3N}N!\mathcal{Z}_N}\int\int \mathrm{d}\mathbf{r}^{(N-n)}\mathrm{d}\mathbf{p}^N\exp\left(-\beta\mathcal{H}\left(\mathbf{r}^N,\mathbf{p}^N\right)\right)\\
&= \frac{N!}{(N-n)!}\frac{1}{h^{3N}N!\mathcal{Z}_N}\int\int \mathrm{d}\mathbf{r}^{(N-n)}\mathrm{d}\mathbf{p}^N\exp\left(-\beta\left(\sum_{i=1}^N\frac{|\mathbf{p}_i|^2}{2m}\right)\right)\exp\left(-\beta\mathcal{V}\left(\mathbf{r}^N\right)\right).
\end{aligned}
$$

(5.1)

Performing separately the integration over the momenta, Eq. (5.1) can be written as:

$$
\rho_N^{(n)}\left(\mathbf{r}^n\right) = \frac{N!}{(N-n)!}\frac{1}{z_N}\int \mathrm{d}\mathbf{r}^{(N-n)}\exp\left(-\beta\mathcal{V}\left(\mathbf{r}^N\right)\right).
$$

(5.2)

where z_N is the *configuration integral* defined in Eq. (2.16). The quantity $\rho_N^{(n)}\left(\mathbf{r}^n\right)\mathrm{d}\mathbf{r}^n$ give the probability of finding any n particles of a N-particle system in the volume element $\mathrm{d}\mathbf{r}^N$ [see Eq. (2.1)] irrespective of *all* momenta and of the positions of the remaining $N-n$ particles. Normalization of $\rho_N^{(n)}\left(\mathbf{r}^n\right)$ yields:

$$
\int \mathrm{d}\mathbf{r}^n\rho_N^{(n)}\left(\mathbf{r}^n\right) = \frac{N!}{(N-n)!}
$$

(5.3)

which corresponds to finding n particles among N. In particular, for $n = 1$ and 2 we get:

$$\int d\mathbf{r}^1 \, \rho_N^{(1)} \left(\mathbf{r}^1\right) = N, \tag{5.4}$$

$$\int d\mathbf{r}^2 \, \rho_N^{(2)} \left(\mathbf{r}^2\right) = N \left(N - 1\right). \tag{5.5}$$

Thus, for a uniform fluid the one-particle density is identical to the number density ρ of the system:

$$\rho_N^{(1)} \left(\mathbf{r}\right) = \frac{N}{V} \equiv \rho. \tag{5.6}$$

It is also useful here to introduce another special case of a density function, i.e. the pair density function for an ideal gas, i.e. a theoretical gas composed of non-interacting, randomly moving particles. In this case, Eq. (2.16) reduces to $z_N = V^N$ with V being the volume of the system. Therefore, it follows from Eq. (5.2) that the pair density function is:

$$\rho_N^{(2)} = \rho^2 \left(1 - \frac{1}{N}\right). \tag{5.7}$$

We can re-express the one-particle density using the Dirac delta function as:

$$\rho_N^{(1)} \left(\mathbf{r}\right) = \left\langle \sum_{i=1}^N \delta \left(\mathbf{r} - \mathbf{r}_i\right) \right\rangle. \tag{5.8}$$

Equivalently, for the two-particle density we get:

$$\rho_N^{(2)} \left(\mathbf{r}, \mathbf{r}'\right) = \left\langle \sum_{i=1}^N \sum_{j=1}^N \delta \left(\mathbf{r} - \mathbf{r}_i\right) \delta \left(\mathbf{r}' - \mathbf{r}_j\right) \right\rangle. \tag{5.9}$$

Now, we can define the pair distribution function as:

$$g_N^{(2)} \left(\mathbf{r}_1, \mathbf{r}_2\right) = \frac{\rho_N^{(2)} \left(\mathbf{r}_1, \mathbf{r}_2\right)}{\rho_N^{(1)} \left(\mathbf{r}_1\right) \rho_N^{(1)} \left(\mathbf{r}_2\right)}. \tag{5.10}$$

For a homogeneous system we have $\rho_N^{(1)} \left(\mathbf{r}\right) = \rho$ and thus, Eq. (5.10) takes the form:

$$\rho_N^{(n)}(\mathbf{r}^n) = \rho^n g^{(n)}(\mathbf{r}^n). \tag{5.11}$$

Additionally, for a system that is isotropic the pair distribution function $g^{(2)} \left(\mathbf{r}_1, \mathbf{r}_2\right)$ depends only on the separation $r = |\mathbf{r}_1 - \mathbf{r}_2|$ between the particles and it is also called *radial distribution function* $g(r)$ (RDF) [61, 62]:

$$g(r) = \frac{\rho_N^{(2)} \left(r\right)}{\rho^2}. \tag{5.12}$$

It can be shown [67] that:

$$\left\langle \frac{1}{N} \sum_{i=1}^{N} \sum_{j=1}^{N} \delta\left(\mathbf{r} - \mathbf{r}_j + \mathbf{r}_i\right) \right\rangle = \frac{1}{N} \int d\mathbf{r}' \rho_N^{(2)}\left(\mathbf{r}' + \mathbf{r}, \mathbf{r}'\right). \tag{5.13}$$

Thus, from Eq. (5.12) and Eq. (5.13) we have:

$$\rho g(r) = \frac{1}{N} \left\langle \sum_{i=1}^{N} \sum_{j=1}^{N} \delta\left(\mathbf{r} - \mathbf{r}_j + \mathbf{r}_i\right) \right\rangle. \tag{5.14}$$

The calculation of $g(r)$ in a simulation performed within a cubic box of side length L and where periodic boundary conditions (cf. Sec. 2.3.1) are applied, is restricted within a distance equal to $L/2$. This is due to the spatial periodicity in each of the directions of the central unit cell. Computationally the calculation of RDF is as follows:

(i) We create an empty histogram of N_{bin} bins and of a spatial step Δr and of range $[0, L/2]$. We denote with i the bin number which ranges from 0 to $N_{\text{bin}} - 1$.

(ii) We calculate for each bin i the number of pairs whose distance is between $i\,\delta r$ and $(i+1)\,\delta r$. Note that according to Eq. (5.14), each distinct pair should be counted twice in the histogram. This way, if $N_{\text{dp}}(r)$ is the number of distinct pairs of particles then the number of pairs in the bin is $2N_{\text{dp}}(r)$.

(iii) The term $\rho g(r)\Delta V$ gives the probability of finding a particle inside the volume element ΔV and at a distance r from a reference particle [see Fig. 5.1]. Thus, we can approximate Eq. (5.14) by:

$$\rho g\left((i + 0.5)\,\delta r\right) = \frac{2N_{\text{dp}}(r)}{N\delta V} \tag{5.15}$$

where $\delta V = V_{i+1} - V_i$ with $V_i = \frac{4}{3}\pi\,(i\delta r)^3$.

The quantity $g(r)$ of a system is of special importance since its Fourier transform [101], known as the structure factor $S(k)$ [see Eq. (5.16)], can be experimentally measured using, for example, *small-angle neutron scattering* (SANS) [102] and *small-angle X-ray scattering* techniques (SAXS) [103]. The structure factor is related to the RDF via relation [104]:

$$S(k) = 1 + \frac{4\pi\rho}{k} \int_0^\infty [g(r) - 1]\, r \sin(kr)\mathrm{d}r \tag{5.16}$$

where ρ is the density of the system, and k is the scattering wavevector modulus defined by:

$$k = \frac{4\pi}{\lambda} \sin(\theta/2). \tag{5.17}$$

A typical RDF calculated from MC simulation of a hard-sphere fluid system presented in Sec. 2.4.1 and for a number density $\rho = 0.6\,\sigma^{-3}$ is shown in Fig. 5.2. The x-axis is in units of particle diameter σ.
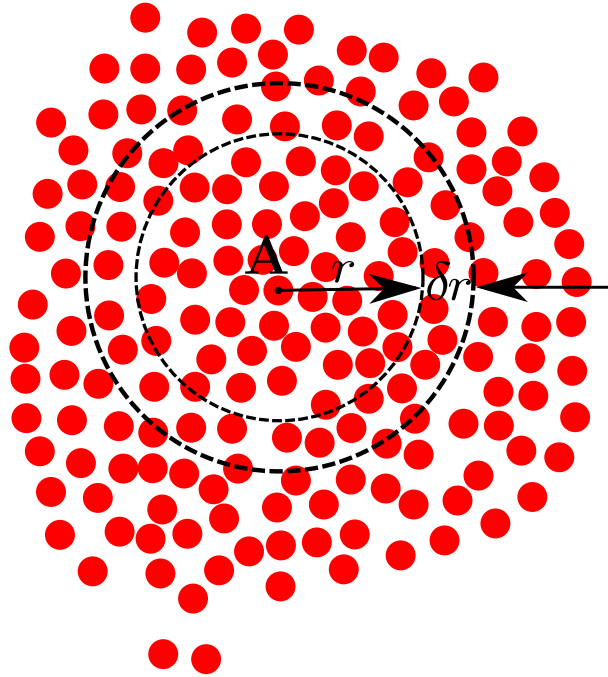
Figure 5.1: Schematic representation of the shell ΔV used for the calculation of $g(r)$ and located at a distance r from a reference particle **A**. The volume δV of the shell is given by $\delta V = \frac{4}{3}\pi \left[(i+1)^3 - i^3\right]\delta r^3$.
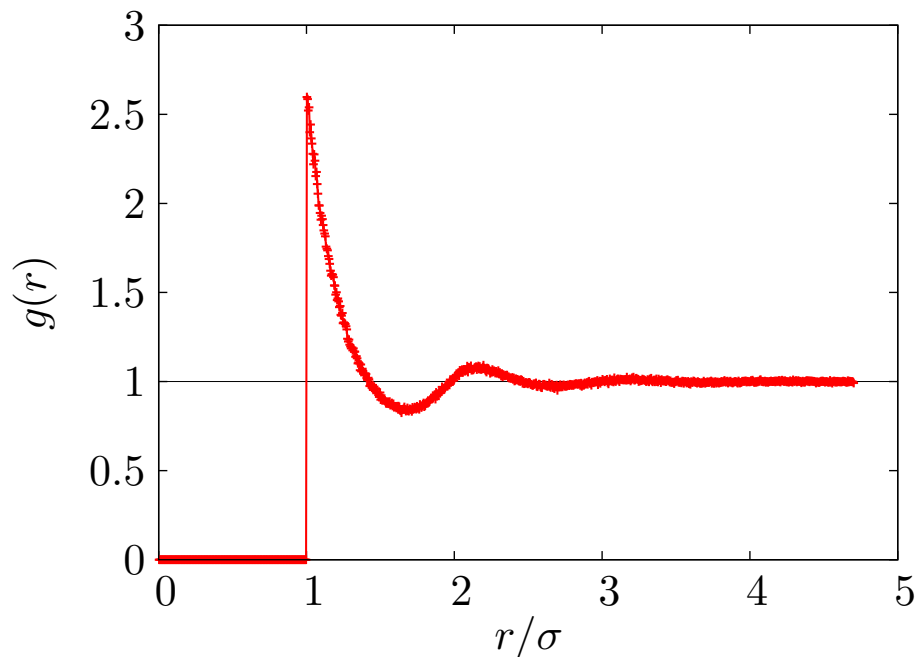

Figure 5.2: Radial distribution function calculation from MC simulation of a hard-sphere fluid at a density $\rho = 0.6\,\sigma^{-3}$ and for $N = 500$ particles.

At short distances, $r \in [0, 1.0)$, $g(r)$ is zero as a result of the strong repulsion between the particles [see Eq. (2.62)]. At $r = 1.0\sigma$ we see the largest peak with $g(1.0) \approx 2.6$.

5.2   Sample autocorrelations

5.2.1   Autocorrelation function

Autocorrelation refers to the linear dependence of an observable quantity with itself at two points in time. Suppose that during the production steps of an MC simulations we measure the value of an observable quantity A. We define as a *time series* a set, also called a *sample set*, of M equi-spaced in time measurements of the quantity A, namely $\{A_1, A_2, \ldots A_M\}$. Then, the *lag-k autocorrelation coefficient* is given by [105, 106]

$$r_k = \frac{C_k}{C_0} \tag{5.18}$$

where C_k is the *autocovariance function* at lag k is defined as

$$C_k = \frac{1}{M} \sum_{t=1}^{M-k} \left(A_t - \overline{A}\right) \left(A_{t+k} - \overline{A}\right) \tag{5.19}$$

and C_0 is the variance function

$$C_0 = \frac{1}{M} \sum_{t=1}^{M} \left(A_t - \overline{A}\right)^2 \tag{5.20}$$

where $\overline{A}$ is the mean value of A over all values M. Note that in the bibliography a different definition of c_k can be found, i.e.:

$$C_k = \frac{1}{M-k} \sum_{t=1}^{M-k} \left(A_t - \overline{A}\right) \left(A_{t+k} - \overline{A}\right), \tag{5.21}$$

but the difference between Eqs. (5.19) and (5.21) is small for large values of M [107].

The coefficient r_k is used to detect correlation between the two values, A_t and A_{t+k} at times t and $t+k$, respectively. The sample *autocorrelation function*, or simply ACF, for a time series is the sequence of the autocorrelation coefficients C_k for $k = 0, 1, \ldots, M-1$. If we compare the time series with itself, which is the *zero-lag* case, the correlation coefficient r_0 will be exactly 1.0. In order to determine the correlation coefficient for the first lag, we offset the lag by one time step, i.e. we set $k = 1$. We can continue offsetting the time series by an additional step in order to get higher lags coefficients. Note that each time we increase the lag k by one the number of points that are used in the sum of Eq. (5.18) decreases by two. Thus, it is not recommended to calculate autocorrelation coefficients for lags greater then half the sample size M, i.e. the relation $k < M/2$ must hold during the calculation [106, 107].

The plot of the ACF as a function of lag k is called *autocorrelation plot* or *correlogram* [107]. Using correlograms we can interpret a set of autocorrelation coefficients $\{r_k\}$[1]. Autocorrelation plots are used as a tool for checking randomness of of a dataset $\{A_M\}$. If the data is random, the autocorrelation coefficients should be near zero for all timelags $k > 0$. As an example, we generated 1000 random points and then compared the

---

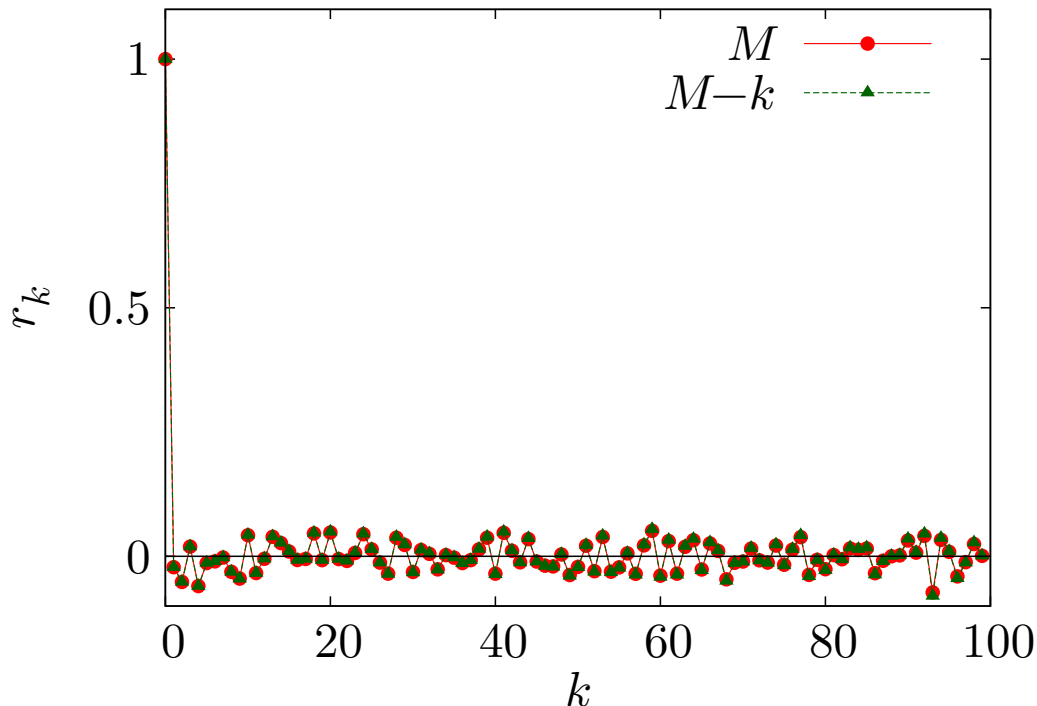[1]A general advice on how to interpret a correlogram is given in Ref. [107].

Figure 5.3: Correlogram of the ACK calculated for a sample of 1000 random numbers and for the first 100 lags. We illustrate with filled circles (red) the results using Eq. (5.19) and with filled triangles (green) using Eq. (5.21). Notice that the value of r_k approaches zero for all $k > 0$ which shows that this time series was created through a random process.

first 100 lags of the ACF shown in Fig. 5.3. We calculate the ACF using both Eqs. (5.19) and (5.21) in order to show that the results do not differ irrespective of whether we divide the sum with M or with $M - k$.

5.2.2   Autocorrelation function of R_{g}

If we, during a Monte Carlo simulation, sample after every move then we create a highly correlated sample set since after every move the point created in the phase space is very close to the initial point. As a result, we end up with an underestimation of the true error of an observable quantity A. In order to get results of the averaged quantities of interest, we have to create a set of independent points in the phase space that are not close to one another.

Throughout this thesis, our criterion for determining equilibration and statistical independence of the configurations is based in the calculations of the radius of gyration R_g of a macromolecule [cf. Sec. 3.2.1] which is known to relax very slowly [108]. Based on the definition in Eq. (5.18), the autocorrelation function [51, 109] of the radius of gyration R_g for different lags k is defined as:

$$\phi_{R_{\mathrm{g}}}(k) = \frac{\overline{[R_g(t+k) - \sum R_g][R_g(t) - \sum R_g]}}{\overline{[R_g(t) - \sum R_g]^2}}. \tag{5.22}$$

Here the time t is measured in terms of Monte Carlo sweeps and $\overline{\cdots}$ denotes the average calculated as: $\frac{1}{M} \sum_{t=1}^{M} \cdots$. where M is the number of different equi-spaced in time measurements of R_g. We typically find that the correlation of R_g decreases exponentially with the number of Monte Carlo steps. The characteristic time of this exponential is called the *relaxation time* τ_{rel} and is defined as the time required for $\phi_{R_g}(k)$ to decrease to $1/e \, (\approx 0.368)$ of its initial value.

This way we can have an estimate of the decorrelation time τ_0 by [110]:

$$\tau_0 = -\frac{\tau}{\ln r_1} \tag{5.23}$$

This suggest that if the value of the first lag r_1 is $1/e$ then there is a very good chance that our sample set is composed of statistical independent measurements.

5.3 Shape and orientation analysis

5.3.1 Radius of gyration

The fundamental quantity for the characterization of the size of a macromolecule is its radius of gyration R_{g} (cf. Sec. 3.2.1, see Fig. 5.4). We repeat here for convenience the formula for calculating the squared radius of gyration of a macromolecule consisting of N monomers, i.e.:

$$
\begin{aligned}
R_{\mathrm{g}}^2 &= \frac{1}{N} \left\langle \sum_{i=1}^{N} (\mathbf{r}_{\mathrm{i}} - \mathbf{R}_{\mathrm{CM}})^2 \right\rangle \\
&= \frac{1}{N} \left\langle (x - x_{\mathrm{CM}})^2 + (y - y_{\mathrm{CM}})^2 + (z - z_{\mathrm{CM}})^2 \right\rangle
\end{aligned}
\tag{5.24}
$$

where $\mathbf{R}_{\mathrm{CM}}$ denotes the position vector of the center-of-mass, located at $(x_{\mathrm{CM}}, y_{\mathrm{CM}}, z_{\mathrm{CM}})$, expressed in the same coordinate system used for the position vector of particle i, $\mathbf{r}_i$. R_{g} is used to characterize the overall size of a macromolecule.

5.3.2 Radius of gyration tensor

By itself the radius of gyration R_{g} does not provide information concerning the shape and orientation of a macromolecule. When calculating the components $(\tau - \tau_{\mathrm{CM}})^2$, with $\tau = x$ or y or z, of R_g then we expect that the following relation will hold for the average values [111]:

$$\left\langle (x - x_{\mathrm{CM}})^2 \right\rangle = \left\langle (y - y_{\mathrm{CM}})^2 \right\rangle = \left\langle (z - z_{\mathrm{CM}})^2 \right\rangle = \frac{R_{\mathrm{g}}^2}{3}. \tag{5.25}$$

since there is no preference in the orientation of the macromolecule in space. Thus, after averaging over a very large number of different and independent conformations, the shape of the macromolecule can be approximated by a sphere of radius R_{g}.
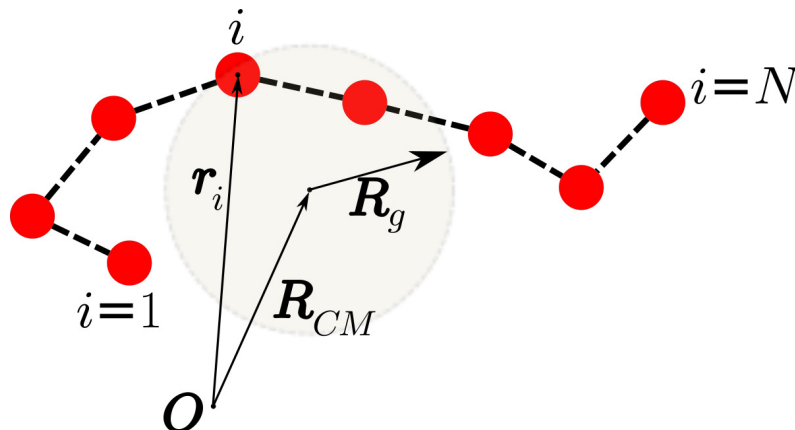
Figure 5.4: Schematic representation of the radius of gyration R_{g} for a given macromolecule consisting of N monomers. We denote with $\mathbf{O}$ the origin, with $\mathbf{R}_{\mathrm{CM}}$ the position of the center-of-mass while $\mathbf{r}_i$ is the position vector of the i-th monomer.

By its definition the R_{g} is a measure of the size of the macromolecule which can hardly characterize its shape. It was Kuhn who first pointed out in 1934 [112] that although the long-time averages of the quantities in Eq. (5.25) should be spherically symmetric in space, this is not in general true for an instantaneous chain conformation [113]. Later, Šolc and Stockmayer [113, 114] employed the radius of gyration tensor (RGT) as a way of characterizing the shape of the instantaneous chain conformations. Since then the RGT has been extensively used [87, 111, 115–117] as a measure of shape for polymers.

The RGT $\mathcal{S}$ is a tensor whose components $\mathcal{S}_{\tau\tau'}$ are constructed from the dyadic of the position column vector $\mathbf{r}_i = (x_i, y_i, z_i)^T$ in a frame of reference with its origin located at the center of mass of the macromolecule. Thus:

$$\mathcal{S}_{\tau\tau'} = \frac{1}{N} \sum_{i=1}^{N} (\tau_i - \tau_{\mathrm{CM}})(\tau_i' - \tau_{\mathrm{CM}}') \tag{5.26}$$

where $\tau = x, y, z$. Therefore,

$$\mathcal{S} \equiv \begin{bmatrix} \mathcal{S}_{xx} & \mathcal{S}_{xy} & \mathcal{S}_{xz} \\ \mathcal{S}_{yx} & \mathcal{S}_{yy} & \mathcal{S}_{yz} \\ \mathcal{S}_{zx} & \mathcal{S}_{zy} & \mathcal{S}_{zz} \end{bmatrix}$$

$$= \begin{bmatrix} \sum (x_i - x_{\mathrm{CM}})^2 & \sum (x_i - x_{\mathrm{CM}})(y_i - y_{\mathrm{CM}}) & \sum (x_i - x_{\mathrm{CM}})(z_i - z_{\mathrm{CM}}) \\ \sum (x_i - x_{\mathrm{CM}})(y_i - y_{\mathrm{CM}}) & \sum (y_i - y_{\mathrm{CM}})^2 & \sum (y_i - y_{\mathrm{CM}})(z_i - z_{\mathrm{CM}}) \\ \sum (x_i - x_{\mathrm{CM}})(z_i - z_{\mathrm{CM}}) & \sum (y_i - y_{\mathrm{CM}})(z_i - z_{\mathrm{CM}}) & \sum (z_i - z_{\mathrm{CM}})^2 \end{bmatrix} \tag{5.27}$$

with the shorthand $\sum \cdots$ we denote a summation over all particles $\frac{1}{N} \sum_{i=1}^{N} \cdots$. By definition $\mathcal{S}$ is a real, symmetric 3×3 matrix. The squared radius of gyration [cf. Eq. (5.24)] is given by the trace of $\mathcal{S}$, i.e. $R_{\mathrm{g}}^2 = \mathcal{S}_{\mathrm{xx}} + \mathcal{S}_{\mathrm{yy}} + \mathcal{S}_{\mathrm{zz}}$. This trace, as the first invariant of $\mathcal{S}$, is independent of the orientation of the reference system. However, in the absence of

spherical symmetry, the individual elements $\mathcal{S}_{\tau\tau}$ of the RGT depend on the orientation of the reference system.

5.3.2.1 Eigenvalues and eigenvectors

Following the convention introduced by Theodorou et al. [115] we chose a particle-reference system so that $\mathcal{S}$ is diagonal, i.e.:

$$\mathcal{S}_{\mathrm{diag}} = \begin{bmatrix} E_1 & 0 & 0 \\ 0 & E_2 & 0 \\ 0 & 0 & E_3 \end{bmatrix} = \mathrm{diag}\,(E_1, E_2, E_3) \tag{5.28}$$

where E_1, E_2 and E_3 are the three eigenvalues arranged in descending order, i.e. $E_1 \geq E_2 \geq E_3$ while $\hat{\boldsymbol{\epsilon}}_1$, $\hat{\boldsymbol{\epsilon}}_2$, and $\hat{\boldsymbol{\epsilon}}_3$ are the corresponding eigenvectors. This matrix $\mathcal{S}$ has three invariants $\mathrm{Tr}\,(\mathcal{S})$, $\mathrm{D}\,(\mathcal{S})$ [118, 119] and $\mathrm{M}\,(\mathcal{S})$, where $\mathrm{Tr}\,(\mathcal{S})$ is the trace, $\mathrm{D}\,(\mathcal{S})$ is the determinant and $\mathrm{M}\,(\mathcal{S})$ is the sum of its principal minors[2] M_{11}, M_{22}, M_{33}, i.e.

$$\begin{aligned} \mathrm{M} &= M_{11} + M_{22} + M_{33} \\ &= \mathcal{S}_{xx}\mathcal{S}_{yy} + \mathcal{S}_{xx}\mathcal{S}_{zz} + \mathcal{S}_{yy}\mathcal{S}_{zz} - \mathcal{S}_{xy}\mathcal{S}_{yx} - \mathcal{S}_{xz}\mathcal{S}_{zx} - \mathcal{S}_{yz}\mathcal{S}_{zy}. \end{aligned} \tag{5.29}$$

Therefore in terms of eigenvalues we have [120]:

$$\mathrm{Tr}\,(\mathcal{S}) = E_1 + E_2 + E_3, \tag{5.30}$$
$$\mathrm{D}\,(\mathcal{S}) = E_1 E_2 E_3, \tag{5.31}$$
$$\mathrm{M}\,(\mathcal{S}) = E_1 E_2 + E_1 E_3 + E_2 E_3. \tag{5.32}$$

The size and shape of macromolecules can be characterized by quantities expressed in terms of the eigenvalues of $\mathcal{S}$.

5.3.2.2 Shape analysis

As already mentioned, the trace of $\mathcal{S}$ is defined as the squared radius of gyration R_{g}^2 [cf. Eq. (5.28)]:

$$\mathrm{Tr}\,(\mathcal{S}) = \frac{1}{N} \sum_{i=1}^{N} \left(x_i^2 + y_i^2 + z_i^2 \right) = R_{\mathrm{g}}^2. \tag{5.33}$$

If the macromolecule is isotropic in all directions, then we can approximate its shape with an effective sphere center located at its centers-of-mass and of radius R_{g}. On the other hand, deviations from spherical symmetry macromolecules can be approximated by three additional measurements which can be derived by comparing the traceless form of the gyration tensor defined as [87]:

$$\hat{\mathcal{S}} = \mathcal{S} - \frac{1}{3}\,\mathrm{Tr}\,(\mathcal{S})\,\mathrm{diag}(1, 1, 1) \tag{5.34}$$

---

[2]The minor M_{ij} of the entry in the ith row and j^{th} column of a squared matrix is the determinant of the submatrix formed by deleting the ith row and the jth column.

with an analogous traceless tensor used by Smith and Mortensen in Ref. [121],

$$\hat{S} = b \, \text{diag} \left(2/3, -1/3, -1/3 \right) + c \, \text{diag} \left(0, 1/2, -1/2 \right). \tag{5.35}$$

This way, the asphericity b and the acylindricity c are defined as

$$b = E_1 - \frac{1}{2} \left(E_2 + E_3 \right), \quad b \geq 0 \tag{5.36}$$

$$c = E_2 - E_3, \quad c \geq 0. \tag{5.37}$$

The asymmetry can be also expressed by in terms of the average values $\langle E_1/E_2 \rangle$ and $\langle E_1/E_3 \rangle$. These quantities provide information about deviations of the model dendrimer from the spherical and cylindrical symmetry respectively. The combination $b = c = 0$ can correspond to the spherical symmetric case, but not exclusively; for instance $b = c = 0$ for tetrahedral or cubic symmetry.

A different definition for the asphericity δ was given by Rudnick and Gaspari in Ref. [119]

$$\delta = \frac{\text{Tr}^2 \left(\mathcal{S} \right) - 3\text{M} \left(\mathcal{S} \right)}{\text{Tr}^2 \left(\mathcal{S} \right)} = 1 - 3 \frac{E_1 E_2 + E_1 E_3 + E_2 E_3}{\left(E_1 + E_2 + E_3 \right)^2}. \tag{5.38}$$

The quantity δ takes the value of 1 for rod-like molecules while for molecules with spherical symmetry it vanishes, i.e. $\delta = 0$. Using these three eigenvalues of the radius of gyration tensor we can approximate the shape of the macromolecule as an ellipsoid located at the center-of-mass and with the eigenvalues $\sqrt{E_1}$, $\sqrt{E_2}$ and $\sqrt{E_3}$ being its *semi-axes*.

5.3.3   Orientation analysis

An orientation can be assigned to the macromolecules with no spherical symmetry by means of the eigenvectors extracted from the radius of gyration tensor, by interpreting $\hat{\epsilon}_1$ and $\hat{\epsilon}_3$ as the directions of maximum and minimum extension, respectively. This also allows us to quantify the relative orientation of two macromolecules separated by a center of mass distance r. It is possible to calculate *orientational correlation functions* (OCF) [122, 123] that depend on the relative orientation of the macromolecules. The OCFs allow to describe the degree of the relative orientation between the macromolecules. The most commonly used OCF is defined as:

$$S(r) = \langle P_2 \left(\cos \theta \right) \rangle_{r-\delta r, r+\delta r} \tag{5.39}$$

where $P_2 \left(\cos \theta \right)$ is the second order Legendre polynomial [124], θ is the relative angle between the long axes of the macromolecules described by the unit vectors $\hat{\epsilon}_{1i}$ and $\hat{\epsilon}_{1j}$ (Fig. 5.5). Thus,

$$S(r) = \left\langle \frac{1}{2} \left[3 \left(\hat{\epsilon}_{1i} \cdot \hat{\epsilon}_{1j} \right)^2 - 1 \right] \right\rangle_{r-\delta r, r+\delta r} \tag{5.40}$$

The OCF $S(r)$ takes the value 1 for perfectly aligned molecules, $-1/2$ for perpendicular and 0 for randomly oriented molecules and can be calculated in a similar manner to the RDF (cf. Sec. 5.1). In the bibliography the aforementioned quantity is also referred to as the *Herman's orientation function* [125–127].
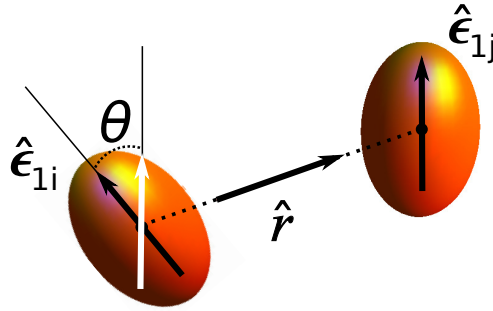
Figure 5.5: Schematic representation of the long axes of $\hat{\boldsymbol{\epsilon}}_{1i}$ and $\hat{\boldsymbol{\epsilon}}_{1j}$, needed to describe the respective orientations of molecules which are here represented by axisymmetric ellipsoids. With the symbol θ we denote the angle between $\hat{\boldsymbol{\epsilon}}_{1i}$ and $\hat{\boldsymbol{\epsilon}}_{1j}$ such that $\cos\theta = \hat{\boldsymbol{\epsilon}}_{1i} \cdot \hat{\boldsymbol{\epsilon}}_{1j}$, $\hat{\boldsymbol{r}}$ being the the unit center-to-center vector between molecules i and j.

The quantity $S(r)$ depends only on the angle between the vectors $\hat{\boldsymbol{\epsilon}}_{1i}$ and $\hat{\boldsymbol{\epsilon}}_{1i}$ and contains no information for the relative position of the two macromolecules. It is a way of representing a property of the phase space rather than the phase space itself. Another way of characterizing each configuration of two molecules is by using

$$\alpha = \frac{1}{2} \left[(\hat{\boldsymbol{\epsilon}}_{1i} \cdot \hat{\mathbf{r}})^2 + (\hat{\boldsymbol{\epsilon}}_{1j} \cdot \hat{\mathbf{r}})^2 \right], \tag{5.41}$$

where $\hat{\boldsymbol{\epsilon}}_{1i}$ and $\hat{\boldsymbol{\epsilon}}_{1j}$ are the directional unit vectors of the long axes of the dendrimers and $\hat{\mathbf{r}}$ is the unit center-to-center vector (see Fig. 5.5). Note that using α is symmetric with respect to an interchange of dendrimers $(1 \leftrightarrow 2)$ as well as to replacing $\hat{\boldsymbol{\epsilon}}_{1i}$ by $-\hat{\boldsymbol{\epsilon}}_{1i}$, reflecting thereby properly the headless nature of the molecules. Furthermore, this quantity takes into account not only the relative orientation but also the relative position of the molecules.

Chapter 6

Results

In this chapter we summarize the results obtained for isolated dendrimers but also for pair of dendrimers in the zero-density limit as well as in the bulk. We study two different types of dendrimers, referred to as D7- and D12-type, specified in Sec. 3.2.3.2.

6.1   Isolated dendrimers

We first investigate the shape and the size of single isolated dendrimers, with the generation number ranging from $G = 2$ with 14 monomers up to $G = 10$ with a total of 4094 monomers. The initial configurations for each dendrimer were constructed such that the bond lengths between the monomers are within the maximum extension $R_{\mu\nu}$ of the FENE potential [see Eq. (3.13)]. We used standard NVT MC simulations with the conventional Metropolis acceptance criterion (cf. Sec. 2.2) and simulation parameters as specified in Table 3.1.

6.1.1   Autocorrelation function

During the simulation runs, the positions of the monomers were recorded for configurations that were sufficiently uncorrelated. In order to determine the optimum sampling frequency of the configurations we used autocorrelation plots as defined in Sec. 5.2. All the quantities that were investigated – i.e the asphericity b, the acylindricity c, the acylindricity δ as defined by Rudnick and Gaspari [38] and the radius of gyration R_{g} – are generated from the radius of gyration tensor, thus their autocorrelation functions have the same behavior. Yet, we chose to present correlations using R_{g} since it is already known from the bibliography to relax very slowly [108]. We computed autocorrelation functions $\phi_{R_{\mathrm{g}}}(k)$ (see Eq. (5.22)) of R_{g} at varying timelags k. As we have seen in Fig. 5.3, if a dataset is completely random then

$$\phi_{R_{\mathrm{g}}}(k) \simeq 0, \text{ for all } k \neq 0. \tag{6.1}$$

As an example, we plot the first 30 time lags in Fig. 6.1 of the sample autocorrelation function (ACF) of R_{g} for a $G10$ dendrimer of type $D7$, in the inset the 500 sampled values of R_{g} that were used for the calculation of the ACF are also plotted. The time interval between two successive measurements is 5×10^5 Monte Carlo sweeps (MCS). These data suggest that our sample of data is sufficiently uncorrelated. This means that

we can use this data sample to calculate ensemble averages and error of the quantities of interest [106].
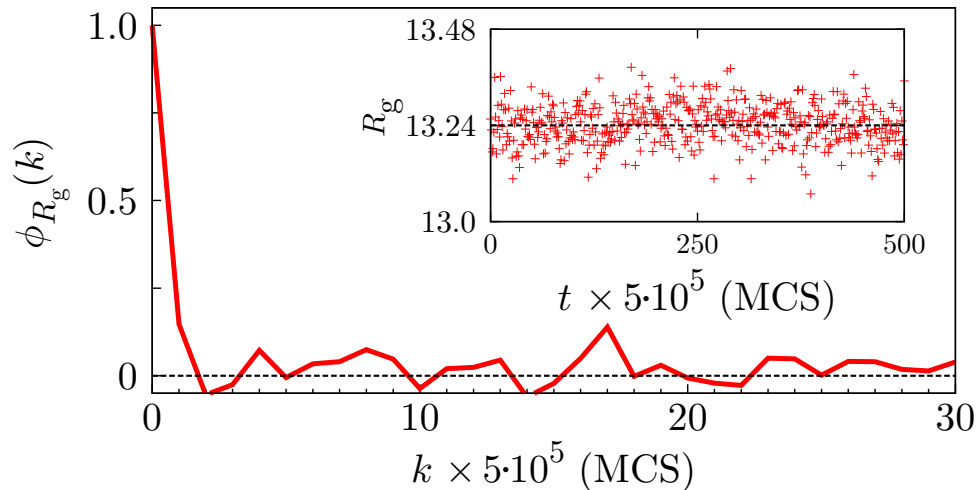
Figure 6.1: Sample autocorrelation function [see Eq. (5.22)] of R_g for a $G10$ dendrimer of type $D7$ and for the first 30 lags. The form of the curve suggests that our data for R_g are sufficiently uncorrelated. The inset shows the R_g measurements at each sampled timestep where the dashed line indicates the compute average value of R_g. Here the timestep and the time lags k are measured in Monte Carlo sweeps (MCS).

6.1.2   Shape analysis

G	$n(G)$	D7			D12		
		R_g^0	E_1/E_2	E_1/E_3	R_g^0	E_1/E_2	E_1/E_3
2	14	2.89(0.27)	1.99(0.76)	4.13(1.77)	2.94(0.26)	1.99(0.73)	4.17(1.75)
3	30	3.51(0.28)	1.82(0.60)	3.20(1.10)	3.67(0.25)	1.76(0.53)	3.19(1.04)
4	62	4.27(0.27)	1.70(0.48)	2.79(0.80)	4.54(0.23)	1.59(0.38)	2.59(0.68)
5	126	5.33(0.23)	1.56(0.34)	2.45(0.59)	5.57(0.19)	1.44(0.26)	2.13(0.43)
6	254	6.55(0.17)	1.37(0.21)	1.92(0.34)	6.77(0.15)	1.32(0.17)	1.76(0.26)
7	510	7.92(0.13)	1.26(0.13)	1.58(0.18)	8.15(0.12)	1.24(0.12)	1.52(0.16)
8	1022	9.47(0.10)	1.20(0.08)	1.39(0.11)	9.72(0.09)	1.20(0.08)	1.38(0.10)
9	2046	11.24(0.07)	1.17(0.06)	1.29(0.06)	11.52(0.06)	1.17(0.05)	1.28(0.06)
10	4094	13.24(0.05)	1.15(0.04)	1.24(0.05)	13.53(0.04)	1.15(0.03)	1.23(0.03)

Table 6.1: Single dendrimer properties as functions of the generation number G. We have denoted with $n(G)$ the total number of monomers. Also given, are the radius of gyration R_g, and the ratios of the principal moments E_1/E_2 and E_1/E_3 (cf. Sec. 5.3.2.1). The sample standard deviation is shown in brackets. The parameters of the dendrimers are given in Table 3.1.

For the low generations dendrimers $G = 2$ to 6 we sampled over ten while for the higher generations $G = 7$ to 10 over twenty independent initial configurations. We used the autocorrelation function of R_g in order to determine the equilibration of the system as well as the optimal sampling frequency. Depending on the dendrimer's generation the sampling frequency ranges from 5×10^3 to 5×10^6 MC sweeps and was chosen according to the form of the R_g autocorrelation function. Once the system has reached equilibrium we performed simulations over a period of 10^8 sweeps during which the position of all monomers were recording. Then we used the monomer coordinated in order to compute the elements of the radius of gyration tensor $\mathcal{S}$ (see Eq. (5.27)) as well as its eigenvalues and eigenvectors. The asphericity b and the acylindricity c of the isolated dendrimer could be then determined from Eqs. 5.36 and 5.37, respectively. Additionally, we computed the R_g^0 with the help of Eq. (5.33). In Table 6.1 we present the quantities describing the size and shape of D7- and D12-type dendrimers of generations $G = 2$ to 10. In the same table we also include for completeness the number of the total monomers $n(G)$.
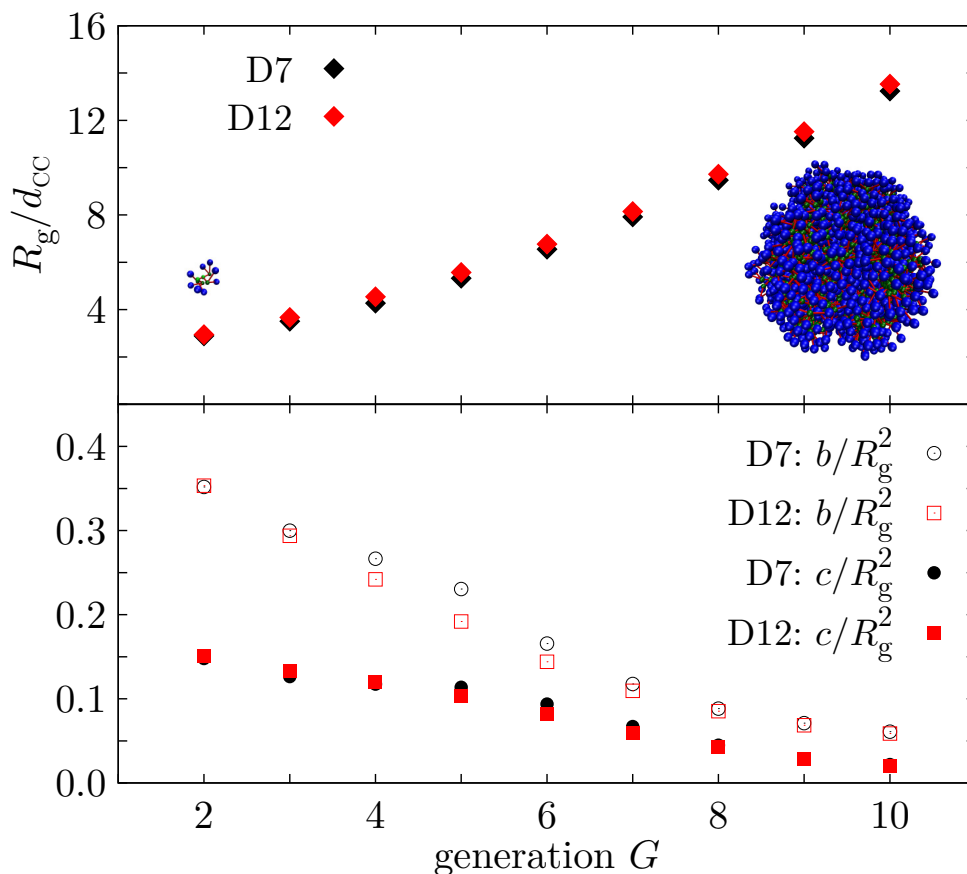
Figure 6.2: The radius of gyration R_g (top) and the asphericity b (empty symbols) and acylindricity c (full symbols) in units of R_g^2 (bottom) as function of generation number G for isolated dendrimers of type D7 and D12. The insets in the top panel show typical simulation snapshots of D7-type dendrimers of generation $G = 2$ and 10.

The top panel of Fig. 6.2 shows the results for the radius of gyration R_g^0 whereas the bottom panel these for the asphericity b and acylindricity c. One one hand we observe that R_g increases with the generation number G. On the other upon changing the dendrimer

type from D7 to D12 its size, in terms of R_g, remains the same. Hence the purely repulsive interactions between core monomers in the D12-dendrimers induce only a small additional stretching of the internal bonds with respect to those for dendrimers of type D7; this additional stretching results in a slightly larger value of the R_g. Also, the data for our amphiphilic dendrimers follow the simple scaling law $R_g^0 \sim n^a(G)$ in terms of the total number of monomers $n(G)$ with an exponent $a = 0.318 \pm 0.004$. This value of a is consistent with the one reported for PAMAM dendrimers [17].

Our most important finding is that the shape of dendrimers is in general not spherical but prolate. As we can see in the bottom panel of Fig. 6.2 the asphericity and the acylindricity of D7- and D12-type dendrimers decrease monotonically with G in a similar fashion. Therefore, there is a significant change in the shape of dendrimers while going from low to high generations. For both types of dendrimers and for generations $G = 2$ and 3 we find highly asymmetric shapes while for generations with $G \geq 8$ nearly spherical shapes. The effect of the dendrimer's type on its shape becomes more pronounced for intermediate values of G, i.e. $G = 4$ to $G = 6$, where the differences between the b values become non-negligible.

(a)   (b)
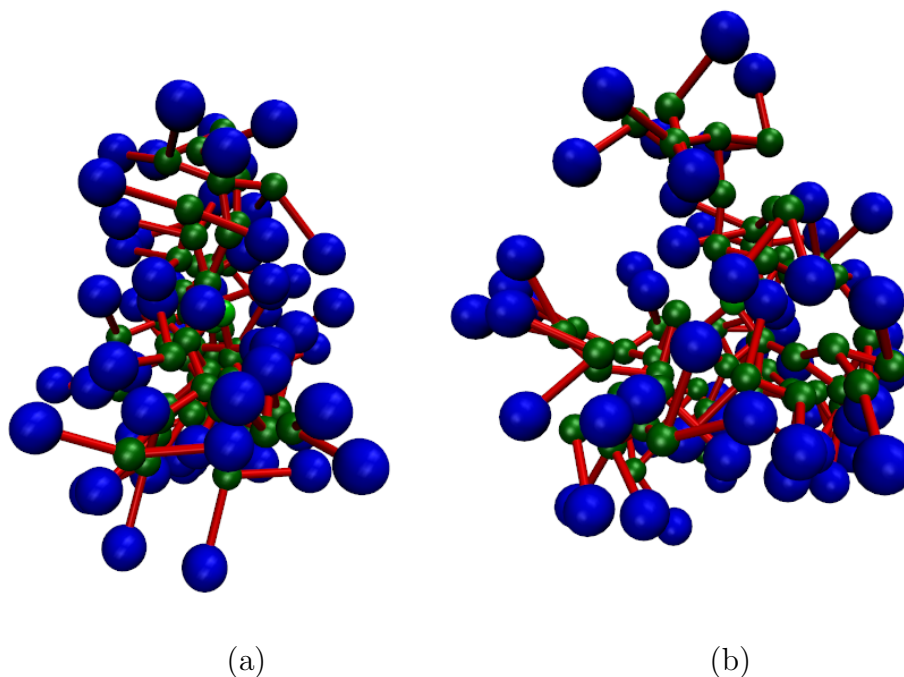
Figure 6.3: Simulation snapshot of G5 dendrimers of (a) D7- and (b) D12-type dendrimers. The purely repulsive nature of the D12-type dendrimers (b) results in a more open structure compared

For generations $G = 2$ and 3 the nature of core-core monomer interaction is of lower importance since the large lengths of the bonds between the monomeric units provide enough space for the additional core monomers to distribute themselves within the core region. As the core region becomes denser, $G \geq 4$ to $G = 6$, on one hand the short range interaction between the core monomers become more significant but on the other, there are not enough shell monomers to fully dominate the structure. In this regime, the

purely repulsive core-core interactions of the D12-type results in slightly more open and more spherical shape compared to that of the D7-type. In an effort to visualize these differences we show in Fig. 6.3 simulation snapshots of $G5$ dendrimers of both D7- and D12-type; we can see that the D12-type $G5$ dendrimer exhibits a slightly more spherical shape compared to the D7-type. In the range from $G = 7$ to 10 both models exhibit essentially the same shape; the dendrimer's core are strongly populated and therefore there is no additional space for outer core or shell monomers to penetrate the inner of the core; the nature of the interaction becomes again irrelevant.

In this case, the dendrimer cores are strongly populated and there is little space left for any additional outer core or shell monomers to penetrate the inner core so their repulsive or attractive interaction does not play any important role.

Finally, we present the results for the asphericity δ as defined by Rudnick and Gaspari [119] (see Sec. 5.38) which is also used in Ref. [17] for the characterization of shape of PAMAM dendrimers. We observe theat the asphericity drops monotonically from $G = 0$ to 10 to $\delta \approx 0$ following the same trend as the asphericity b (see bottom panel of Fig. 6.2).
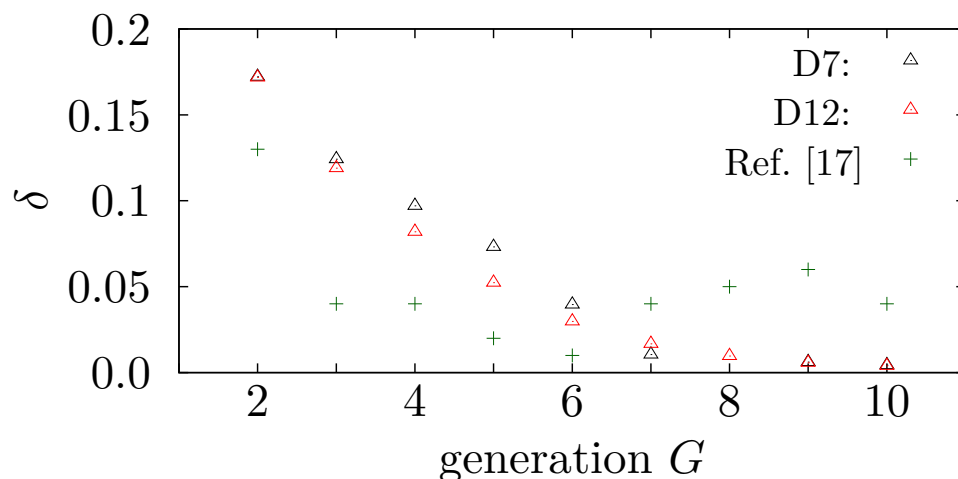
Figure 6.4: Asphericity δ as function of generation number G for isolated dendrimers of type D7 (black triangles) and D12 (red triangles). We also include the results of Maiti et al. [17] for the asphericity δ of PAMAM dendrimers.

Similar results for the overall shape properties of dendrimers can be found in the work of Naylor et al. [128]. Their results also indicated a dramatic change in the morphology with the generation G. More specifically, generations $G = 1 - 3$ where found to be highly asymmetric ($E_1/E_3 = 4.4 - 2.7$) whereas generations $G = 4 - 7$ nearly spherical ($E_1/E_3 = 1.3$) with a transition between two forms ($E_1/E_3 = 1.7$) occurring at generation $G = 4$.

6.1.3   Density profiles

To get a better insight into the microscopic structure of our dendrimer models, we computed the density profiles of dendrimers with $G = 2$–10 and of type D7 and D12. For each generation we measured separately the density profiles for the core and the shell

monomers which are depicted in Fig. 6.5 and where we have scaled the distances r with the radius of gyration R_{g}. By comparing these different profiles, we find that:

(i) For $G = 2-4$ [see Figs. 6.5 (a)-(c)] the core and shell monomers are more segregated. The overall density profile is inhomogeneous with the maximum of the distribution of the core monomers located close to the origin ($r = 0$). The shell distribution peaks around $r = 0.8 - 0.85R_{\mathrm{g}}$ and then falls off towards the surface.

(ii) For $G = 5$ [see Fig. 6.5(d)] the core monomer distribution of D12 develops a first peak at $r \approx 0.1R_{\mathrm{g}}$ whereas the shell distribution develops a plateau.

(iii) For $G \geq 6$ a clear layer-like structure appears with the core distribution of both models developing peaks characteristic for each different generations. Similar layer structure as well as the broadening of the plateau of the shell monomer distribution has been observed in the results obtained for lower generation dendrimers ($G = 4$ and 5) using the FENE-Lennard-Jones model described in Sec. 3.2.3.1 (see also Refs. [29, 129]). In contrast, the shell monomer distribution starts developing an almost constant plateau indicating of the back-folding of the shell monomers to the interior of the core.

(iv) For $G = 10$ the shell monomer distribution plateau is almost constant indicating the limiting generation for this type of dendrimers.

The differences between the two models (D7 and D12) can be seen in the combined plots for different generations presented in Fig. 6.6. The most pronounced difference is seen for generation $G = 2 - 4$ at the origin ($r = 0$) which arises from the different nature of the core-core interaction. In particular, in the case of D12 it is repulsive while for the D7 it is attractive leading to a lower value in the distribution for the case of D12. For $G = 2 - 4$ the density profile $\rho(r)$ develops a peak at $r = 0$ and then falls off towards the surface. From $G = 5$ and up to $G = 10$ the overall density becomes homogeneous while developing multiple peaks for the different generations.

In the next section, we study the effective interaction between dendrimers of generations $G = 2$ and 4 in the zero density limit and we relate it to the shape deformation due to the mutual presence as well as to the relative orientation of the dendrimers.
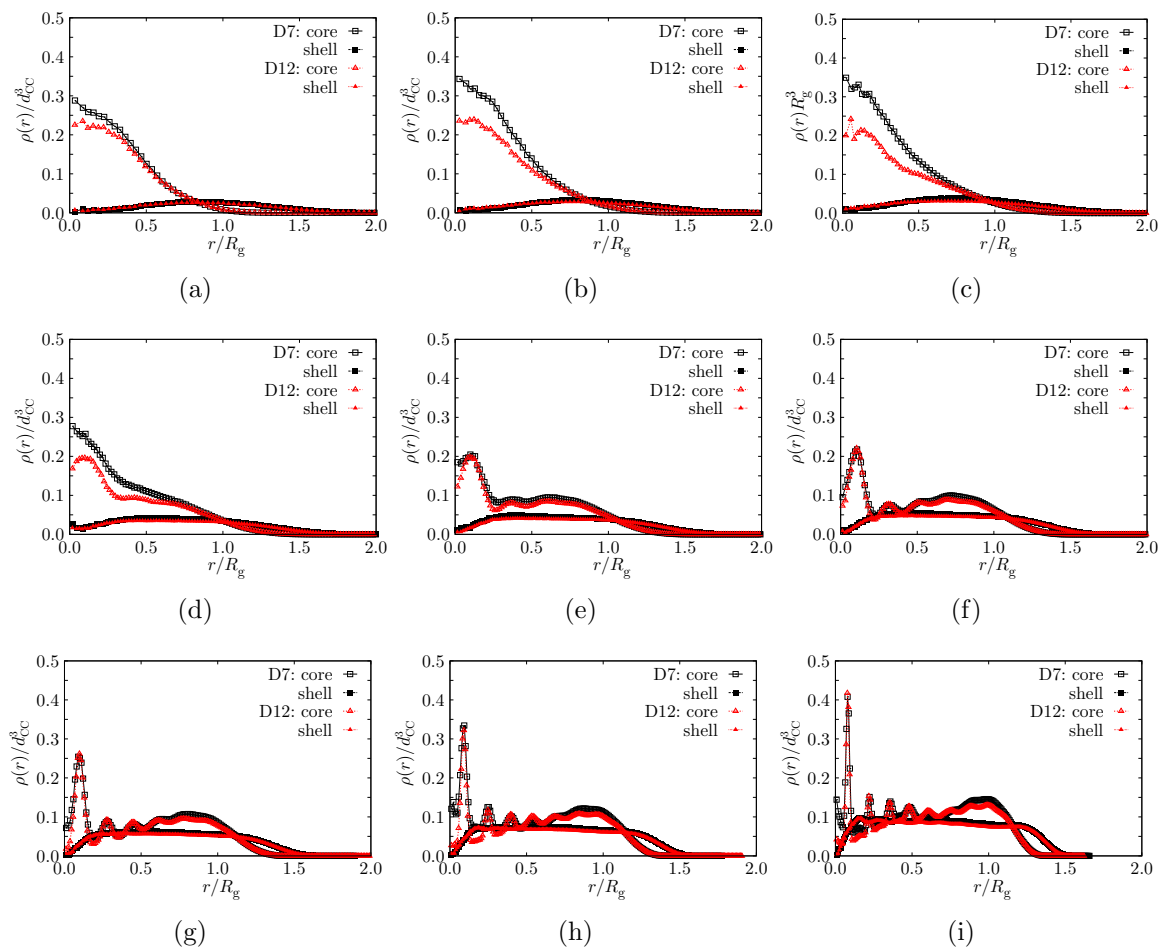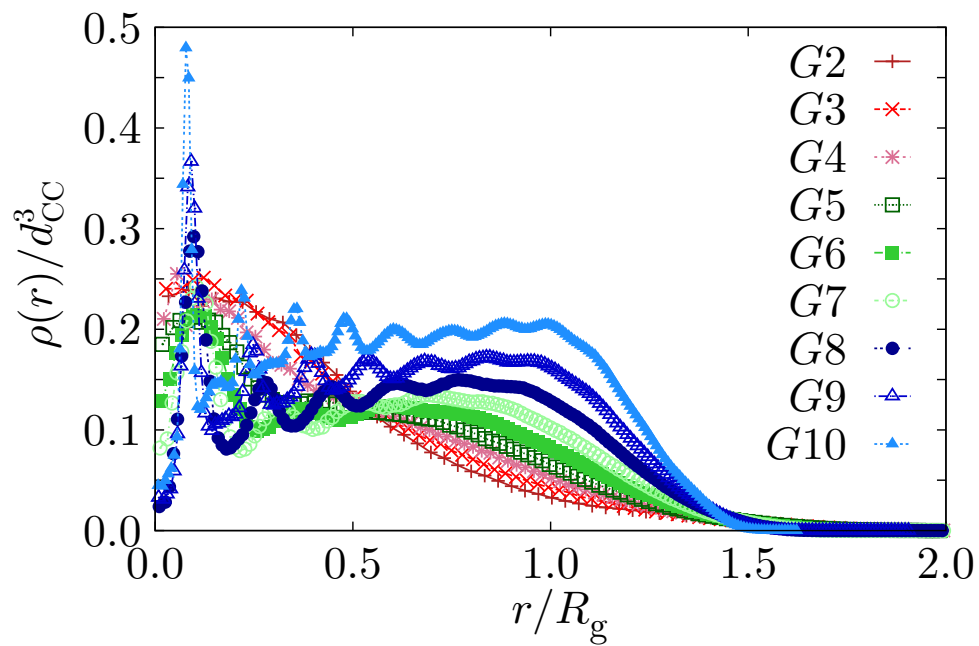
Figure 6.5: Density profiles of D7- (black squares) and D12-type (red triangles) isolated dendrimers for the core (empty symbol) and the shell (filled symbol) regions as a function of the distance r from the dendrimer's center of mass and for generations $G2$ (a), $G3$ (b), $G4$ (c), $G5$ (d), $G6$ (e), $G7$ (f), $G8$ (g), $G9$ (h), $G10$ (i).
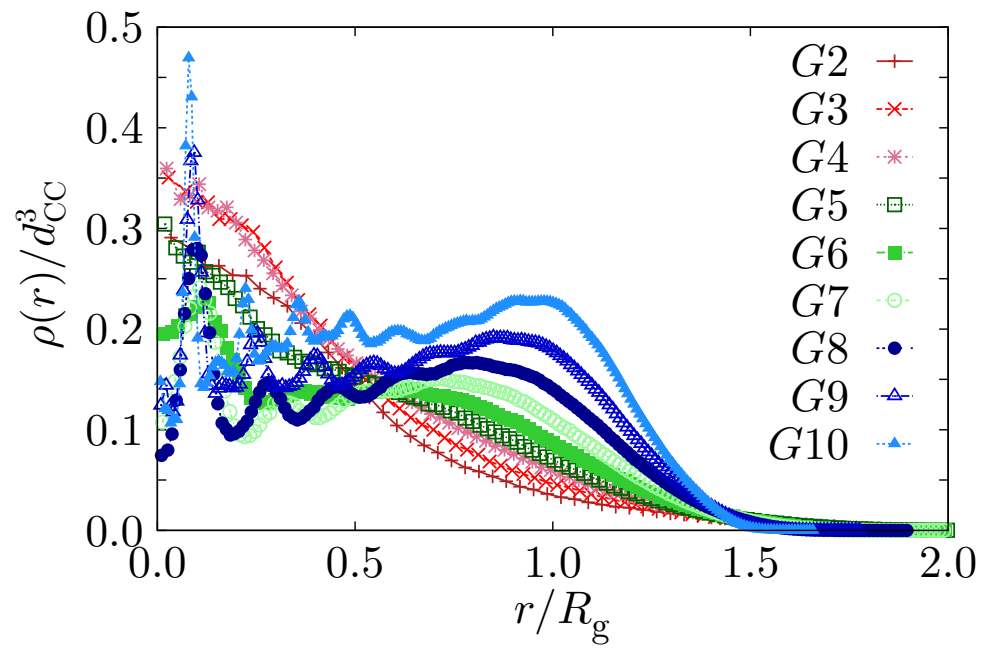
Figure 6.6: Total density profiles for generations $G = 2 - 10$ as a function of the scaled distance r/R_{g} for D7-(a) and D12-type (b).

6.2   Two interacting dendrimers

In order to quantify the mutual influence in the shape of the two dendrimers, we fixed their centers of mass at a distance R chosen from the dendrimer-dendrimer interaction range $R = 0$ to $R_{\max} \simeq 4\,R_{\mathrm{g}}^0$ with R_{g}^0 being the radius of gyration of the isolated dendrimer (this method is referred to as the fixed CM approach). For each distance R we measured the shape and the relative orientations of the two dendrimers with a sampling frequency of 2×10^3 sweeps and for a total 2×10^8 Monte Carlo sweeps. In order to confirm that this is an appropriate method for studying the mutual influence in the shape of dendrimers, we also extracted the effective interaction by integrating the force from the configuration data from the fixed CM approach (see Sec. 2.4.3.3) and compared it with the effective interaction obtained from the umbrella sampling (see Sec. 2.4.3.1) as well as with the one obtained from the Widom particle insertion method (see Sec. 2.4.1). For the purpose of saving computational time, we initially tested the different methods for extracting the effective interactions for the case of $G2$ dendrimers. Then, we focused on the shape and orientational analysis of D7- and D12-type $G4$ dendrimers.

6.2.1   Effective Interactions
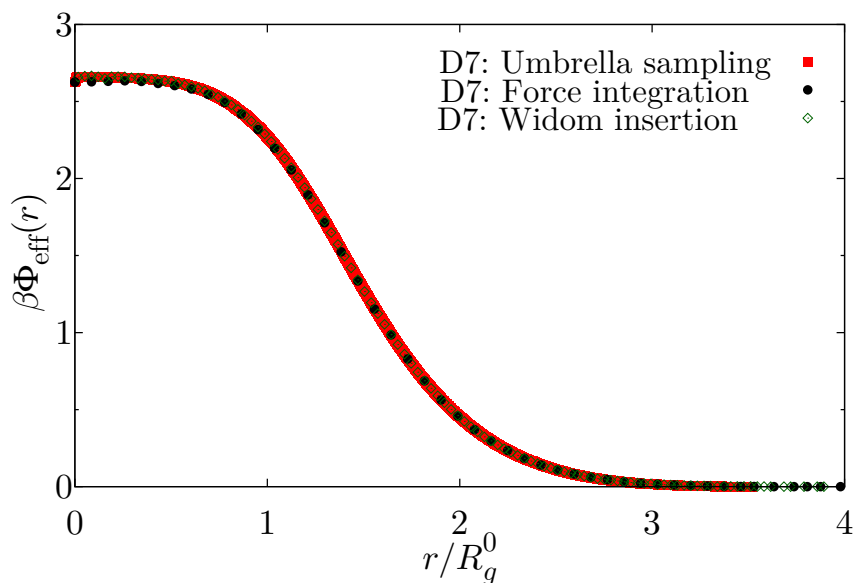
Figure 6.7: Comparison between different methods for obtaining the dimensionless effective interaction $\beta\Phi_{\mathrm{eff}}(r)$ between two $G2$ dendrimers of D7-type.

We first compare the effective interactions obtained by different techniques for the case of D7-type $G2$ dendrimers. In the case of the fixed CM approach, we performed 3×10^8 MC sweeps starting from ten independent initial configurations. For the Widom method we sampled the dendrimers over 2×10^6 MC sweeps, in each on of which we first decorrelated each dendrimer for 280 MC moves (single monomer moves) and then we used the resulting configurations to sample 1000 distances between the two dendrimers as described in Sec. 2.4.1. For the umbrella sampling method we used 33 overlapping windows for a maximum range $R_{\max} \simeq 4\,R_{\mathrm{g}}^0$. In each window we sampled for 4×10^7

MC sweeps. The effective pair interactions obtained are sketched in Fig. 6.7. We observe that the methods produce identical results. The aforementioned methods produce also
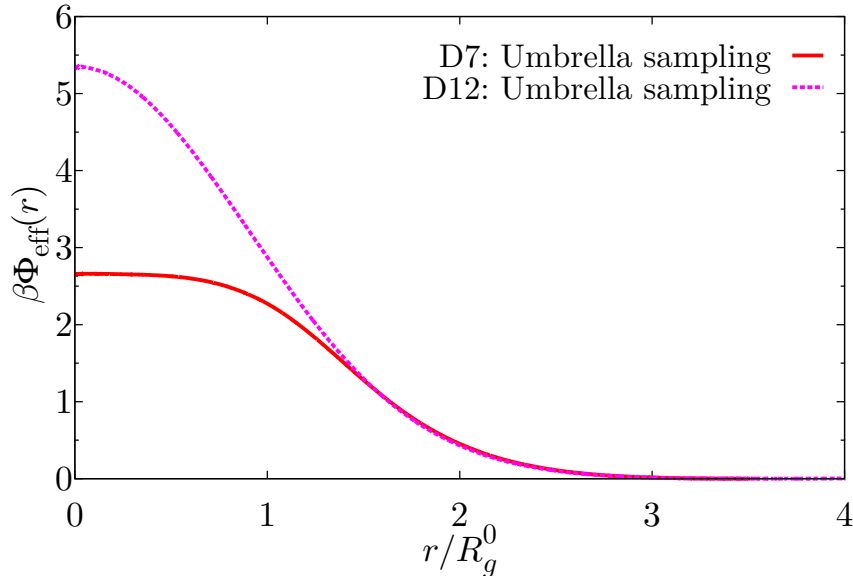

Figure 6.8: Comparison of the effective interactions obtained with the umbrella sampling method between $G2$ dendrimer of D7- and D12-types.

identical results for the case of D12 dendrimers. In Fig. 6.8 we compare the shapes of the pair-potentials for the different types of $G2$ obtained with the umbrella sampling method (see Fig. 6.8) where we observe that the flattened maximum found in the D7 is replaced by a Gaussian-like form in the D12.

The effective interaction of the $G2$ D12-type dendrimers can be fitted to members of the general exponential model of exponent n (GEM-n) potentials $\phi(r)$:

$$\phi(r) = \epsilon \exp\left(-(r/\sigma)^n\right). \tag{6.2}$$

The fitting parameters are presented in Table 6.2.

type	$\epsilon/k_\mathrm{B}T$	σ/R_g	n
D12	5.34	1.26	2.02

Table 6.2: Fit parameters for the pair effective interaction between $G2$ dendrimers of D12-type using a GEM-n type of interaction [see Eq. (6.2)].

The effective pair interaction for $G4$ dendrimers and of D7- and D12-type are sketched in Figs. 6.9 and 6.10 respectively. In this case, for the umbrella sampling the value at $r = 0$ increases and the pair-potential takes a Gaussian form with increasing the dendrimers generation from 2 to 4 and by changing the dendrimer type from D7 to D12. In Table 6.3 we present the fitting parameters and we also illustrate the relevant fitting curve in a common plot with the effective interaction extracted from the simulation data
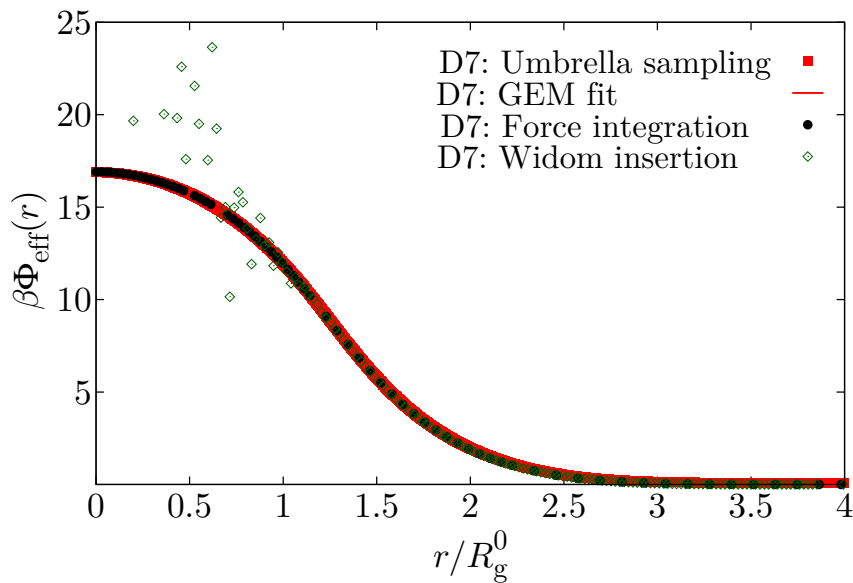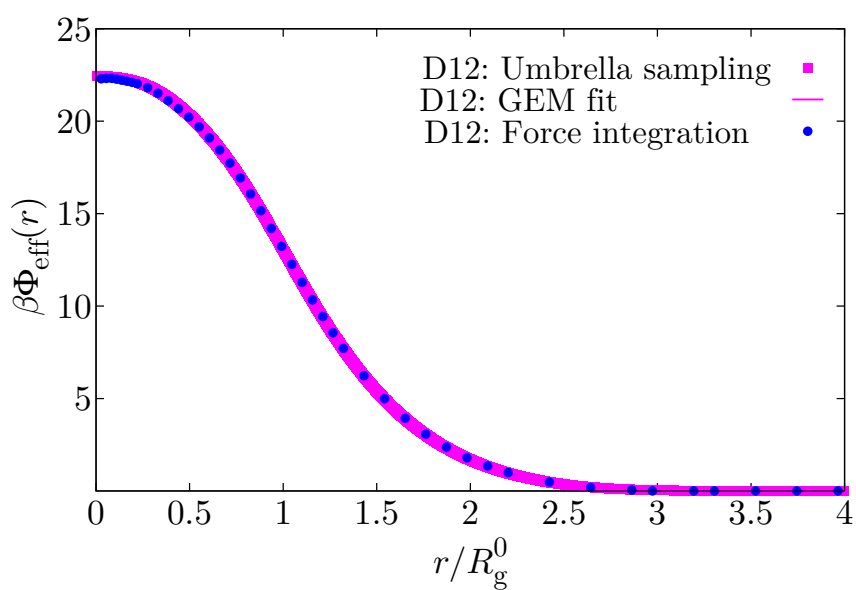
Figure 6.9: Comparison between the effective interaction between two G4 dendrimers of type D7 obtained with the umbrella sampling method (filled squares, GEM-n fit solid line), by integrating the Force from the fixed CM method (filled circles) and with the Widom method (empty diamonds).

in Figs. 6.9 and 6.10. Employing a description based on the validity of the effective pair-interaction being valid for all densities [130], these values of the exponents indicate that these types of amphiphilic dendrimers could form clusters [26, 130]. Upon increasing the

type	$\epsilon/k_{\mathrm{B}}T$	σ/R_{g}	n
D7	16.81	1.48	2.60
D12	22.56	1.29	2.31

Table 6.3: Fit parameters for the pair effective interaction of dendrimers of D7- and D12-type using a GEM-n type of interaction [see Eq. (6.2)].

dendrimer's generation from 2 to 4 the Widom method fails to give correct results at short distance separations. The discrepancies between this method and the other approaches for calculating the effective interaction suggest that the internal structure and also the shape of dendrimers change due to their mutual influence.

Figure 6.10: Comparison between the effective interaction between two G4 dendrimers of type D12 obtained with the umbrella sampling method (filled squares, GEM-n fit solid line) and by integrating the Force from the fixed CM method (filled circles).

6.2.2   Shape deformation

We focus now on the case of $G4$ dendrimers. The shape of the effective interaction (see Figs. 6.9 and 6.10) suggests that on approaching each other, the dendrimers of both types experience an overall repulsive force. The repulsion is enhanced as the dendrimers start to overlap since the core particles repel the shell particles. As soon as the core regions overlap the growth of the repulsion ceases to increase upon further compression. Although both dendrimer types show the same qualitative behavior on overlap, its nature is different for the D7- and the D12-type. In the case of D7 dendrimers it is the attractive core-core monomer interactions [see Fig. 3.10] that suspend the repulsion. On the other hand, in the case of D12 dendrimers, the repulsive nature of the cores results in a higher potential value at the origin but it also gives a more open structure to the dendrimers (see Sec. 6.1.2) and thus there is more free space available for the dendrimers to inter-penetrate each other. This can be seen also from the simulation snapshots presented in Fig. 6.11.

(a)   (b)
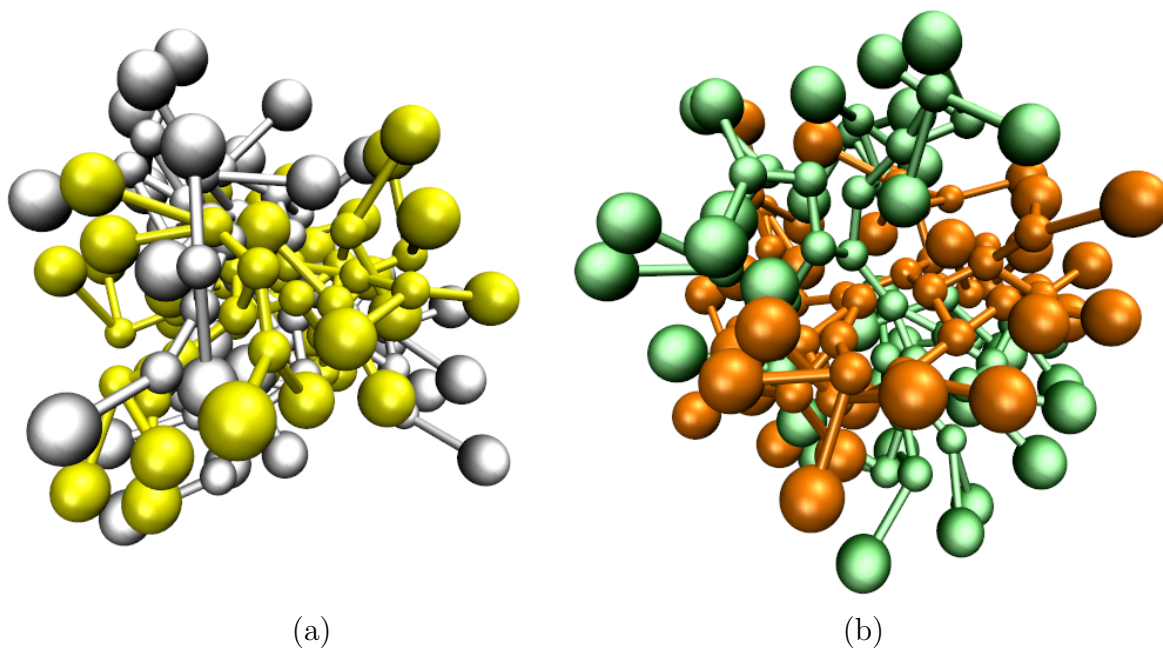
Figure 6.11: Simulation snapshot of two interacting $G4$ dendrimers at interdendrimer distance $r = 0$ and of (a) D7- and (b) D12-type dendrimers. Different colors mark different dendrimers. In the case of D7 dendrimers, the attractive nature of the core regions is responsible for the overlap of dendrimers. In the case of the D12 dendrimers, it is the open structure of the dendrimers that allows them to overlap.

In order to have a better understanding of the mutual change in the shape of the dendrimers, we sketch in a common plot the effective potential as well as the asphericity b and acylindricity c versus the interdendrimer separation r for the D7 (Fig. 6.12) and the D12 dendrimers (Fig. 6.13). The solid line in Figs. 6.12 and 6.13 shows the dimensionless

effective interaction potential, $\beta\Phi_{\mathrm{eff}}(r)$, of two $G = 4$ dendrimers in the zero-density limit computed using umbrella sampling (Sec. 2.4.3.1). The filled circle points correspond to the asphericity b while the empty circles to the acylindricity c. The acylindricity of dendrimers is essentially the same for both models and although it increases as the dendrimers are pushed against each other it remains small. Its deviation from the acylindricity of isolated dendrimers is moderate since the values of b and c at larger separations, i.e. $r \gtrsim 2.5R_{\mathrm{g}}$, coincide with those of an isolated dendrimer. On the other hand, the asphericity exhibits a much more pronounced dependence on distance, increasing from about 0.24 and 0.26 (in D12 and D7 types, respectively) at large separation to about 0.32 and 0.35 in overlapping dendrimers. As soon as the overlap of dendrimers becomes significant at a distance $r \simeq 2R_{\mathrm{g}}^0$, the interaction of the shell particles causes an increase in the asphericity.
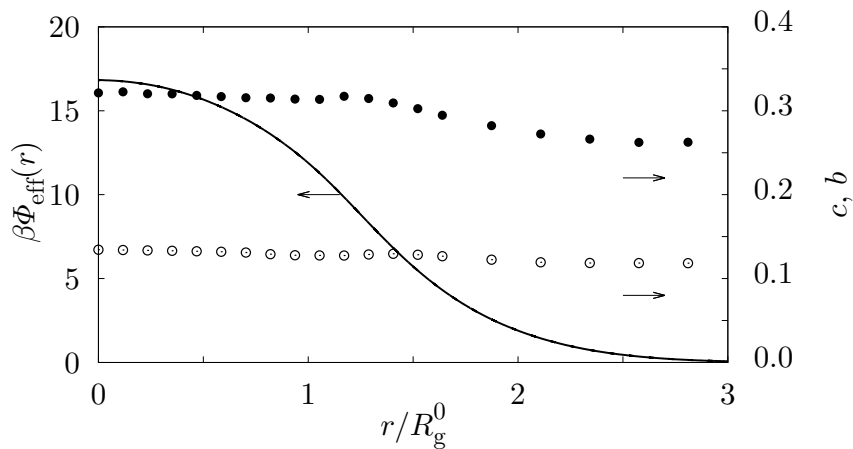
Figure 6.12: Dimensionless effective interaction $\beta\Phi_{\mathrm{eff}}(r)$ (solid line) between two D7 dendrimers of $G = 4$ and their asphericity b and acylindricity c (filled and open circles, respectively), both shown on the secondary vertical axis. The distances are scaled to the respective radius of gyration R_{g}^0 of the isolated dendrimer (see Table 6.1).
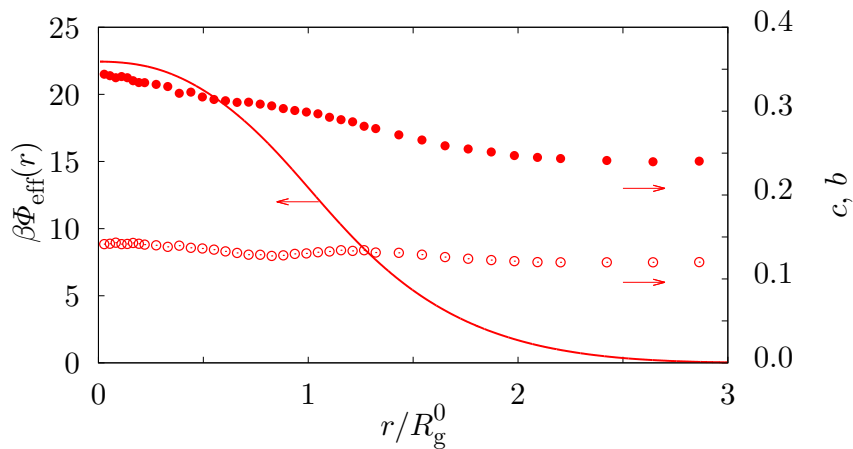
Figure 6.13: Same as Fig. 6.12 but for two interacting D12 dendrimers.

The distinctively different trends in asphericity for the two dendrimer models can also

be understood on a monomeric level. In the D12 model the mutual repulsion between all monomers at small center-to-center separations induces a steady increase in the asphericity with decreasing r, as this deformation enables dendrimers with suitable relative orientations (see Sec. 6.2.3) to minimize the number of interacting monomer pairs. In contrast, for the D7-dendrimers the attractive interactions between core monomers can lower the overall repulsion.

6.2.3   Relative orientation of dendrimers

It is clear that from the intrinsically aspherical shape of the dendrimers, which is even more enhanced by the presence of neighboring particles, it follows that the dendrimer-dendrimer interaction depends on both the relative orientation and the separation of the particles. In order to study the relative orientation of the dendrimers we use two different approaches, where we avoid using the full relative position and orientation of the dendrimers because it is too complicated and not very instructive. We restrict ourselves to the center of mass distance r, the angle ϕ_i ($i = 1$ and 2) between the long axis $\hat{\epsilon}_{1i}$ of the ith dendrimer and the unit center-to-center vector $\hat{r}$, the angle θ between the long axes of both dendrimers, which are depicted schematically in Fig. 6.14, and the quantity α defined in Eq. (5.41).
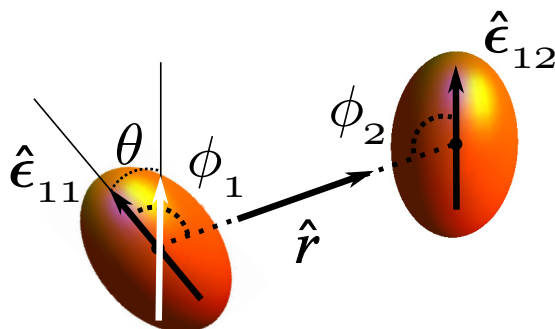
Figure 6.14: Schematic representation of the two unit vectors, $\hat{\epsilon}_{11}$ and $\hat{\epsilon}_{12}$, needed to describe the respective orientations of molecules which are here represented by axisymmetric ellipsoids. With the symbols ϕ_1 and ϕ_2 we denote the angles between $\hat{\epsilon}_{11}$ and $\hat{\epsilon}_{12}$ and the unit center-to-center vector $\hat{r}$ between molecules 1 and 2, respectively. With the symbol θ we denote the angle between the long axes $\hat{\epsilon}_{11}$ and $\hat{\epsilon}_{12}$.

First we computed the distribution $P(\phi_i)$ of the angle ϕ_i with $i = 1$ and 2. The results for the $P(\phi)$ were obtained by averaging the distributions over the different ϕ_i. The data presented in Figs. 6.15(a) and 6.15(b) we show the normalized probability per unit solid angle, $P(\phi)$, as a function of the polar angle ϕ relative to the long axis of the dendrimer, over a representative range of center-to-center separations r. Since the distribution is symmetric around $\pi/2$, we have plotted $P(\phi)$ for the interval $[\pi/2, \pi)$. In Fig. 6.15(c) the orientation correlation function given by Eq. (5.40) is also plotted.

Figures 6.15 (a) - (c) provide a good quantitative representation of the relative orientation of the dendrimers but they are difficult to visualize. This is why we relegate the
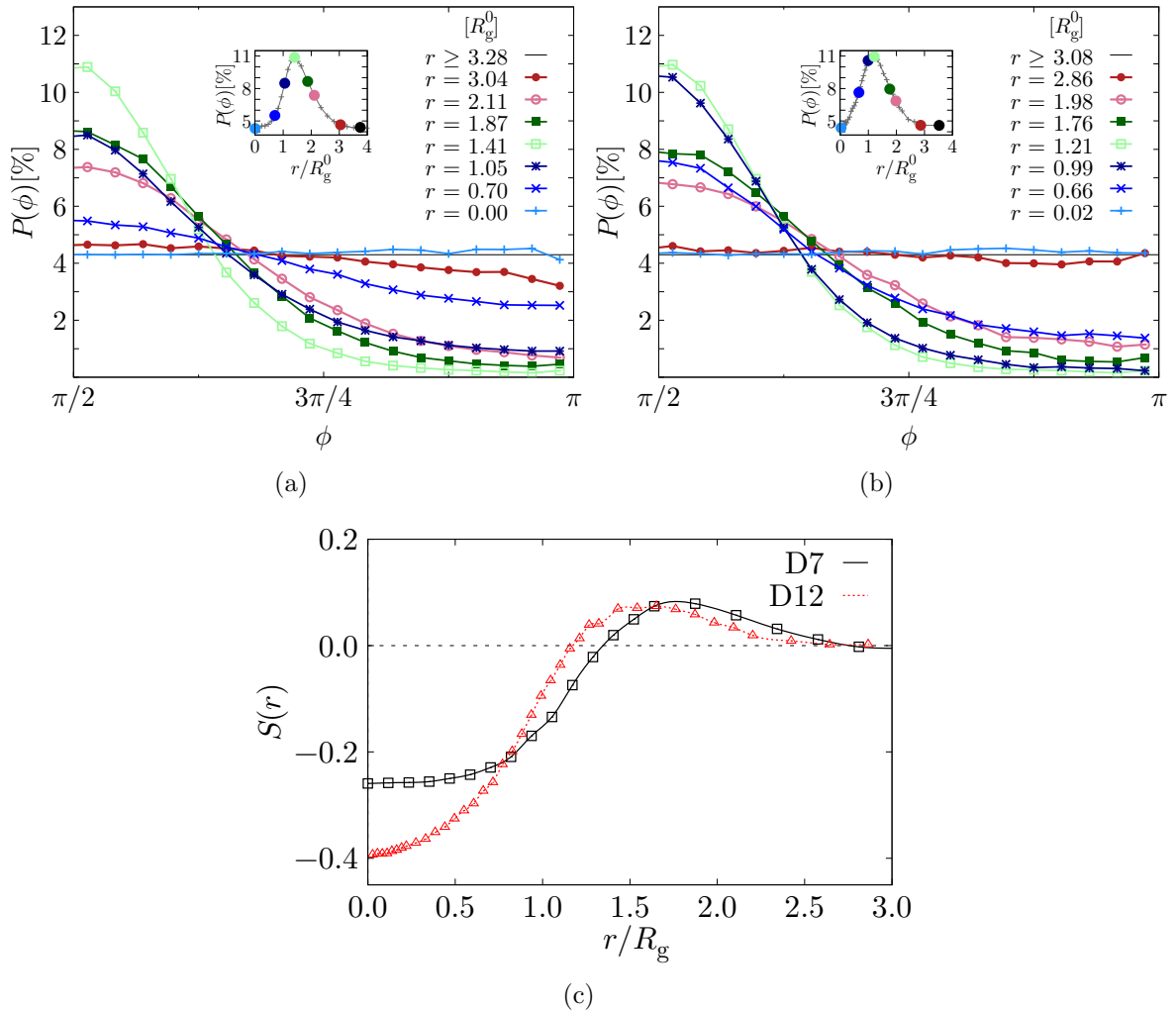
(a)

(b)

(c)

Figure 6.15: (a): normalized probability distribution per unit solid angle $P(\phi)$ for two interacting D7-dendrimers as a function of the polar angle ϕ over a representative range of separations r, expressed in units of R_{g}^{0}. The results are averages over both dendrimers. The inset shows the position of the maximum of $P(\phi)$ as a function of of the interdendrimer separation r. (b): same as Fig. 6.15(a) but for D12-type dendrimers. (c): orientational correlation function $S(r)$ [see Eq. (5.40)] as a function of the center-to-center separation r. The black square points correspond to the case of D7-type dendrimers while the red triangular points to the case of D12-type dendrimers.

interpretation to an alternative representation in Fig. 6.16 where we combined $P(\phi)$ for the different values of r in contour plots. The top panels of Figs. 6.16(a) and 6.16(b) show the normalized probability per unit solid angle, $P(\phi)$, as a function of ϕ, the polar angle relative to the long axis of the dendrimer and averaged over both angles ϕ_i, $i = 1$ and 2. In the bottom panels, the distribution of $S(r, \phi)$ is plotted, which measures the relative orientation by means of the quantity S defined in Eq. (5.40).
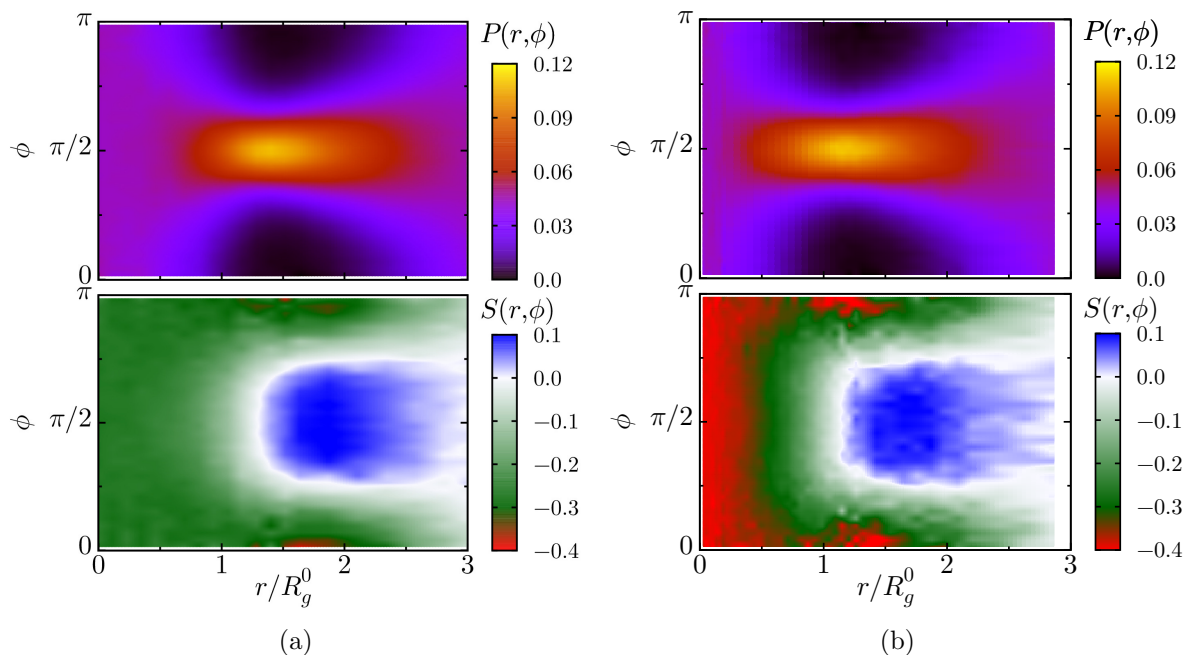
Figure 6.16: Contour plots for D7- (a) and D12-type (b) dendrimers. Top panels: probability $P(r, \phi)$ of finding the neighbor at a polar angle ϕ relative to the long axis connecting to the central dendrimer and a distance r; plotted is the probability distribution per unit solid angle. Bottom panels: distribution of the orientation correlation function $S(r, \phi)$ as defined in Eq. (5.40) for two interacting dendrimers as a function of separation r and polar angle ϕ.

At larger separations, i.e. at $r \gtrsim 3R_g^0$, the probability $P(r, \phi)$ obviously does not depend on ϕ and $S(r, \phi)$ becomes zero, which signifies random relative orientation [see Fig. 6.17(a)]. However, on approaching each other the two dendrimers are located preferentially in the equatorial position at $\phi = \pi/2$ whereas the polar regions, i.e. $\phi = 0$ and $\alpha = \pi$, are depopulated. This effect becomes most pronounced at a distances $r \approx 1.5R_g^0$ [see Fig. 6.17(b)]. At the same time, dendrimers in or near to the equatorial plane attain positive values for $S(r, \phi)$, indicating parallel orientations, whereas in the polar regions perpendicular relative orientations (negative $S(r, \phi)$-values) are preferred. In either case this allows the dendrimers to minimize mutual interactions by making the overlap region smaller.

At very small separations $r \lesssim 0.5R_g^0$ [see Fig. 6.17(c)] the probability distribution $P(r, \phi)$ becomes again uniform. This can be understood in view of the fact that in such cases the degree of overlap of dendrimers hardly depends on the position, but mainly on the relative orientation. In particular, the dendrimers prefer to have perpendicular orientations, which

(a)

$$r \gtrsim 3R_{\mathrm{g}}^0$$

(b)

$$r \approx 1.5 \text{ - } 2.5 R_{\mathrm{g}}^0$$
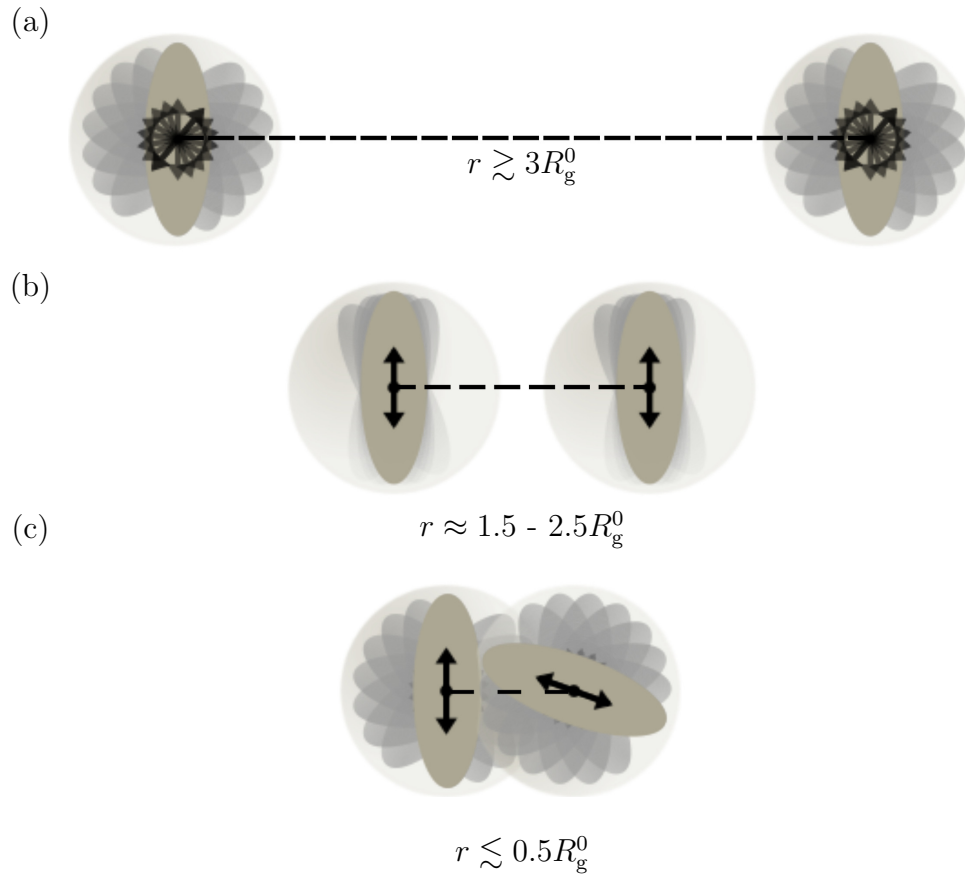
(c)

$$r \lesssim 0.5 R_{\mathrm{g}}^0$$

Figure 6.17: Schematic representation of the relative orientation of two dendrimers. (a) At large separations, the dendrimers do not interact with each other and thus $P(r, \phi)$ does not depend on ϕ. In this case $S(r, \phi) = 0$ and thus the dendrimers are randomly oriented. (b) At intermediate separations, they are located preferentially in the equatorial position with $S(r, \phi)$ attaining positive values. (c) At small separations, the dendrimers prefer to have almost perpendicular orientations ($S(r) < 0$) in order to minimize the interaction strength.

minimize the total degree of overlap, and hence the interaction strength, between the dendrimers.

The angle ϕ is in fact an average of the scalar products of the long axes and the center-to-center vector of both dendrimers. We choose to use the quantity α defined in Eq. (5.41), which we repeat here for convenience

$$\alpha = \frac{1}{2} \left[(\hat{\boldsymbol{\epsilon}}_{11} \cdot \hat{\mathbf{r}})^2 + (\hat{\boldsymbol{\epsilon}}_{12} \cdot \hat{\mathbf{r}})^2 \right], \tag{6.3}$$

as it contains two separate contributions of the angle ϕ. In Table 6.4 six characteristic pair configurations are listed along with the corresponding values of α and S as well as a schematic representation.
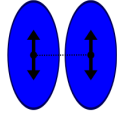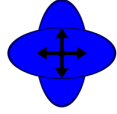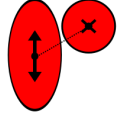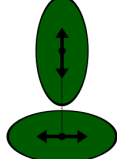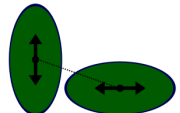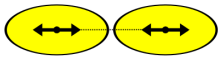
configuration	α	S	schematic
‖	0	1	
+	0	-0.5	
I˙	0.25	-0.5	
⊥	0.5	-0.5	
L	0.5	-0.5	
– –	1	1	

Table 6.4: List of symbols used for the six characteristic configurations along with the corresponding values of α and S. In the last column we sketch each pair configuration.
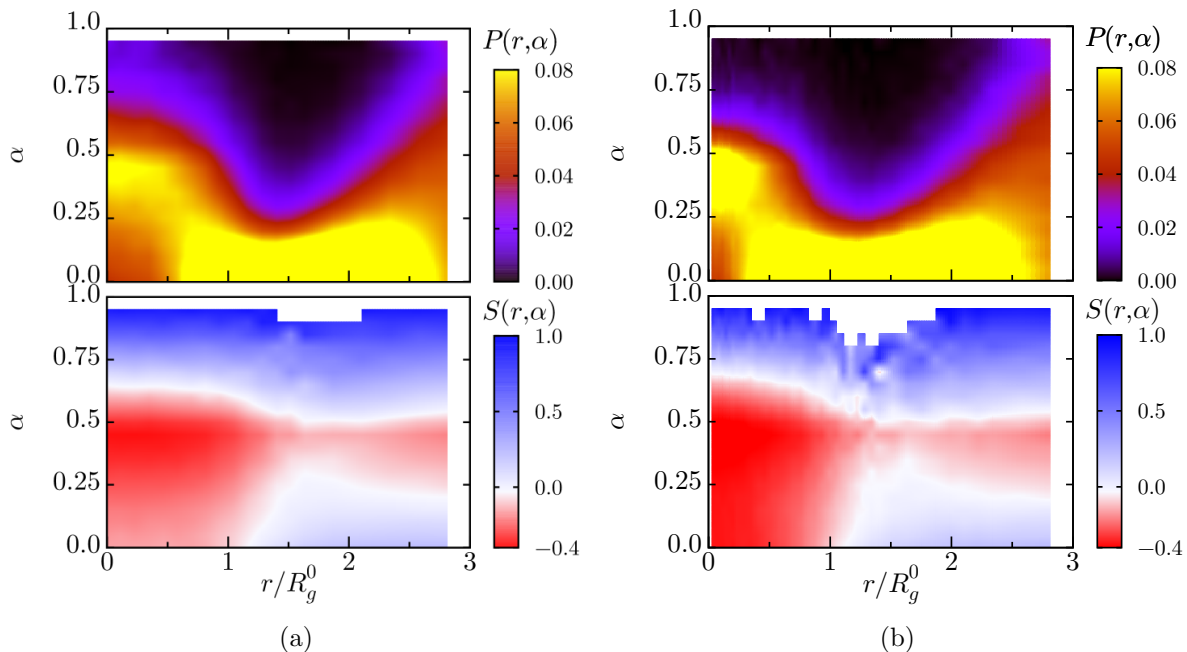
Figure 6.18: Positional and orientational order of an isolated pair of D7- (a) and D12-type (b) dendrimers. Top panels: the conditional probability $P(r, \alpha)$ of finding two dendrimers with a relative orientation which corresponds to a value α and a distance r. Bottom panels: distribution of the orientation correlation function $S(r, \alpha)$ as defined in Eq. (5.40) for two interacting dendrimers as a function of separation r and of the relative orientation parameter α.

In the top panels of Fig. 6.18 we observe the relative orientation of an isolated pair depends on their separation. It is not surprising that at large separation ($r/R_g^0 \gtrsim 3$) the dendrimers are completely uncorrelated since all the monomers belonging to different dendrimers are located above the Morse potential cutoff distance. In this regime, all orientations of $\hat{\epsilon}_1$ and $\hat{\epsilon}_2$, are equally probable and therefore we gain a flat profile of $P(r, \alpha)$ (not shown here). Correlations become more pronounced as the dendrimers approach each other.

At large separations, i.e. $r/R_g^0 \gtrsim 3$, we gain a flat profile of $P(r, \alpha)$ (not shown here) indicating that in this regime the orientations of the dendrimers are completely uncorrelated. This means that in the large separation regime all orientations of $\hat{\epsilon}_1$ and $\hat{\epsilon}_2$, are equally probable. On the onset of the interdendrimer interaction, i.e. $r \approx 2.5 R_g^0$, the correlations become more obvious. In more detail, on decreasing the center-of-mass distance r the conditional probability $P(r, \alpha)$ peaks at $r = 0$ and at $r/R_g^0 \approx 1.5$ the probability for configurations with $\alpha \gtrsim 0.25$ is essentially negligible. For $1.5 \lesssim r/R_g^0 \lesssim 2.5$ ∥ configuration are more preferred. This can be readily see in the bottom panels of Fig. 6.18 where the enhanced α range of $P(r, \alpha)$ coincides with the region of positive orientational order parameter $S(r, \alpha)$. In the regime of full overlap, i.e. $r/R_g^0 \lesssim 1$, the distribution $P(r, \alpha)$ broadens; orientations with $\alpha \approx 0.4$ are favored while the probability of large α ($\gtrsim 0.6$)-configurations is negligible. Combined with the strongly negative orientational order parameter $S(r, \alpha)$ at small r, this implies that ⊥ and ⌞ configurations are preferred

in the case of overlapping dendrimers. Thus we conclude that repulsion between the overlapping dendrimers forces them into a perpendicular arrangement (see also Fig. 6.11).

6.3   Dendrimer liquid

In this section, we investigate the positional and orientational properties of dendrimers in a bulk liquid. We employ standard NVT MC simulations to obtain the equilibrium structures of N_D number of dendrimers in a cubic simulation box. All the results presented here pertain to the case of $G = 4$, D7-type dendrimer.

As a measure for the density for the liquid phase, we introduce the volume fraction of the monomers, defined by [35]

$$\phi_m = \frac{N_\mathrm{D}}{V_\mathrm{system}} \frac{\pi}{6} \left(30 d_\mathrm{CC}^3 + 32 d_\mathrm{SS}^3\right), \tag{6.4}$$

where:

$$d_\mathrm{SS} = 1.50 d_\mathrm{CC}, \tag{6.5}$$

V_system is the volume of the system expressed in units of the core monomer diameter d_CC. Thus,

$$\phi_m \approx \frac{N_\mathrm{D}}{V_\mathrm{system}} \times 72.2565 \ d_\mathrm{CC}^3. \tag{6.6}$$

As we have seen in Fig. 6.12 the inter-dendrimer interactions affects the shape and the relative orientation of the dendrimers. However, we expect that the zero density pair interaction alone should not be sufficient for the description of the spatial and orientational behavior of a bulk system. With the use of standard NVT Monte Carlo simulations (see Sec. 2.2) we obtain the equilibrium structure of an ensemble of N_D dendrimers in a cubic box and at several monomer packing fractions ϕ_m. Starting from several independent initial configurations at high temperatures, we cool the system using a simulated annealing protocol [53, 131] to reach the desired temperature T such that $k_\mathrm{B}T$ is $1.4\epsilon_\mathrm{CC}$, ϵ_CC being the depth of the core-core attractive potential.

During the simulations, the positions of monomers are recorded and used to evaluate the following structural features:

(i) For each dendrimer in the ensemble we calculate the RGT $\mathcal{S}$ (see Sec. 5.3.2).

(ii) By diagonalizing $\mathcal{S}$ we obtain the eigenvalues E_1, E_2, E_3 for each dendrimer. Using these values, the radius of gyration R_g, the asphericity b and the acylindricity c are computed using Eqs. (5.33), (5.36) and (5.37) respectively. We also record the normalized effective ellipsoidal volume V_ell given by [111]

$$V_\mathrm{ell} = 4\pi\sqrt{3}\sqrt{E_1 E_2 E_3} \tag{6.7}$$

which we normalize with the average effective volume of the isolated dendrimer V_ell^0.

(iii) Using the eigenvectors $\hat{\boldsymbol{\epsilon}}_1$ that correspond to the largest eigenvalues E_1 and center-to-center unit vector $\hat{\mathbf{r}}$, we compute for each pair of dendrimers in the ensemble the quantities α and S as in Sec. 6.2.3 (see Fig. 6.20). We refer to $\hat{\boldsymbol{\epsilon}}_1$ as the long axis of the dendrimer.

(iv) For the different volume fractions ϕ_m considered, we compute the conditional probability $P(r, \alpha)$ and the orientational order parameter $S(r, \alpha)$ in the following way: initially the r-space is divided in N_r^{bin} number of bins each one of length equal to the core monomer diameter d_{CC}. On each r-bin separate statistics for the parameter α are performed; we create an one-dimensional histogram of the parameter α for each r-bin by dividing the α-space into 40 equally sized bins (the number of bins is arbitrary). This way we get one one-dimensional histogram of α for each value of r. We normalize the α-histogram according to the total number of pairs and to the random distribution of the α parameter (cf. Appendix A). This way, we obtain the normalized conditional distribution $P(r, \alpha)$. Similarly, we construct the $S(r, \alpha)$ conditional distributions where on each α bin instead of counting pairs, we weight the histogram according to the S value of the pair of dendrimers.

(v) Last, we calculate the pair distribution function $g(r)$ as a function of interdendrimer separation r and the two-dimensional radial distribution function $g(r; \alpha)$ described in the following. The distribution $g(r; \alpha)$ can be constructed in a way similar to the $g(r)$. Instead of an one-dimensional histogram, where only the r-space is divided into bins, we create a two-dimensional histogram where additionally to the r-binning we also divide the orientational parameter α-space, creating pairs (r, α). After counting the dendrimer pairs that fall into each (r, α)-bin, the histogram is normalized with the volume element of each r-bin (see Sec. 5.1) as well as with the random distribution of α (see (iv)).
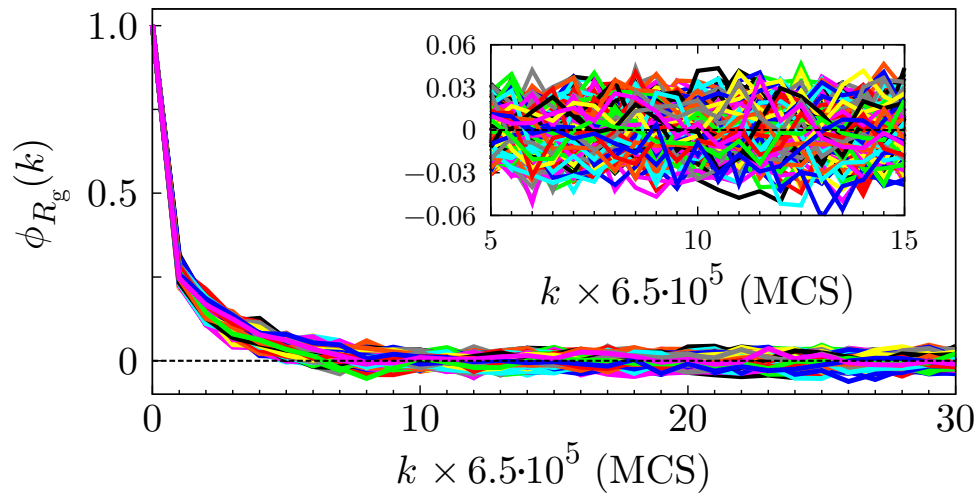

Figure 6.19: The first 30 lags (k) of the autocorrelation function $\phi_{R_g}(k)$ of 220 individual D7 dendrimers of generation $G = 4$ at a density $\phi_m = 0.249$. Different colors correspond to different dendrimers within the same simulation run.

Similarly to the case of the isolated dendrimer (see Sec. 6.1.1), we determine the optimal sampling frequency by checking the behavior of the autocorrelation function of R_g Eq. (5.22). A typical example of the correlation function $\phi_{R_g}(k)$ measured for individual dendrimers in a system of 220 D7 dendrimers of generation $G = 4$ and volume monomer fraction $\phi_m = 0.248$ is shown in Fig. 6.19. The results for different dendrimers

within the same simulation coincide almost perfectly and to a good approximation, the autocorrelation function decays exponentially. The simulation runs typically involve 5×10^5 to 3×10^6 equilibration sweeps followed by 5×10^7 to 5×10^8 production sweeps with a sampling frequency between 2×10^4 and $\times 10^6$ sweeps depending on the number of dendrimers N_D in the system as well as on the monomer volume fraction ϕ_m.
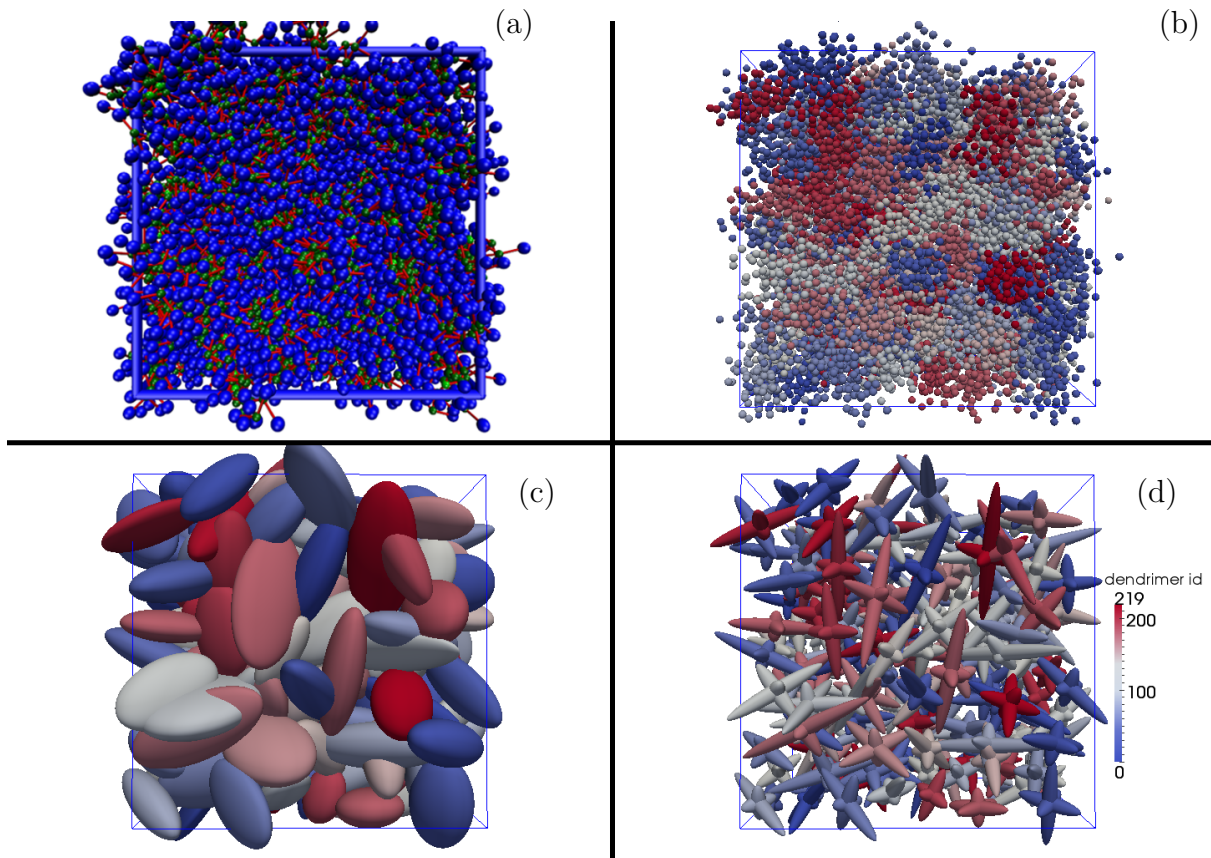

Figure 6.20: Snapshot of a configuration of 220 interacting D7 dendrimers of fourth generation at a volume fraction $\phi_m = 0.199$. Panel (a): representation of the dendrimers by their monomeric units and by their bonds. Core monomers are colored are green, shell monomers are blue and bonds are red. Monomers are drawn to scale. In panels (b),(c) and (d) each dendrimer is represented by a different color according to the legend in panel (d). Panel (b): representation of the dendrimers by their monomeric units (not to scale). Panel (c): dendrimers represented by ellipsoids of semiaxes equal to the eigenvalues of the radius of gyration tensor, E_1, E_2, and E_3. Panel (d): dendrimer represented by the semiaxes of the radius of gyration tensor.

In order to determine the appropriate system size, we simulate different numbers of dendrimers N_D from $N_D = 27$ with 1674 monomers up to $N_D = 220$ with 13640 monomers and at densities covering a range from $\phi_m = 0.030$ to $\phi_m = 0.249$. In Fig. 6.21 we plot the average asphericity b, acylindricity c and the normalized ellipsoidal volume V_{ell}/V_{ell}^0 [see Eq. (6.7)] as a function of the overall density ϕ_m for the different system sizes. The data obtained by these simulations suggest that, as far as shape deformations are con-

cerned, there are no finite-size effects in any of the quantities of interest. For clarity we also plot in Fig. 6.22 the pair distribution function $g(r)$ as a function of the interdendrimer separation r for the largest monomer volume fraction studied, i.e. $\phi_m \approx 0.248$, and for system sizes from $N_D = 27$ up to 220. We observe that the smaller systems are not able to capture the long-range behavior where $g(r) \to 1$. In an effort to minimize
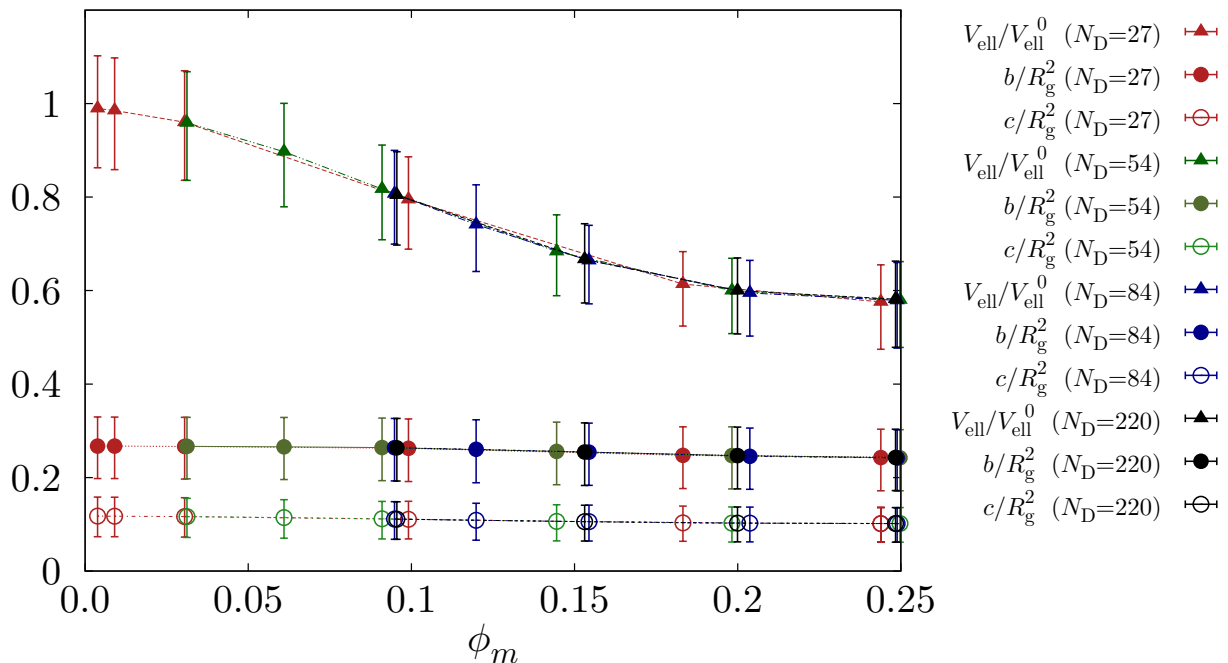

Figure 6.21: Mean asphericity (b), acylindricity (c), and normalized ellipsoidal volume (V_{ell}/V_{ell}^0) in a fluid of interacting D7 fourth generation dendrimers as functions of the monomer volume fraction ϕ_m [see Eq. (6.4)] and for several system sizes N. The error bars indicate the first and the third quartile of the respective distributions.

computational time, we first limited our investigation to the case of 27 dendrimers in the liquid phase where we computed the relative orientations using the quantity α as presented in Sec. 6.3 (iii). After developing the necessary tools we apply them to all system sizes. Nevertheless, all system sizes studied exhibited the same quantitative and qualitative behavior. Therefore, we choose to present in Sec. 6.3.1 the results from simulations of the largest system studied, i.e. a system of $N_D = 220$ dendrimers.
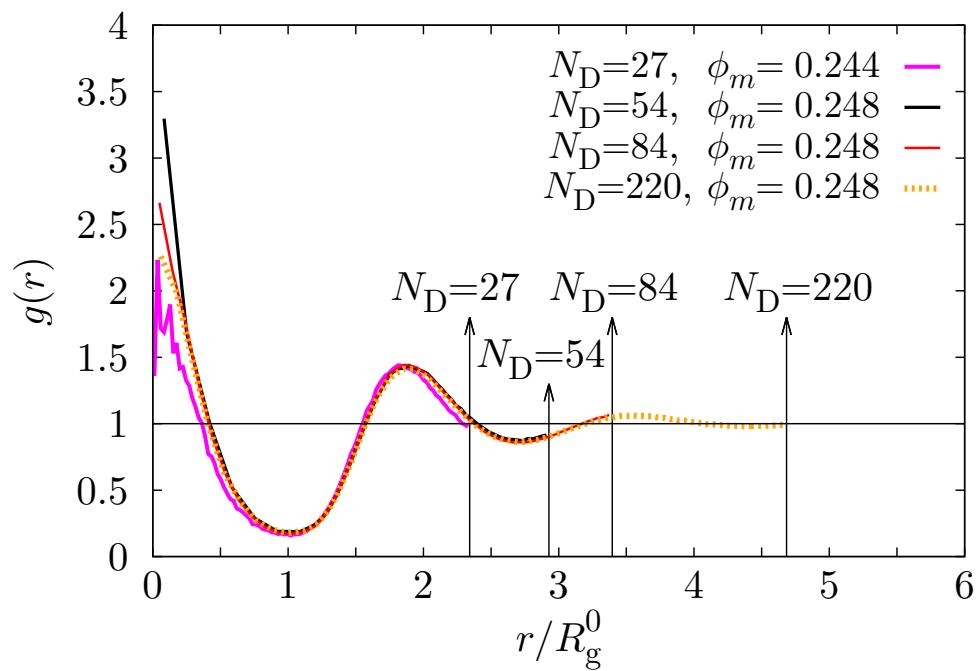
Figure 6.22: Pair distribution function $g(r)$ as a function of the interdendrimer separation r for systems of different number of dendrimers N_{D}. The arrows indicate the location of the half box size for each system size.

6.3.1   System of $N_{\mathrm{D}} = 220$ dendrimers in the liquid phase

In this section, the discussion will point to the case of 220 dendrimers of D7-type in the liquid phase at volume fractions covering a range from $\phi_m = 0.0$ to 0.248. At the largest volume fraction ($\phi_m = 0.248$) we perform 1000 different realization where in each one we sample for 6.5×10^6 MC sweeps after equilibration. During the simulation runs we recorded the positions of the monomers with a sampling frequency of 6.5×10^5 MC sweeps determined by the autocorrelation plot shown in Fig. 6.19. For smaller densities we perform from 20 (for $\phi_m = 0.095$) to 500 (for $\phi_m = 0.199$) different realizations and sampled the system for 5×10^6 MC sweeps.
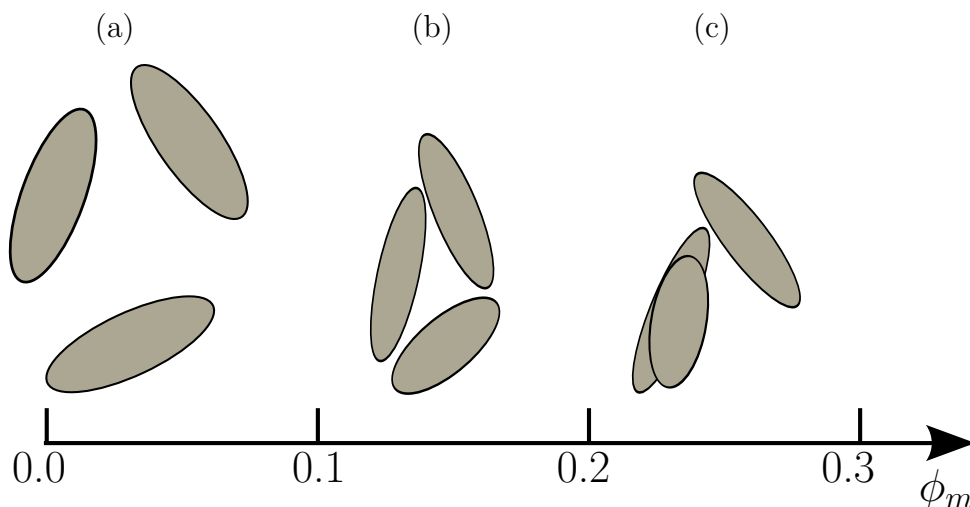

Figure 6.23: Schematic representation of the compression of dendrimer volume. (a) At volume fractions $\phi_m \approx 0$ the dendrimers do not interact with each other and as a result the ellipsoidal volume of each individual dendrimer is the same with that of the isolated dendrimers. (b) For volume fractions in the range $\phi_m = 0.0$ to $\phi_m \approx 0.19$ the dendrimers experience a massive compression but their shape remains the same in terms of asphericity b and acylindricity c. In this range the dendrimers do not overlap (see Fig. 6.24). (c) Upon further increasing ϕ_m, the rate of compression decreases as the dendrimers start to overlap. Multi-occupancy of dendrimers starts playing a significant role in lowering the energy of the system. The compression of dendrimers seems to stop at $\phi_m \approx 0.24$ where the mean volume of the dendrimers correspond to 60% of that of an isolated dendrimer.

The results presented in Fig. 6.21 demonstrate the pronounced impact of many-body effects. Based on the results obtained for a pair of dendrimers –where the asphericity is increasing with decreasing the interdendrimer separation (cf. Figs. 6.12 and 6.13) – we expected that the interacting macromolecules would become more and more elongated as the volume fraction is increased. However, the results displayed in Fig. 6.21 show that there is no significant change in the average asphericity and acylindricity with the volume fraction. In fact, there is a slight decrease in both of the aforementioned quantities with increasing the volume fraction.

In contrast, the size of the dendrimers is affected considerably. In particular, at the highest volume fraction investigated, $\phi_m = 0.248$, the volume that a dendrimer occupies, based on Eq. (6.7), corresponds to only 60% of that when such a dendrimer is considered

isolated. This massive compression is much larger than that found by Götze et al. [21], where for dendrimers with hard-core monomers a value of $R_g/R_g^0 \approx 0.98$ was reported for highly concentrated dendrimer solutions. The large deformation found here implies that the effective pair interactions calculated at the zero-density limit (see Fig. 6.9) will fail to accurately describe dense systems.

As we can see in Fig. 6.21 the reduction in volume of the dendrimers seems to stop at $\phi_m \simeq 0.24$. At this volume fraction, the system has found an alternative way to lower its energy (see Fig. 6.23).

Whereas for $\phi_m \lesssim 0.199$ the value of the radial distribution function $g(r = 0)$, shown in Fig. 6.24, vanishes or is very small, it increases beyond this threshold. For $\phi_m \geq 0.248$, the probability of finding a dendrimer overlapping with the reference dendrimer is larger than the probability of finding it in the nearest-neighbor shell. Consequently, the system arrives at a transition from a normal dense liquid to a multi-occupancy or cluster liquid.
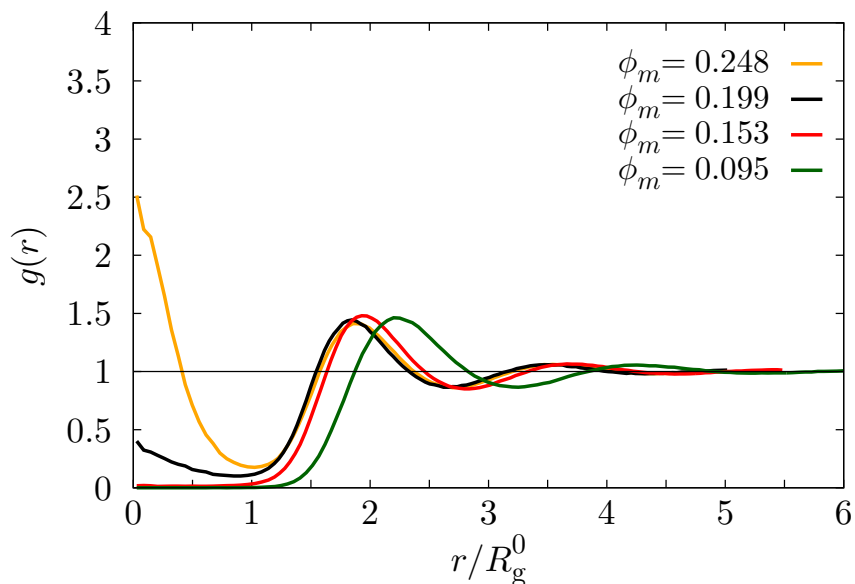

Figure 6.24: Radial distribution function $g(r)$ as a function of r for a system of 220 dendrimers and for monomer volume fractions ϕ_m covering a range from 0.095 to 0.248.

Considering Fig. 6.21 we point the reduction in volume as an effect stemming from the many-body interactions, since such a feature was not present in the results for two dendrimers in the zero-density limit. Therefore, we focus now our attention on computing the positional and orientational correlations in the fluid state. These calculations are performed in the same way as we have presented for a pair of interacting dendrimers (see Sec. 6.2.3). We use once again the orientation parameter α and the orientational correlation function $S(r, \alpha)$.

In Fig. 6.27 we compare the results obtained for two different volume fractions of $\phi_m = 0.199$ and $\phi_m = 0.248$, and with the results for a pair of dendrimers. In Fig. 6.27(a) we repeat as a reference the results for the two dendrimers in the zero-density limit [see Fig. 6.18(a)]. Additionally in Figs. 6.27(b) and 6.27(c) we plot the radial distribution function $g(r)$ (top panels), the conditional distribution function $P(r, \alpha)$ (middle panels) and the orientational order parameter $S(r, \alpha)$ (bottom panels).

As a first observation we note that the variations of $P(r, \alpha)$ are less noticeable compared to the isolated pair of dendrimers case. At distances $r/R_g^0 \approx 2.5$, the onset of the dendrimer-dendrimer interaction, we find a slight preference for large-α configurations (e.g., − −) [see Fig. 6.28(b)] which is also the case for overlapping dendrimers ($r \to 0$). In contrast to the aforementioned distances, at intermediate distances $r/R_g^0 \approx 1.5$ the large α configurations are less preferred – similar to the two isolated dendrimers – whereas the $\alpha < 0.25$ configurations are more favored [see Figs. 6.28(d) and 6.28(e)].

To give a more accurate description for the location and orientation of nearest neighbours we superimpose in the $P(r, \alpha)$- and $S(r, \alpha)$-plots some of the contour lines of the $g(r; \alpha)$. At the smaller packing fraction this contour line corresponds to the surface representing the nearest neighbor peak location; the value of the $g(r; \alpha)$ on the isoline is a little smaller than the height of this peak. At the larger packing fraction, $\phi_m = 0.248$, we additionally plot the contour line at the overlapping region $r \to 0$. This representation is more clear than that of plotting the whole set of isolines (see Fig. 6.3.1) and yet more robust than displaying only the r-location of the nearest-neighbor peak using the pair distribution function $g(r)$.
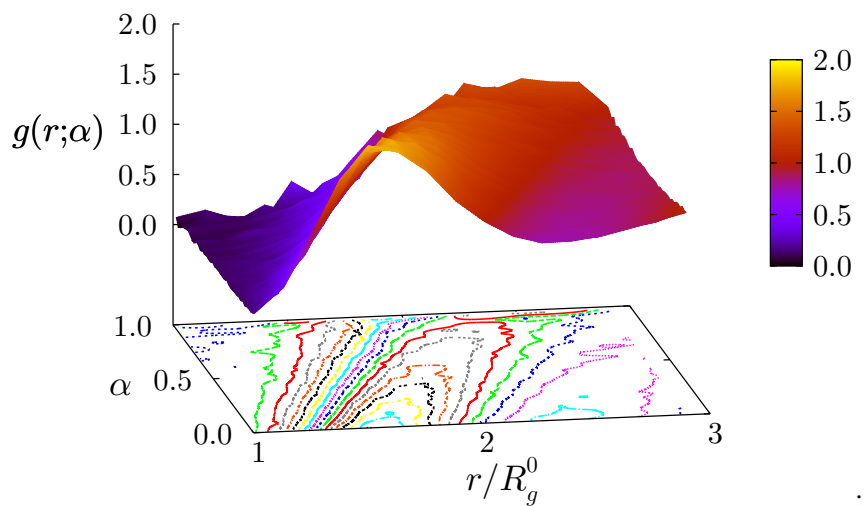

Figure 6.25: Surface and contour lines of $g(r, \alpha)$ for a system of $N_D = 220$ dendrimers in the liquid phase and at a volume fraction $\phi_m = 0.199$.

Based on the tilted $g(r)$ contour line, the nearest $\alpha = 0$ neighbors peak at the smaller packing fraction $\phi_m = 0.199$ is located at a distance $r \approx 1.7 R_g$. The value of $\alpha = 0$, along with the observation of a positive value of $S(r, \alpha)$ [bottom panel in Fig. 6.27(b)] lead to the conclusion of a parallel ‖ configuration rather than a + configuration (see Table 6.4). The intermediate-α configurations (⌐ ˙, ⊥, and ⌐) are located at a distance of about $2R_g^0$. Last, end-to-end − − configuration with $\alpha = 1$ are located at $r \approx 2.25 R_g^0$.

The differences of the relative orientation of a pair of dendrimers in isolation and in a bulk liquid at both small and large separations are even more pronounced at the larger packing fraction $\phi_m = 0.248$ [Fig. 6.27(c)] where particles start to overlap. Additionally to the nearest neighbor peak, which exhibits similar behavior to the one at smaller volume fraction, the occurrence of isolines at small r-values indicate the overlapping of dendrimers. In this overlapping region we find a preferred parallel orientation due to the peak of the
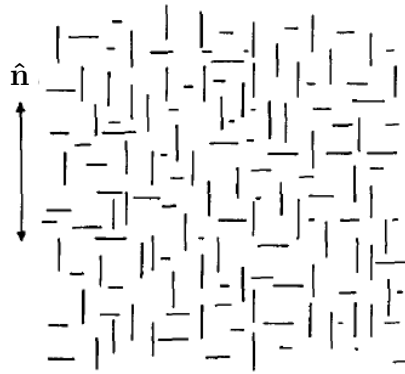
Figure 6.26: A schematic view of the antinematic from Ref. [39]. For monoaxial molecules interacting via a Corner-type potential [132] it was found that the distribution function describing the orientation of molecules with respect to the director $\hat{\mathbf{n}}$ has two maxima. The first maximum corresponded to orientations of the molecules parallel to the director $\hat{\mathbf{n}}$ whereas the second to the antinematic phase where the orientations of the molecules are perpendicular to the director.

conditional distribution function $P(r, \alpha)$ at $\alpha = 0$ [middle panel of Fig. 6.27(c)].

To visualize the resulting orientation pattern of dendrimers in the liquid phase, we show in Fig. 6.28 an idealized schematic view, where dendrimers are represented by axisymmetric ellipsoids of aspect ratio of 1.70, consistent with the average ratio of semiaxes of a single isolated dendrimer (Table 6.1). Figure 6.28(a) shows the observed pattern in a dendrimer liquid. In more detail, the polar regions of the central reference dendrimer (colored in white) are populated either by ━━ neighbors (yellow) or by ⊥ neighbors (green) [see Figs. 6.28(b) and 6.28(c), respectively]. In the equatorial plane, the central reference dendrimer is surrounded by ‖(blue), ╎˙ (red), and ⊥ (green) neighbors [see Figs. 6.28(d), 6.28(e) and 6.28(f), respectively], with the ‖ neighbors being located a little closer to the reference particle than the ╎˙ and the ⊥ neighbors. Since most nearest neighbors are perpendicular the resulting pattern is *antinematic* [39] (see Fig. 6.26) such that the long axes of most nearest neighbors are perpendicular, e.g., ╎━˙╎˙╎━ (where dots represent rods pointing into or out of the paper).

The bottom Fig. 6.27(a) shows the perpendicular arrangement (✚) of a pair of isolated dendrimers in the overlapping region ($r \to 0$), which can be see from the extended red region. On the contrary, overlapping dendrimers are arranged in an end-to-end configuration in a bulk liquid of volume fraction $\phi_m = 0.248$ [see bottom panel of Fig. 6.27(c)]. The origin of such a strong effect stems from tight ordering where the neighbors form a "cage" which leaves little space for a perpendicular orientation of overlapping dendrimers. Together with the differences of $P(r, \alpha)$ between an isolated pair [top panel of figure Fig. 6.27(a)] and a pair in a bulk dendrimer liquid (middle panels of Fig. 6.27(b) and Fig. 6.27(c)) signify the existence of many-body effects.
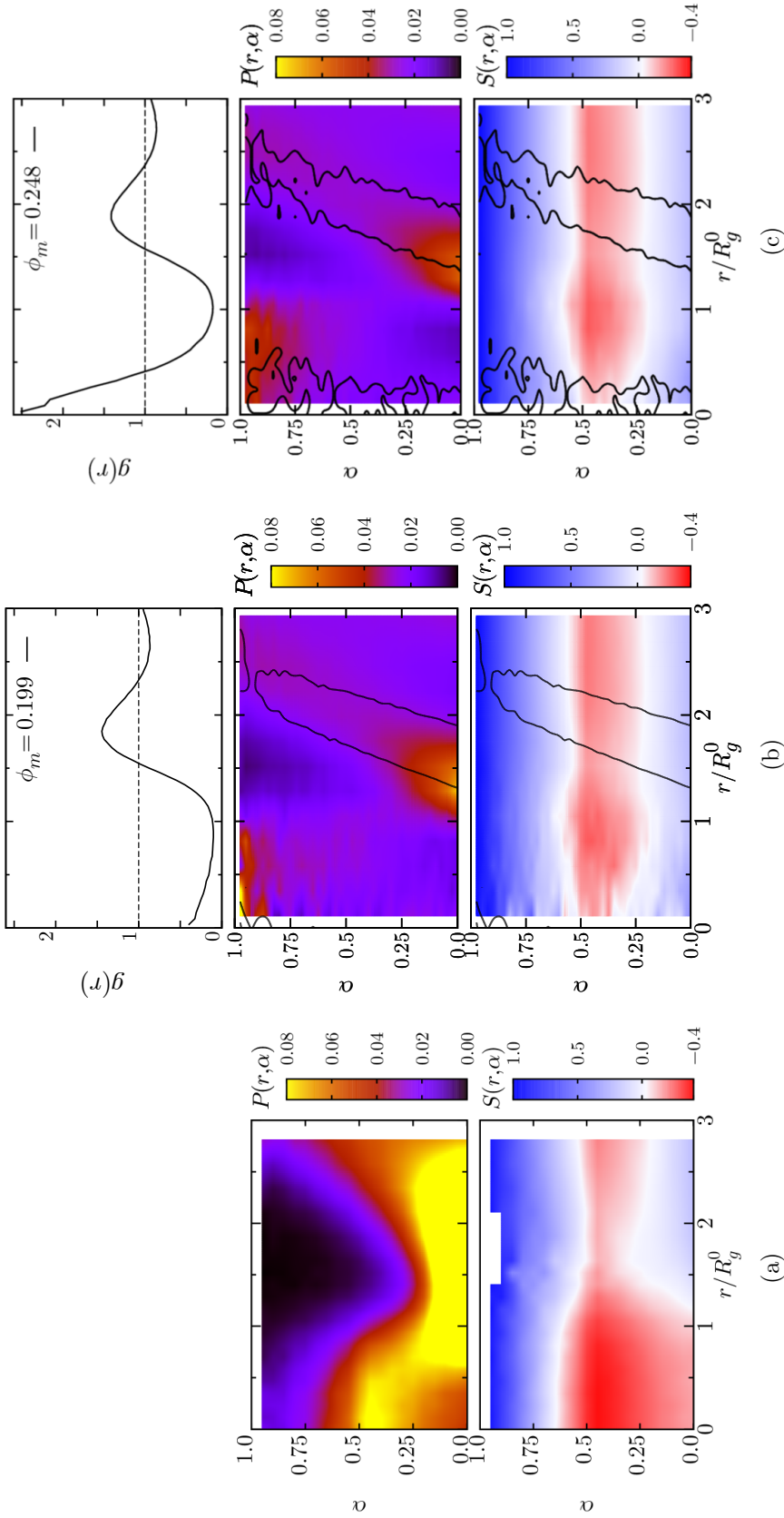
Figure 6.27: Positional and orientational order of two interacting dendrimers. (a): shows the data for the isolated pair [see Fig. 6.27(a)]. Top panel presents the conditional probability $P(r, \alpha)$ whereas the bottom panel the orientational order parameter $S(r, \alpha)$. (b), (c) show the data for each pair of dendrimers in the liquid state at packing fractions $\phi_m = 0.199$ and $\phi_m = 0.248$ respectively. Top panels: Radial distribution function $g(r)$ as a function of r. Middle panels: density plot of the conditional probability $P(r, \alpha)$. Bottom panels: density plot of the orientational order parameter S. Black contours are isolines of the pair distribution function $g(r; \alpha)$ at a value a little smaller than the height of the nearest-neighbor peak.
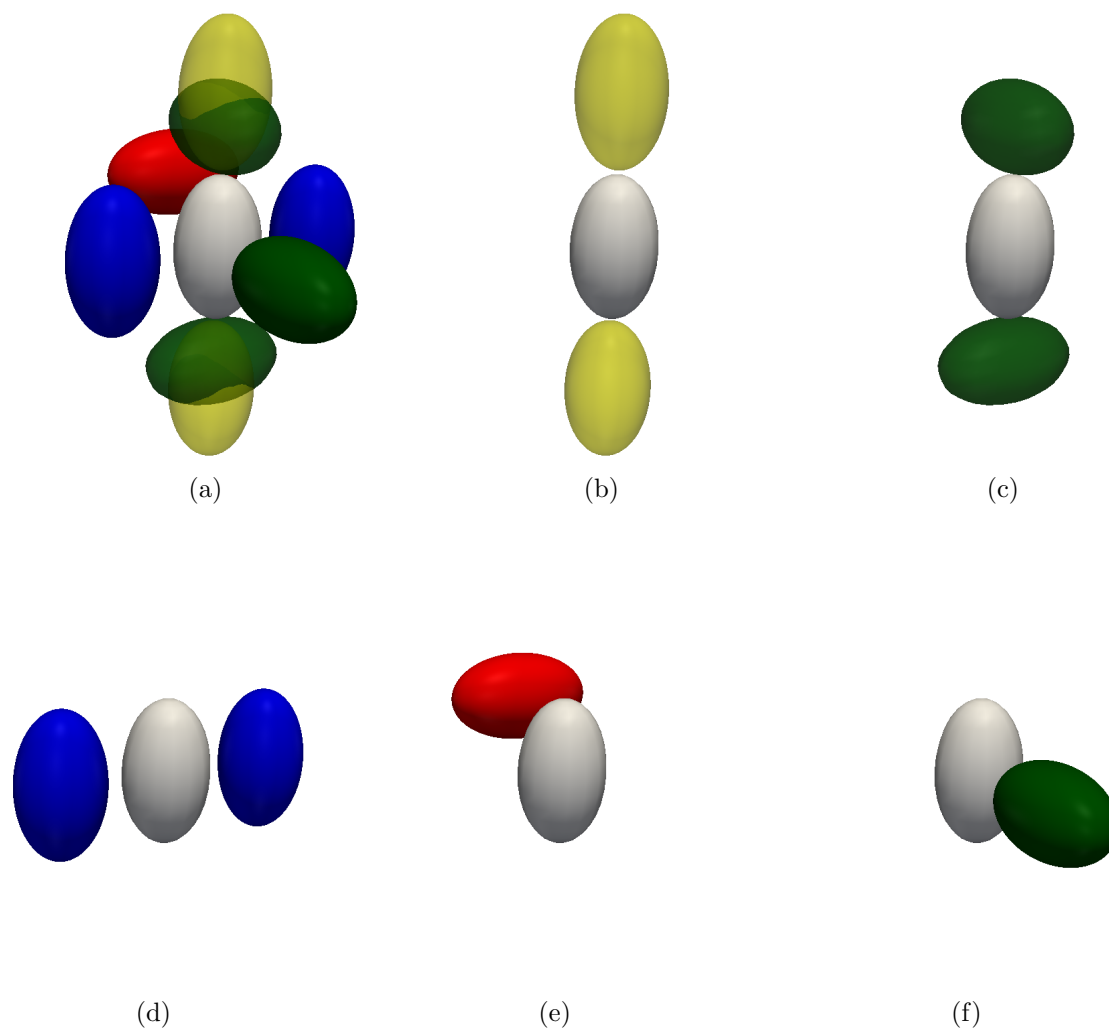
Figure 6.28: Schematic representation of the antinematic packing pattern observed in a dendrimer liquid. (a): The central reference dendrimer, drawned in white, is surrounded by neighbors with different orientations. The polar regions are populated either by ▬ ▬ (b) or by ⊥ (c) neighbors. In the equatorial plane, the central reference dendrimer is surrounded by ∥ (d), │˙ (e) and ⊥ (f) neighbors. The color coding is compatible with Table 6.4.

Chapter 7

Conclusions & Outlook

In this work we have studied the shape as well as the spatial and orientational equilibrium properties of amphiphilic dendrimers by means of extensive Monte Carlo simulations. Our investigations included the cases of an isolated dendrimer, a pair of interacting dendrimers in the zero-density limit as well as the case of a finite number of dendrimers in the bulk liquid phase. In the case a single isolated dendrimer, we investigated the shape properties vary with the generation number G ranging from $G = 2$ up to 10. We have shown that dendrimers are in general not spherical but prolate; their asphericity b, acylindricity c as well as the asphericity δ as defined by Rudnick and Gaspari [119] decrease monotonically with G. We also showed that the sizes of the amphiphilic dendrimers scale as $R_{\mathrm{g}} \sim N^{0.32}$ where N is the total number of monomers. This suggests that our model macromolecules exhibit a homogeneous structure where monomers are densely packed. To get a better understanding of the internal structure of our macromolecules we computed the density profiles for different values of G as well as for different monomer interaction potential parameters (cf. D7- and D12-type model in Sec. 3.2.3.2); our findings suggest that for generation up to $G = 4$ dendrimers have a segregated core-shell structure whereas for $G \geq 5$ back-folding of the shell monomers takes place. Then we focused on the case of $G4$ dendrimers and study the mutual influence in the shape of a pair of dendrimers in the zero-density limit and try to associate it to core and the shell monomers separately.

While studying our macromolecules in the zero-density limit we also investigated the effective interactions using several different approaches. We observed that up to generation $G = 4$ can be well fitted to members of the general exponential model of exponent n (GEM-n). It would be interesting as future work to investigate dendrimers of higher generations at the zero density limit and verify if they belong to the class of $Q^{\pm}$-potential that are prone to cluster formation [26, 130]. In Appendix B we show first results that also generation $G = 6$ dendrimers belong to the class of the aforementioned potentials. The most interesting case should be the one of $G = 10$ where the shell monomers fold back to the interior of the dendrimer and thus their structure loses its segregated core-shell character. Concerning the simulation methods for obtaining the effective interactions: from the three different methods that were presented in this thesis, the umbrella sampling method was proven to be the most robust and trustworthy technique for obtaining the pair effective interaction in the zero-density limit. The main disadvantage of this method is that separate simulations have to be performed in different windows of the inter-dendrimer separations r which, at the end of the simulations, have to be combined (see Appendix B). Other methods that can be used for obtaining the effective interactions of macromolecules

are:

(i) The Multiscale coarse-graining Method of Izvekov and Voth [133]; we show some preliminary results of the method in Appendix B.

(ii) The Virtual-Move Parallel Tempering (VMPT) method developed by Coluzza and Frenkel [134] combined with the waste-recycling method [50, 72].

In terms of shape deformations of two dendrimers in the zero-density limit, our results suggested that for $G = 4$ there is indeed a change in the shape and relative orientation of dendrimers due to their mutual influence. The data yielded by our study provide convincing evidence that our macromolecules become more prolate and that orientation plays an important role in the formation of clusters; this was attributed to the different nature of the core and the shell monomers. Amphiphilicity has the key role on both orientation and interpenetration of dendrimers. In the case of the D7 model, the attractive core-core interaction ceases the repulsion between the shell regions and along with the orientation of the molecules allows the formation of a cluster. On the other hard, if the core-core interaction is repulsive the perpendicular relative orientation of the molecules preferred axes of elongation can by itself allow the interpenetration of dendrimers.

Finally, we investigated the spatial and orientational properties of dendrimers in a bulk liquid. We first performed extensive Monte Carlo simulations for several system sizes starting from a system of 27 dendrimers with 1674 monomers end ending at a total number of 220 dendrimers with 13640 monomers. For all the aforementioned systems we calculated the shape in terms of asphericity b and acylindricity c as well as the size using as a measure the volume of the relevant ellipsoid of each distinct dendrimers. We then defined the quantities and developed the tools for quantifying the relative orientation of dendrimer pairs in the bulk. We have chosen to use as measures for the relative orientation of a pair of dendrimers in the bulk liquid phase, the orientational correlation function S along with the parameter α. On the one hand, the α parameter includes information for the orientation of both long axes of the dendrimers relative to the center-to-center vector. On the other hand, S is a measure for the orientation of the long axes relative to one another. This description was a non-detailed but yet very practical way for calculating and interpreting the relative orientation of molecules. Our findings demonstrated the pronounced impact of the many body effects. Although we expected – based on the analysis at zero-density limit – that interacting macromolecules would become more and more elongated we observed that with increasing the volume fraction, dendrimers preserve their average asphericity and acylindricity. In contrast, the size of the dendrimers was strongly affected since they underwent a massive compression. Concerning the relative orientation of our model macromolecules, there was overwhelming evidence corroborating the existence of an antinematic [39] liquid phase.

Based on the observations for the bulk liquid phase we can now formulate our expectations for the structure of dendrimer crystals at even higher packing fractions. As the average orientation of dendrimers with a local antinematic order is fairly isotropic, a crystalline lattice formed by dendrimers is likely highly symmetric, i.e., cubic. However, the single-site-type cubic lattices (e.g., simple, body-centered , and face-centered) are incompatible with the antinematic order, implying that dendrimer crystals must be more complex.
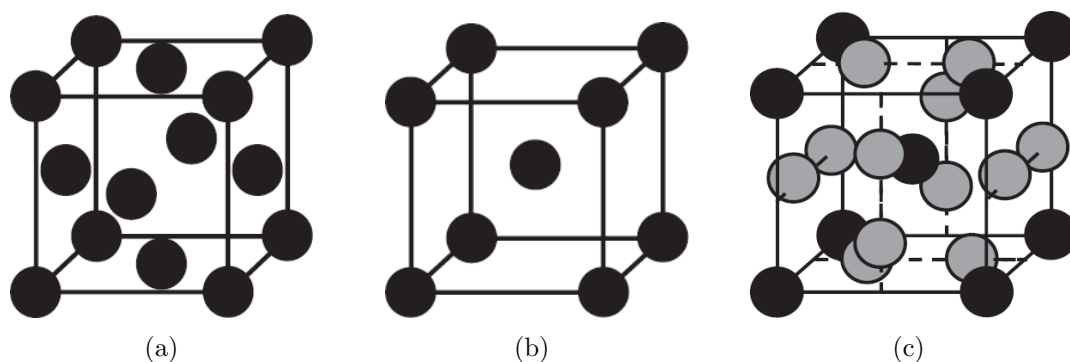
Figure 7.1: Unit cells of the FCC (a), BCC (b) and the A15 lattice (c). The columnar sites of the A15 lattice are colored in gray whereas the interstitial in black [135].
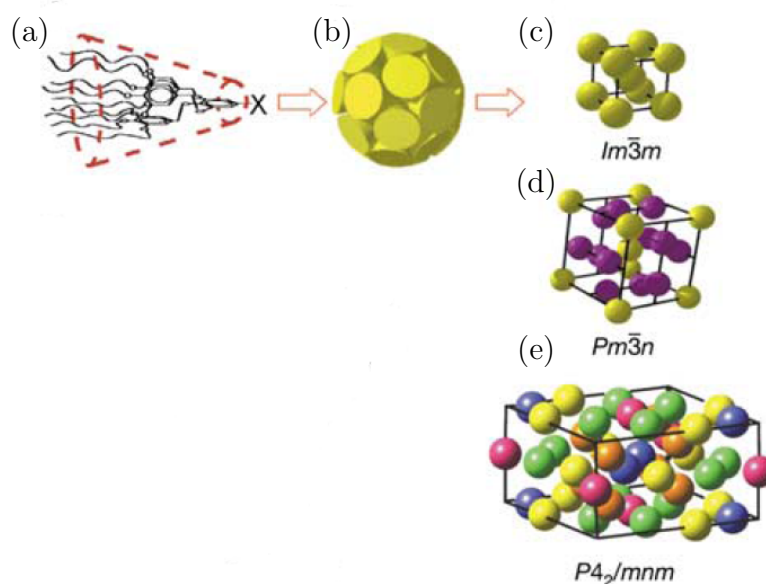

Figure 7.2: Self-organization of dendritic polymers [31]. (a) Dendrons assume a conical shape. (b) The cones assemble to form spherical micelles consisting of a compact core and a squishy shell, which pack on three different three-dimensional lattices (c), (d), (e). Panel (d) corresponds to the case of the A15 lattice.

It has been already observed that micell es of dendritic polymers (see Fig. 7.2) [30, 31] indeed self-assemble to form more complex structures such as the A15 lattice. Unlike the most common FCC [Fig. 7.1(a)] and BCC [Fig. 7.1(b)] lattices, the A15 lattice consists of two different types of lattice sites. The A15 unit cell [see Fig. 7.1(c)] includes eight sites: six columnar sites and two interstitial sites. The columnar sites are organized in pairs and lie along the bisectors of the faces of the cube. The space between the columns is then filled out by dodecahedral interstices, one in the center of the cell and one at the vertex. The existence of such a structure in dendrimer assemblies was unclear mostly of their low packing fraction. If the spherical micelles were hard they would self-organize into an FCC lattice that has the largest packing fraction (i.e. 74%) and thus it maximizes the configurational entropy of the system. In contrast, the A15 lattice is considered to be

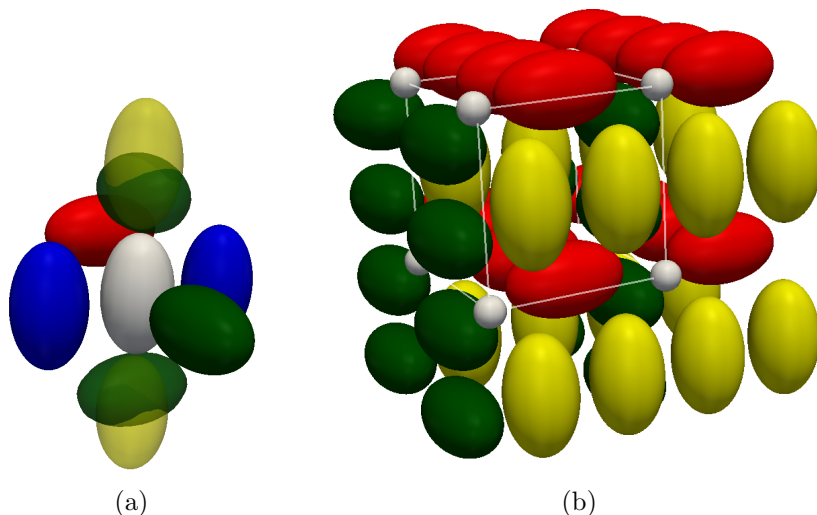<div align="center">(a)   (b)</div>

Figure 7.3: Schematic view of the antinematic packing pattern observed in a dendrimer liquid. Panel (a): The nearest-neighbor shell around the reference particle (white ellipsoid) contains ‖ (left and right), ∣˙ (back), and ⊥ (front) configurations in the equatorial region. The polar regions may be occupied either by ⊥ (green) or −− (yellow) configurations, the latter being a little farther from the reference particle. (b): The A15 lattice decorated by ellipsoids arranged in three sets of mutually interlocking columns is indeed able to capture the antinematic nature of the pattern shown in panel (a); the dodecahedral interstitial sites (small white spheres only shown in the unit cell for clarity) lack a preferred orientation. In this case the different colors indicate the different types of columnar site pairs.

loosely-packed since its packing fraction is that of the simple cubic (SC) lattice, i.e. 52%. Therefore, the formation of such complex cases is related to the fact that dendrimers are not structureless spheres, but they have a well-defined structure consisting of a compact core and a squishy shell. Thus, the stability of the lattice that the micelles form does not only depend on the repulsion between their hard cores but also on the interaction between their soft shells. Ziherl and Kamien in Ref. [136] suggested a theory that provided a robust insight into the self-organization of dendrimer micelles in complex lattices such as the A15 lattice; thus in the case of dendrimer systems the "softness" of the particles wins over their hard cores.

In the case of amphiphilic dendrimers, it is the three sets of mutually perpendicular columns [Fig. 7.3(a)] of particles which accommodate many features of the A15 packing pattern discussed above. In Fig. 7.3(b) we plot a lattice based on the local structure of a dendrimer liquid [see Fig. 7.3(a)]. Each columnar site [ellipsoids in Fig. 7.3(b)] has ‖ neighbors and hybrids of ∣˙, ⊥, and ⌞ neighbors as well as the more distant −− neighbors. Thus, unlike any single-site cubic crystal structure, the A15 lattice is essentially very consistent with antinematic order although the interstitial sites [small white spheres in Fig. 7.3(b)] are characterized by a dodecahedral environment and are most easily populated by spherical rather than elongated particles. In all, our results suggest that the stability of the A15 lattice is directly related to the elongated shape and deformability of dendrimers.

Appendices

Appendix A

Random distribution of α parameter

In this appendix we provide the code for calculating the random distribution of the parameter α (see Sec. 5.41) that was used for quantifying the relative orientation of dendrimers in the zero-density limit but also in the bulk. The resulting distribution is presented in Fig. A.1.

```python
#!/usr/bin/python
import sys
import numpy as np
import numpy.random as ran
import math as m


steps = 5000000


def ran_theta():
        return m.acos(ran.uniform(-1.0,1.0))
def ran_phi():
        return ran.uniform(0.0,2*m.pi)


R = []
L1 = []
L2 = []
Alpha =[]
count = 0


for s in range(steps):
        if s%100000 == 0:
                print "step=",s,"/",steps
        th1 = ran_theta()
        th2 = ran_theta()
        thr = ran_theta()
        ph1 = ran_phi()
        ph2 = ran_phi()
        phr = ran_phi()
#    Create three random unit vectors
#    l1: long axes first molecule
```

```
#    l2:  long  axes  second  molecule
#     r:  center  to  cente  vector
        l1 = ( m.sin(th1)*m.cos(ph1) ,
                   m.sin(th1)*m.sin(ph1) , m.cos(th1) )
        l2 = ( m.sin(th2)*m.cos(ph2) ,
                   m.sin(th2)*m.sin(ph2) , m.cos(th2) )
        r  = ( m.sin(thr)*m.cos(phr) ,
                   m.sin(thr)*m.sin(phr) , m.cos(thr) )
        L1.append( l1 )
        L2.append( l2 )
        R.append(r)
#    Calculate  alpha  parameter
        alpha = ( np.dot(l1,r))**2 + (np.dot(l2,r))**2
        Alpha.append(alpha)
#Create  histograms  of  alpha
H_alpha, bin_alpha = np.histogram( Alpha, bins = 40, range=[0,2.0] )
#output  to  files
fz_new  = open("alpha_dist_40bins.out","w")


for i in range(len(H_alpha)):
        fz_new.write("%4d\t%13.6f\t%13.6f\t%13.6f\n"
                %(i,bin_alpha[i],H_alpha[i]/float(steps),H_alpha[i]))
```
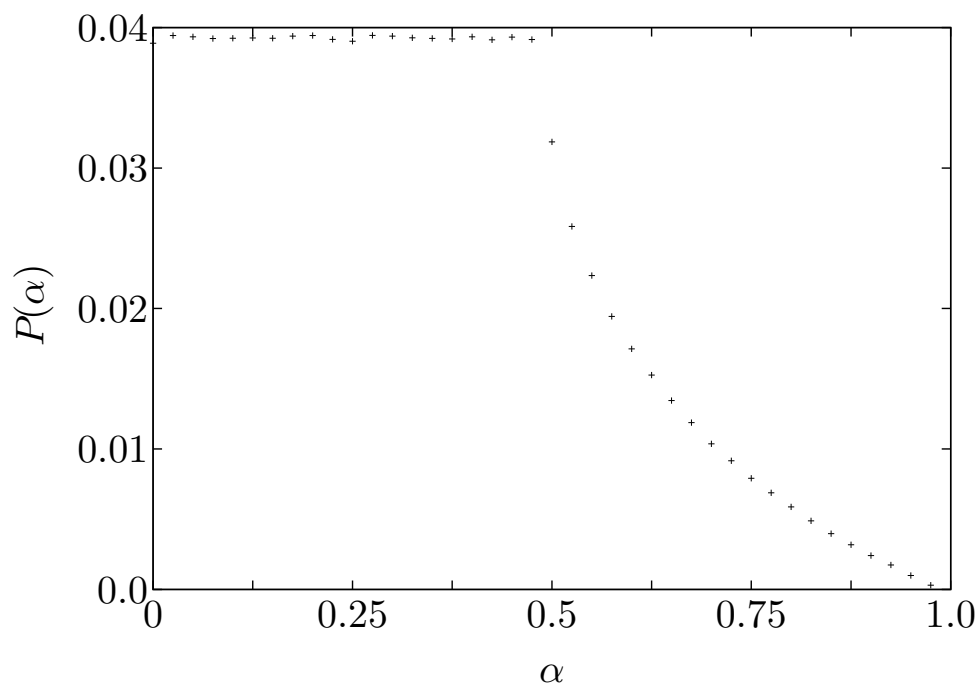

Figure A.1: Random distribution of the α used for describing relative orientation of dendrimers.

Appendix B

Further study of effective interactions of dendrimers

In Fig. B.1 we illustrate in a common plot the effective interaction extracted from the simulation data for a $G = 6$ using the umbrella sampling methods as well as the relevant GEM-n fitting lines; the relevant fitting parameters are presented in Table B.1. We observe that even in this case $n > 2$ dendrimers can form clusters.
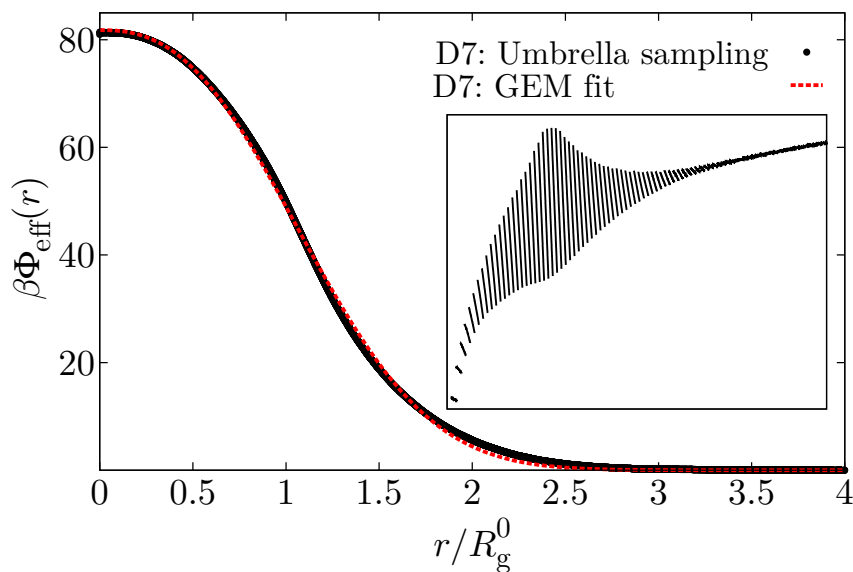

Figure B.1: The effective interaction of $G = 6$ dendrimers obtained with the umbrella sampling method (filled black diamonds, GEM-n-fit dashed red line). The inset shows the results obtained for the different windows that when combined give the final curve.

type	ϵ/k_BT	σ/R_g	n
D7	81.79	1.30	2.51

Table B.1: Fit parameters for the pair effective interaction of dendrimers of $G = 6$ dendrimers of D7-type using a GEM-n type of interaction [see Eq. (6.2)].

We also present in Fig. B.2 preliminary results for the effective interaction for $G = 4$ dendrimers of D7-type obtained with the multiscale coarse-graining method [133] in a common plot with the one obtained from the umbrella sampling method (see Sec. 2.4.3.1.)
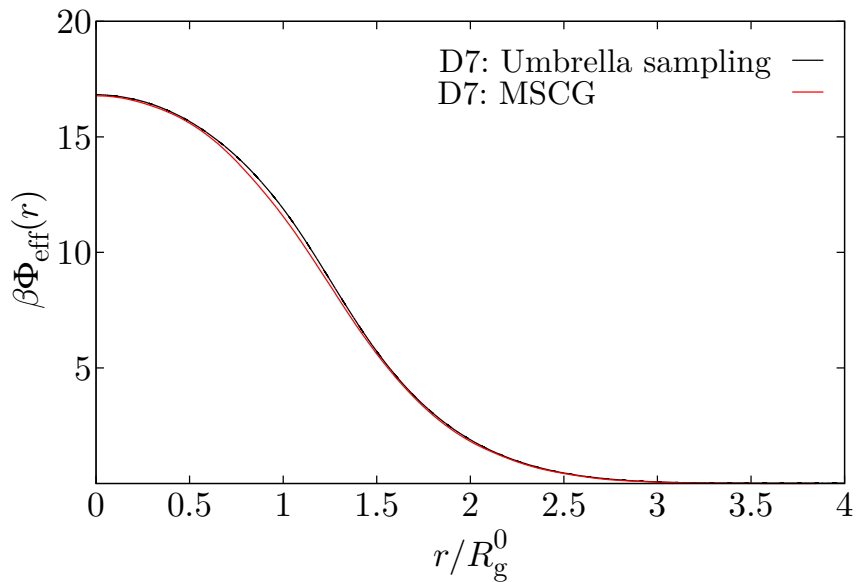

Figure B.2: Comparison between the effective interaction obtained with the umbrella sampling method (solid black line) and by the multiscale coarse-graining method [133] (M. Montes Saralegui, Technische Universität Wien).

Bibliography

[1] P. G. de Gennes, *Soft matter: more than words*, Soft Matter **1**, 16 (2005).

[2] R. Jones, *Soft condensed matter*, Oxford Master Series in Physics (Oxford University Press, 2002).

[3] W. Hu, *Polymer Physics: A Molecular Approach* (Springer, 2012).

[4] V. Parsegian, *Van der Waals forces: a handbook for biologists, chemists, engineers, and physicists* (Cambridge University Press, 2006).

[5] M. Amer, *Raman spectroscopy for soft matter applications*, Wiley InterScience online books (Wiley, 2009).

[6] P. G. de Gennes, *Soft matter*, Reviews of Modern Physics **64**, 645 (1992).

[7] E. Buhleier, W. Wehner and F. Vögtle, *Cascade- and nonskid-chain-like cyntheses of molecular cavity topologies*, Synthesis **1978**, 155 (1978).

[8] D. A. Tomalia, H. Baker and J. Dewald, *A new class of polymers: starburst-dendritic macromolecules*, Polymer Journal **17**, 117 (1985).

[9] D. A. Tomalia, A. M. Naylor and W. A. Goddard, *Starburst dendrimers: molecular-level control of size, shape, surface chemistry, topology, and flexibility from atoms to macroscopic matter*, Angewandte Chemie International Edition **29**, 138 (1990).

[10] T. J. Prosa, B. J. Bauer, E. J. Amis, D. A. Tomalia and R. Scherrenberg, *A SAXS study of the internal structure of dendritic polymer systems*, Journal of Polymer Science Part B: Polymer Physics **35**, 2913 (1997).

[11] A. Topp, B. J. Bauer, D. A. Tomalia and E. J. Amis, *Effect of solvent quality on the molecular dimensions of PAMAM dendrimers*, Macromolecules **32**, 7232 (1999).

[12] R. Esfand and D. A. Tomalia, *Poly(amidoamine) (PAMAM) dendrimers: from biomimicry to drug delivery and biomedical applications*, Drug Discovery Today **6**, 427 (2001).

[13] F. Zhao and W. Li, *Dendrimer/inorganic nanomaterial composites: tailoring preparation, properties, functions, and applications of inorganic nanomaterials with dendritic architectures*, Science China Chemistry **54**, 286 (2011).

[14] G. M. Dykes, *Dendrimers: a review of their appeal and applications*, Journal of Chemical Technology and Biotechnology **76**, 903 (2001).

[15] Y. Cheng and D. Tomalia, *Dendrimer-based drug delivery systems: from theory to practice* (Wiley, 2012).

[16] D. A. Tomalia, H. Baker, J. Dewald, M. Hall, G. Kallos, S. Martin, J. Roeck and P. Ryder, J.and Smith, *Dendritic macromolecules: synthesis of starburst dendrimers*, Macromolecules **19**, 2466 (1986).

[17] P. K. Maiti, G. Wang and W. A. Goddard, *Structure of PAMAM dendrimers: generations 1 through 11*, Macromolecules **37**, 6236 (2004).

[18] P. K. Maiti, Y. Li, T. Cagin and W. A. Goddard, *Structure of polyamidoamide dendrimers up to limiting generations: a mesoscale description*, The Journal of Chemical Physics **130**, 144902 (2009).

[19] M. L. Mansfield and M. Jeong, *Simulation of lattice dendrimers by a Monte Carlo technique with detailed balance*, Macromolecules **35**, 9794 (2002).

[20] M. Murat and G. S. Grest, *Molecular Dynamics study of dendrimer molecules in solvents of varying quality*, Macromolecules **29**, 1278 (1996).

[21] I. O. Götze and C. N. Likos, *Microscopic and coarse-grained correlation functions of concentrated dendrimer solutions*, Journal of Physics: Condensed Matter **17**, S1777 (2005).

[22] S. Huißmann, C. N. Likos and R. Blaak, *Conformations of high-generation dendritic polyelectrolytes*, Journal of Materials Chemistry **20**, 10486 (2010).

[23] S. Huißmann, C. N. Likos and R. Blaak, *Explicit vs implicit water simulations of charged dendrimers*, Macromolecules **45**, 2562 (2012).

[24] B. M. Mladek, G. Kahl and C. N. Likos, *Computer assembly of cluster-forming amphiphilic dendrimers*, Physical Review Letters **100**, 028301 (2008).

[25] B. M. Mladek and D. Frenkel, *Pair interactions between complex mesoscopic particles from widom's particle-insertion method*, Soft Matter **7**, 1450 (2011).

[26] C. N. Likos, *Effective interactions in soft condensed matter physics*, Physics Reports **348**, 267 (2001).

[27] I. O. Götze, H. M. Harreis and C. N. Likos, *Tunable effective interactions between dendritic macromolecules*, The Journal of Chemical Physics **120**, 7761 (2004).

[28] S. Huißmann, C. N. Likos and R. Blaak, *Effective interactions between charged dendrimers*, Soft Matter **7**, 8419 (2011).

[29] M. Ballauff and C. N. Likos, *Dendrimers in solution: Insight from theory and simulation*, Angewandte Chemie International Edition **43**, 2998 (2004).

[30] V. S. K. Balagurusamy, G. Ungar, V. Percec and G. Johansson, *Rational design of the first spherical supramolecular dendrimers self-organized in a novel thermotropic cubic liquid-crystalline phase and the determination of their shape by x-ray analysis*, Journal of the American Chemical Society **119**, 1539 (1997).

[31] X. Zeng, G. Ungar, Y. Liu, V. Percec, A. E. Dulcey and J. K. Hobbs, *Supramolecular dendritic liquid quasicrystals*, Nature **428**, 157 (2004).

[32] Y. Li, S.-T. Lin and W. A. Goddard, *Efficiency of various lattices from hard ball to soft ball: theoretical study of thermodynamic properties of dendrimer liquid crystal from atomistic simulation*, Journal of the American Chemical Society **126**, 1872 (2004).

[33] S. Prestipino and F. Saija, *Phase diagram of Gaussian-core nematics*, The Journal of Chemical Physics **126**, 194902 (2007).

[34] A. Nikoubashman and C. N. Likos, *Self-assembled structures of gaussian nematic particles*, Journal of Physics: Condensed Matter **22**, 104107 (2010).

[35] D. A. Lenz, R. Blaak and C. N. Likos, *Adsorption characteristics of amphiphilic dendrimers*, Soft Matter **5**, 2905 (2009).

[36] D. A. Lenz, B. M. Mladek, C. N. Likos, G. Kahl and R. Blaak, *Monomer-resolved simulations of cluster-forming dendrimers*, The Journal of Physical Chemistry B **115**, 7218 (2011).

[37] B. M. Mladek, *Exotic phenomena in the phase behaviour of soft matter systems*, Ph.D. thesis, Technishe Universität Wien, Fakultät für Physik, Wien (2007).

[38] J. Rudnick and G. Gaspari, *Elements of the random walk: An introduction for advanced students and researchers* (Cambridge University Press, 2004).

[39] K. Sokalski and T. Ruijgrok, *An anti-nematic phase of liquid crystals*, Physica A: Statistical Mechanics and its Applications **126**, 280 (1984).

[40] P. G. de Gennes and J. Prost, *The physics of liquid crystals*, International Series of Monographs on Physics (Clarendon Press, 1995).

[41] D. Greenwood, *Classical dynamics* (Dover Publications, 1997).

[42] E. Manousakis, *Lectures on statistical mechanics* (2007).

[43] J. Liouville, *Note sur la théorie de la variation des constantes arbitraires*, Journal de Mathématiques Pures et Appliquées **I**, 342 (1838).

[44] R. Tolman, *The principles of statistical mechanics* (Dover Publications, 1938).

[45] L. Boltzmann, *Vorlesungen über Gastheorie: Th. theorie van der Waals'; Gase mit zusammengesetzten Molekülen; Gasdissociation; Schlussbemerkungen* (J. A. Barth, 1898).

[46] J. L. Lebowitz and O. Penrose, *Modern ergodic theory*, Physics Today **26**, 23 (1973).

[47] J. Gibbs, *Elementary principles in statistical mechanics: developed with especial reference to the rational foundations of thermodynamics*, Yale bicentennial publications (C. Scribner's Sons, 1902).

[48] K. Binder and D. Heermann, *Monte Carlo simulation in statistical physics: an introduction* (Springer, 2010).

[49] E. Newman and G. Barkema, *Monte Carlo methods in statistical physics* (Clarendon Press, 1999).

[50] D. Frenkel and B. Smit, *Understanding molecular simulation : from algorithms to applications* (Academic Press, 2002), 2nd edn.

[51] D. P. Landau and K. Binder, *A guide to Monte Carlo simulations in statistical physics* (Cambridge University Press, 2005), 2nd edn.

[52] M. N. Rosenbluth and A. W. Rosenbluth, *Monte Carlo calculation of the average extension of molecular chains*, The Journal of Chemical Physics **23**, 356 (1955).

[53] N. Metropolis, A. W. Rosenbluth, M. N. Rosenbluth, A. H. Teller and E. Teller, *Equation of state calculations by fast computing machines*, The Journal of Chemical Physics **21**, 1087 (1953).

[54] J. Norris, *Markov chains* (Cambridge University Press, 1998).

[55] C. Gardiner, *Handbook of stochastic methods for physics, chemistry, and the natural sciences* (Springer, 1994).

[56] N. Metropolis, *The beginning of the Monte Carlo method*, Los Alamos Science, Special Issue, Stanislaw Ulam 1909 - 1984 **15** (1987).

[57] G. Marsaglia, *Choosing a point from the surface of a sphere*, The Annals of Mathematical Statistics **43**, 645 (1972).

[58] M. Borm and T. von Karman, *Periodic boundary conditions*, Physikalische Zeitschrift **13**, 297 (1912).

[59] P. P. Ewald, *Die Berechnung optischer und elektrostatischer Gitterpotentiale*, Annalen der Physik **369**, 253 (1921).

[60] J. M. Haile, *Molecular dynamics simulation: elementary methods*, A Wiley-Interscience publication (Wiley, 1997).

[61] D. Rapaport, *The art of molecular dynamics simulation* (Cambridge University Press, 2004).

[62] M. P. Allen and D. J. Tildesley, *Computer simulation of liquids*, Oxford science publications (Oxford University Press, 1989).

[63] B. Quentrec and C. Brot, *New method for searching for neighbors in molecular dynamics computations*, Journal of Computational Physics **13**, 430 (1973).

[64] T. Cormen, C. Leiserson, R. Rivest and C. Stein, *Introduction to algorithms* (MIT Press, 2001).

[65] W. Allen, *Data structures and algorithm analysis In C++, 3/E* (Pearson Education, 2007).

[66] B. Widom, *Some topics in the theory of fluids*, The Journal of Chemical Physics **39**, 2808 (1963).

[67] J. Hansen and I. McDonald, *Theory of simple liquids* (Elsevier Science, 2006).

[68] M. N. Rosenbluth and A. W. Rosenbluth, *Further results on Monte Carlo equations of state*, The Journal of Chemical Physics **22**, 881 (1954).

[69] G. M. Torrie and J. P. Valleau, *Monte Carlo free energy estimates using non-Boltzmann sampling: application to the sub-critical Lennard-Jones fluid*, Chemical Physics Letters **28**, 578 (1974).

[70] C. R. A. Abreu and F. A. Escobedo, *A general framework for non-Boltzmann Monte Carlo sampling*, The Journal of Chemical Physics **124**, 054116 (2006).

[71] K. Murthy, *Monte Carlo methods: in statistical physics* (Universities Press, 2004).

[72] D. Marzi, C. N. Likos and B. Capone, *Coarse graining of star-polymer – colloid nanocomposites*, The Journal of Chemical Physics **137**, 014902 (2012).

[73] B. Capone, I. Coluzza and J.-P. Hansen, *A systematic coarse-graining strategy for semi-dilute copolymer solutions: from monomers to micelles*, Journal of Physics: Condensed Matter **23**, 194102 (2011).

[74] P. J. Flory, *Principles of polymer chemistry* (Cornell University Press, 1953).

[75] G. S. Grest, L. J. Fetters, J. S. Huang and D. Richter, *Star polymers: experiment, theory, and simulation* (John Wiley and Sons, 2007).

[76] A. Jusufi, M. Watzlawek and H. Löwen, *Effective interaction between star polymers*, Macromolecules **32**, 4470 (1999).

[77] M. Rubinstein and R. H. Colby, *Polymer physics* (Oxford University Press, 2003).

[78] A. Hult, *Hyperbranched polymers* (John Wiley & Sons, Inc., 2002).

[79] H. Galina and X. Zhu, *Degree of branching* (John Wiley and Sons, 2011).

[80] H. Frey and D. Hölter, *Degree of branching in hyperbranched polymers. 3. Copolymerization of ABm-monomers with AB and ABn-monomers*, Acta Polymerica **50**, 67–76 (1999).

[81] G. Odian, *Principles of polymerization*, Wiley InterScience electronic collection (Wiley, 2004).

[82] R. Baxter, *Exactly solved models in statistical mechanics* (Dover Publications, 2007).

[83] M. Maciejewski, *Concepts of trapping topologically by shell molecules*, Journal of Macromolecular Science: Part A - Chemistry **17**, 689 (1982).

[84] P. de Gennes and H. Hervet, *Statistics of "starburst" polymers*, Journal de Physique Lettres **44**, 351 (1983).

[85] S. F. Edwards, *The statistical mechanics of polymers with excluded volume*, Proceedings of the Physical Society **85**, 613 (1965).

[86] P. G. de Gennes, *Some conformation problems for long macromolecules*, Reports on Progress in Physics **32**, 187 (1969).

[87] G. Newkome, C. Moorefield and F. Vögtle, *Dendritic molecules: concepts, syntheses, perspectives* (Wiley, 2008).

[88] R. L. Lescanec and M. Muthukumar, *Configurational characteristics and scaling behavior of starburst molecules: a computational study*, Macromolecules **23**, 2280 (1990).

[89] D. Boris and M. Rubinstein, *A self-consistent mean field model of a starburst dendrimer: dense core vs dense shell*, Macromolecules **29**, 7251 (1996).

[90] L. Kadanoff, *More is the same; phase transitions and mean field theories*, Journal of Statistical Physics **137**, 777 (2009).

[91] C. N. Likos, A. Lang, M. Watzlawek and H. Löwen, *Criterion for determining clustering versus reentrant melting behavior for bounded interaction potentials*, Physical Review E **63**, 031206 (2001).

[92] B. M. Mladek, D. Gottwald, G. Kahl, M. Neumann and C. N. Likos, *Formation of polymorphic cluster phases for a class of models of purely repulsive soft spheres*, Physical Review Letters **96**, 045701 (2006).

[93] D. A. Lenz, R. Blaak, C. N. Likos and B. M. Mladek, *Microscopically resolved simulations prove the existence of soft cluster crystals*, Physical Review Letters **109**, 228301 (2012).

[94] K. Kremer and G. S. Grest, *Dynamics of entangled linear polymer melts: A molecular-dynamics simulation*, The Journal of Chemical Physics **92**, 5057 (1990).

[95] P. Welch and M. Muthukumar, *Tuning the density rofile of dendritic polyelectrolytes*, Macromolecules **31**, 5892 (1998).

[96] L. Onsager, *The effects of shape on the interaction of colloidal particles*, Annals of the New York Academy of Sciences **51**, 627 (1949).

[97] G. J. Vroege and H. N. W. Lekkerkerker, *Phase transitions in lyotropic colloidal and polymer liquid crystals*, Reports on Progress in Physics **55**, 1241 (1992).

[98] P. Atkins, *Physical Chemistry* (Macmillan Higher Education, 1997).

[99] P. Ziherl, *Physics of soft matter* (2013).

[100] P. Chaikin and T. Lubensky, *Principles of condensed matter physics* (Cambridge University Press, 2000).

[101] J. W. Cooley and J. W. Tukey, *An algorithm for the machine calculation of complex fourier series*, Mathematics of Computation **19**, 297 (1965).

[102] J. Higgins and H. Benoît, *Polymers and neutron scattering* (Clarendon Press, 1994).

[103] O. Glatter and O. Kratky, *Small angle X-ray scattering* (Academic Press, 1982).

[104] A. Filipponi, *The radial distribution function probed by X-ray absorption spectroscopy*, Journal of Physics: Condensed Matter **6**, 8415 (1994).

[105] J. Hamilton, *Time series analysis* (Princeton University Press, 1994).

[106] G. Box, G. Jenkins and G. Reinsel, *Time series analysis: forecasting and control* (Wiley, 2013).

[107] C. Chatfield, *The analysis of time series: an introduction* (Taylor and Francis, 2003), 6th edn.

[108] M. L. Mansfield and L. I. Klushin, *Monte Carlo studies of dendrimer macromolecules*, Macromolecules **26**, 4262 (1993).

[109] P. E. Theodorakis, H.-P. Hsu, W. Paul and K. Binder, *Computer simulation of bottle-brush polymers with flexible backbone: good solvent versus theta solvent conditions*, The Journal of Chemical Physics **135**, 164903 (2011).

[110] H. von Storch and F. Zwiers, *Statistical analysis in climate research* (Cambridge University Press, 2001).

[111] S. Hadizadeh, A. Linhananta and S. S. Plotkin, *Improved measures for the shape of a disordered polymer to test a mean-field theory of collapse*, Macromolecules **44**, 6182 (2011).

[112] W. Kuhn, *Über die Gestalt fadenförmiger Moleküle in Lösungen*, Kolloid Zeitschrift **68**, 2 (1934).

[113] K. Šolc and W. H. Stockmayer, *Shape of a random-flight chain*, The Journal of Chemical Physics **54**, 2756 (1971).

[114] K. Šolc, *Shape of a random-flight chain*, The Journal of Chemical Physics **55**, 335 (1971).

[115] D. N. Theodorou and U. W. Suter, *Shape of unperturbed linear polymers: polypropylene*, Macromolecules **18**, 1206 (1985).

[116] P. E. Theodorakis and N. G. Fytas, *A study for the static properties of symmetric linear multiblock copolymers under poor solvent conditions*, The Journal of Chemical Physics **136**, 094902 (2012).

[117] G. Zifferer, *Shape asymmetry of star-branched random walks with many arms*, The Journal of Chemical Physics **102**, 3720 (1995).

[118] L. Lebedev and M. Cloud, *Tensor analysis* (World Scientific, 2003).

[119] J. Rudnick and G. Gaspari, *The asphericity of random walks*, Journal of Physics A: Mathematical and General **19**, L191 (1986).

[120] R. Bishop and S. Goldberg, *Tensor analysis on manifolds* (Macmillan, 1968).

[121] R. P. Smith and E. M. Mortensen, *Bond and molecular polarizability tensors. I. mathematical treatment of bond tensor additivity*, The Journal of Chemical Physics **32**, 502 (1960).

[122] A. K. Soper, *Orientational correlation function for molecular liquids: The case of liquid water*, The Journal of Chemical Physics **101**, 6888 (1994).

[123] C. Gray and K. Gubbins, *Theory of molecular fluids: I: fundamentals* (Oxford University Press, 1984).

[124] G. Arfken, H. Weber and F. Harris, *Mathematical methods for physicists: a comprehensive guide* (Elsevier, 2012).

[125] U. Gedde, *Polymer physics* (Springer, 1995).

[126] S. Fakirov, *Oriented polymer materials* (Wiley, 2008).

[127] N. Platé and S. Schnur, *Liquid-crystal polymers* (Plenum Press, 1993).

[128] A. M. Naylor, W. A. Goddard, G. E. Kiefer and D. A. Tomalia, *Starburst dendrimers. 5. Molecular shape control*, Journal of the American Chemical Society **111**, 2339 (1989).

[129] H. M. Harreis, C. N. Likos and M. Ballauff, *Can dendrimers be viewed as compact colloids? A simulation study of the fluctuations in a dendrimer of fourth generation*, The Journal of Chemical Physics **118**, 1979 (2003).

[130] C. N. Likos, B. M. Mladek, D. Gottwald and G. Kahl, *Why do ultrasoft repulsive particles cluster and crystallize? Analytical results from density-functional theory*, The Journal of Chemical Physics **126**, 224502 (2007).

[131] S. Kirkpatrick, C. D. Gelatt and M. P. Vecchi, *Optimization by simulated annealing*, Science **220**, 671 (1983).

[132] J. Corner, *The second virial coefficient of a gas of non-spherical molecules*, Proceedings of the Royal Society A. **192**, 275 (1948).

[133] S. Izvekov and G. A. Voth, *A multiscale coarse-graining (MSCG) method for biomolecular systems*, The Journal of Physical Chemistry B **109**, 2469 (2005).

[134] I. Coluzza and D. Frenkel, *Virtual-move parallel tempering*, Chemical Physics and Physical Chemistry **6**, 1779 (2005).

[135] W. Kung, *Geometry and phase transitions in colloids and polymers* (World Scientific, 2009).

[136] P. Ziherl and R. D. Kamien, *Maximizing entropy by minimizing area: towards a new principle of self-organization*, The Journal of Physical Chemistry B **105**, 10147 (2001).

Acknowledgements

I would like to express my gratitude to all the people that helped me in different ways to complete this thesis. I would like to thank:

My advisors **Prof. Gerhard Kahl** and **Prof. Primož Ziherl**. Gerhard, many thanks for accepting me to work in your group and for supervising me. Primož, thank you for all the productive time during my stays in Ljubljana, for your comments and for sharing your wonderful ideas with me. Many thanks to both of you for your support and for the great chance that you gave me within the COMPLOIDS network.

Ronald Blaak for all the fruitful discussions, for the advice and for letting me bother him with my questions.

Prof. Christos N. Likos for his knowledge and enthusiasm for physics that combined with his multiculti identity made him the ideal coordinator of our European network. I hope that one day his biggest dream will come true and Π.Α.Ο.Κ will be the world champion.

Panos Theodorakis for being a great collaborator but most importantly a great friend. Panos helped me to get through numerous difficult situations.

My long time colleague and friend **Nikos Fytas** for his help and support from my early days as a Master student until now.

My office mate **Jan Kurzidim** for his help concerning practically everything that had to do with computers as well as for our discussion inside and outside of the University.

Emanuella Bianchi for her scientific help while completing this thesis but also for the crisis management.

Clara Abaurrea Velasco, the youngest member of the group, for all the fun we had during my last months in our office.

The rest of the members of the Soft Matter Theory group: **Ismene Kolovos, Martina Lechner, Moritz Antlanger, Günther Doppelbauer, Silvano Ferrari, Arash Nikoubashman, Marta Montes Saralegui, Dieter Schwanzer, Cecilia Bores Quijano, Andreas Tröster and Ulf Rørbæk Pedersen** for the nice working atmosphere and our lunch breaks.

Frau Heike Höller für ihre Hilfe und Geduld mit der ganzen COMPLOIDS Bürokratie.

My extremely special (in all sorts of ways) friend **Labrini At-hanassopoulou** for being always there. I never managed to escape her company no matter how far I traveled.
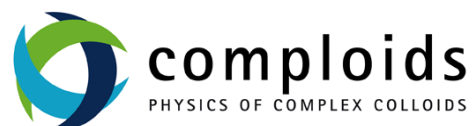
Meine besonderen (und auch speziellen) sehr sehr sehr deutschen Freunde **Jonas Riest** und **Christian Koch**. Jonesy, danke dass du mein Bier aus meinem Kühlschrank ausgetrunken hast. Christian danke, dass du mein Auto in den U.S.A verloren und einen Unfall gebaut hast. Ich wollte Garnelen und stattdessen habe ich einen Big Mac gegessen. Vielen Dank...

Prof. Anastasios Malakis. I always remember him especially whenever I make a successful step in my career. Thank you!

Τους γονείς μου, Τάσο και Βίκυ, για την αγάπη τους, την υποστήριξή τους, την καθοδήγησή τους και την υπομονή τους.

Vienna was meant to be the place where I would also find the love of my life: **Daniela Marzi**. Thank you for making every single day of my life beautiful. I could have never made it without you... Ich liebe dich!

Curriculum Vitae
Ioannis GEORGIOU, M.Sc

e-mail: ioannis.georgiou@tuwien.ac.at

Date of Birth: June 4th, 1982

Nationality: Greek

Education

- **Vienna University of Technology, Vienna, Austria**   *11/2010 – Present*
  Ph.D in Physics (anticipated)
  Marie Curie Fellow (FP7) within ITN-COMPLOIDS

- **University of Athens, School of Sciences, Physics Department, Athens, Greece**   *10/2007 – 06/2010*
  M.Sc. in Solid State Physics, GPA: 9.0/10 (Graduation with distinction)

- **University of Athens, School of Sciences, Physics Department, Athens, Greece**   *09/2000 – 09/2006*
  Diploma in Physics, Solid State Physics Section

Professional Experience

- *11/2010 – 12/2013*
  Project assistant at the Vienna University of Technology

- *09/2008 – 02/2009*
  Software developer of custom business software

- *10/2007 – 02/2008*
  Graduate teaching assistant in undergraduate physics laboratory, Physics Department, University of Athens (Greece)

Other Occupations

- *02/09 – 01/10* Military Service (Greece)